PHYSICS-BASED MICROWAVE DEVICE MODELING AND CIRCUIT OPTIMIZATION

By

QIAN CAI, M. Sc.(Eng.)
(South China Institute of Technology)

A Thesis

Submitted to the School of Graduate Studies

in Partial Fulfilment of the Requirements

for the Degree

Doctor of Philosophy

McMaster University

September 1992

PHYSICS-BASED MICROWAVE DEVICE MODELING AND CIRCUIT OPTIMIZATION

DOCTOR OF PHILOSOPHY (1992) McMASTER UNIVERSITY
(Electrical and Computer Engineering) Hamilton, Ontario

TITLE: **Physics-Based Microwave Device Modeling and Circuit Optimization**

AUTHOR: Qian Cai
M.Sc.(Eng.)
(South China Institute of Technology)

SUPERVISOR: John W. Bandler
Professor, Department of Electrical and Computer Engineering
B.Sc.(Eng.), Ph.D., D.Sc.(Eng.) (University of London)
D.I.C. (Imperial College)
P.Eng. (Province of Ontario)
C.Eng. F.I.E.E. (United Kingdom)
Fellow, I.E.E.E.
Fellow, Royal Society of Canada

NUMBER OF PAGES: xvi, 204

ABSTRACT

This thesis addresses physics-based microwave device modeling and circuit optimization, including conventional and statistical device modeling, performance-driven and yield-driven circuit design.

Approaches for physics-based device modeling are reviewed. Fundamental techniques of physics-based analytical MESFET modeling are presented. Device performance and parameter extraction with physics-based models (PBMs) are discussed.

Nonlinear circuit analysis with PBMs integrated into the harmonic balance (HB) method is presented. A detailed formulation of the HB equations with MESFET PBMs is given. An efficient Newton method for solving the HB equations is discussed.

Gradient-based optimization for circuit design is addressed. Physics-based circuit optimization integrates efficient adjoint sensitivity analysis approaches, the HB simulation method and PBMs. The physical (geometrical, material and process-related) parameters can be directly treated as design variables. Simultaneous device-circuit design is facilitated. The features of physics-based circuit optimization are demonstrated by two circuit design examples.

Statistical modeling at different levels is discussed. Statistical parameter

extraction and postprocessing are used to obtain statistical models to predict parameter statistics. The resulting statistical device models are verified by comparing the statistics of measurements with the corresponding statistics obtained by Monte Carlo simulation. Statistical modeling with equivalent circuit models (ECMs) and PBMs is demonstrated.

Yield-driven circuit design is addressed based on a one-sided ℓ_1 optimization algorithm with a generalized ℓ_p function. Yield optimization of MMICs with PBMs for passive and active devices is discussed. Its features are demonstrated by a three stage X-band MMIC amplifier design. A comprehensive approach to predictable yield-driven circuit design exploiting a novel statistical model is presented. For the first time, the yield estimated by Monte Carlo simulation is shown to be consistent with the yield predicted directly from device measurement data. Simultaneous device-circuit yield optimization assisted by yield sensitivity analysis is also demonstrated.

ACKNOWLEDGEMENTS

The author wishes to express his sincere appreciation to Dr. J.W. Bandler for his encouragement, expert guidance and supervision throughout the course of this work. Without his help and constructive criticism this thesis would not have been possible.

The author appreciates the opportunity given to him by Dr. Bandler to be involved in industrially relevant projects and academic research activities. In particular, the author has greatly benefitted from working with the *HarPE*™ and *OSA90/hope*™ microwave CAD systems developed by Optimization Systems Associates Inc.

Special thanks are due to Dr. R.M. Biernacki, one of the author's supervisory committee members, for his continuing advice, guidance, effort and collaboration which have greatly helped the author in this work. The author also thanks Dr. S.H. Chisholm and Dr. F. Mirza, members of his Supervisory Committee, for their valuable suggestions and continuing interest.

The author is greatly indebted to Dr. Q.J. Zhang, now with Carleton University, Ottawa, for introducing the author to the subject of physics-based circuit optimization and for his expert guidance and direct collaboration in this work. Sincere thanks are due to Dr. S.H. Chen of McMaster University and Optimization

Systems Associates Inc. for his generous advice and close collaboration in this work.

The author is very grateful to Dr. S. Ye of Optimization Systems Associates Inc. for creative discussions and useful suggestions. His generous cooperation and contribution to this work are also acknowledged.

It is the author's pleasure to have been associated with Dr. J. Song of McMaster University. His valuable suggestions and discussions were very helpful in this work. The author acknowledges inspiring discussions with his colleagues P.A. Grobelny and H. Yu.

The author would like to express his appreciation to Dr. R.J. Trew of North Carolina State University, Raleigh, NC, for useful discussions and providing essential data. Thanks are given to Dr. D.M. Brookbanks of GEC-Marconi Materials Research, Caswell, Northamptonshire, England, for generously providing the (Plessey) measurement data. Thanks are extended to Dr. P.H. Ladbrooke of GaAs Code Ltd., Cambridge, England, for helpful discussions and comments.

The financial assistance provided by the Natural Sciences and Engineering Research Council of Canada through Grants OGP0007239, OGP0042444, STR0040923, EQP0043573, the Department of Electrical and Computer Engineering through a Teaching Assistantship and Scholarship, and McMaster University through the Clifton W. Sherman Graduate Scholarship is gratefully acknowledged.

Finally, thanks are due to my family for their continuous encouragement, especially my wife, Hong Wang, for her understanding, patience and continuous support.

CONTENTS

LIST OF FIGURES

LIST OF TABLES

Chapter 1
INTRODUCTION

Computer-aided design (CAD) of microwave circuits has been significantly advanced during the past two decades. CAD technology has progressed from linear to nonlinear simulation, from small to large scale circuits, and from nominal design to yield optimization. The up-to-date CAD systems can perform various kinds of circuit analysis and design.

State-of-the-art microwave circuit analysis and design requires comprehensive general-purpose CAD software to integrate device modeling, steady-state and transient circuit simulation, sensitivity analysis, statistical modeling and analysis, performance- and yield-driven design optimization, as well as physics-based and process-oriented circuit design within the same framework.

Accurate device modeling is the basis for circuit simulation and design optimization. One of the fundamental active devices used in microwave circuits is the metal-semiconductor field-effect transistor (MESFET). Modeling of MESFETs has been continuously an active research subject since they were introduced. Approaches to MESFET modeling have been developed and a variety of models have been implemented into circuit simulators for such purposes as small- and large-signal circuit design. Generally, the methods for device modeling can be classified into two categories: equivalent circuit-based models (ECMs) and physics-based models (PBMs).

ECM modeling assumes an equivalent circuit model to simulate the external behaviour of the device under consideration. The determination of the ECM parameters usually depends on accurate parameter extraction from measured or simulated DC and AC data. ECMs enjoy high computational efficiency and can be easily implemented into circuit simulators. They have been the foundation of pre-MMIC (monolithic microwave integrated circuits) CAD and continue to dominate today's microwave simulators. They are easily understood by microwave engineers. However, there is no obvious relationship between ECM parameters and device physical parameters. Also, since the model parameters are usually identified after device fabrication, they have limited extrapolative or statistically meaningful forecasting abilities.

PBM modeling attempts to solve the fundamental device equations, describing device characteristics in terms of physical parameters such as gate length, channel thickness, doping profile, etc. Circuit design can then be considered at the device parameter level. In other words, the design variables can be directly the device geometrical, material and process-related parameters (Bandler, Zhang and Cai [23]). Therefore, the PBM is very effective in terms of predictability and first-pass success in the development of microwave integrated circuits (MICs) and MMICs.

Efficient microwave nonlinear circuit analysis has been a subject of serious research for a long time. Its importance has resurged with the development of MICs and MMICs, where nonlinear active devices are components critical to performance.

The harmonic balance (HB) method is an efficient approach for nonlinear microwave circuit analysis. The HB technique has been implemented into some

commercial software products, for example, *HarPE*™ [138] and *OSA90/hope*™ [139] from Optimization Systems Associates Inc., *Libra*™ [141] from EEsof Inc. and *Microwave Harmonica*™ [142] from Compact Software Inc.

Nonlinear circuit optimization requires efficient nonlinear circuit simulation. It has become feasible because of the efficiency of the HB method. Optimization employing the HB method has been seriously studied based on ECMs where the active and passive elements are explicitly represented through their equivalent circuit models. Direct treatment of the effects of device physical parameters on the overall circuit performance has been recently emphasized by a number of researchers, for instance, Bandler, Biernacki, Cai, Chen, Ye and Zhang (1992) [29], Filicori, Ghione and Naldi (1992) [55], Snowden and Pantoja (1992) [118] and Stoneking, Bilbro, Gilmore, Trew and Kelly (1992) [125]. One of the most significant benefits of PBMs over ECMs is the opportunity of directly optimizing controllable/designable physical parameters of the passive and active devices to improve the device and circuit performance.

Statistical modeling is a prerequisite for accurate yield-driven and cost-driven circuit analysis and optimization (Bandler and Chen (1988) [15], Purviance, Criss and Monteith (1988) [96]). The model statistics originate from random variations of geometrical, material and process-related parameters in manufacture. These statistical variations of device parameters result in complicated distributions and correlations of device responses. The ultimate purpose of statistical modeling is to characterize devices for accurate yield analysis and optimization.

With the rapid progress of GaAs fabrication technology, MMICs are becoming

increasingly practical (Jha, Goyal and Manz (1989) [71]). During the past two decades, hybrid microwave integrated circuits (HMICs) have been used in the microwave industry, where active and passive discrete components such as transistors, thin- or thick-film capacitors, inductors and resistors are connected on a dielectric substrate. In MMICs, all the active and passive components are fabricated on a common semi-insulating substrate. Post-production tuning of MMICs is restricted, and device replacement is not possible. In the production of MMICs, circuits are manufactured in batches rather than individually. The cost of manufacturing is directly affected by yield. Therefore, yield analysis and optimization, which take into account the manufacturing tolerances, model uncertainties, variations in the process parameters, environmental uncertainties, etc., have become widely accepted as indispensable components of the MMIC design methodology.

Many approaches developed for yield optimization are restricted to circuits employing ECMs. Statistics are then applied to the equivalent circuit elements such as capacitances, inductances or resistances. There is doubt as to whether such an approach is capable of reflecting the actual statistical behaviour of the physical parameters. In MMICs, a change of one device physical parameter may result in correlated changes in all elements of the equivalent circuit model. Furthermore, the resulting correlations may be very complicated and quite difficult to describe. Therefore, conventional design methods at the circuit level are of limited value for yield optimization of MMICs. PBMs, on the other hand, are more likely to provide reliable statistical behaviour because of the physical nature of the model. Consequently, meaningful results of yield optimization should be attainable.

This thesis consists of seven chapters and addresses physics-based device modeling, circuit simulation and optimization.

In Chapter 2, we present physics-based analytical MESFET modeling. Based on the discussion of MESFET physical structure and fundamental device equations, we concentrate on the Khatibzadeh and Trew model (Khatibzadeh and Trew (1988) [76]) which is used as a major vehicle of our research. Performance prediction and parameter extraction using the Khatibzadeh and Trew model are demonstrated.

In Chapter 3, we discuss the HB method for nonlinear circuit analysis. The HB technique is integrated with PBMs to permit physics-based circuit simulation. Our formulation extends the validity and simplifies the iteration layer of the method used by Khatibzadeh and Trew (1988) [76]. An efficient Newton method for solving the HB equation is described.

Gradient-based optimization techniques for circuit design are presented in Chapter 4. We review typical sensitivity analysis techniques for gradient calculation. The Feasible Adjoint Sensitivity Technique (FAST) is addressed. We integrate FAST with PBMs to facilitate physics-based design optimization. The adjoint analysis reuses the Jacobian matrix at the solution of the HB equation available in the form of LU factors. This increases the efficiency of optimization significantly. The additional effort for calculating sensitivity is solving the HB residual function with one simulation by perturbing the corresponding design variable. An algorithm for design optimization using a PBM of MESFETs is given. The efficiency of gradient-based optimization is demonstrated by circuit design examples.

Chapter 5 deals with statistical modeling problems. Statistical modeling at

different levels is illustrated. An approach for statistical modeling using parameter extraction to obtain sample of models and postprocessing to estimate parameter statistics is presented. Monte Carlo simulation is used to generate the device response statistics which are compared with measurements for model verification. Statistical modeling with ECMs is demonstrated using the Materka and Kacprzak model (Materka and Kacprzak (1985) [86]). Physics-based statistical modeling is illustrated using the Khatibzadeh and Trew model (Khatibzadeh and Trew (1988) [76]) and the Ladbrooke model (Ladbrooke (1989) [78]).

We present yield-driven circuit design in Chapter 6. The formulation of yield optimization problem using one-sided ℓ_1 technique with a generalized ℓ_p function is described. FAST gradient-based optimization is used to permit efficient yield-driven circuit design. Physics-based yield optimization of MMICs using PBMs for both the passive elements and active devices is addressed. Yield-driven design of a three stage X-band MMIC amplifier demonstrates a significant increase in yield after yield optimization. We present a comprehensive approach to predictable yield optimization exploiting a novel statistical model. The new model, referred to as the KTL model, takes advantages of the Khatibzadeh and Trew model and the Ladbrooke model and overcomes their shortcomings. We integrate the Khatibzadeh and Trew model for DC simulation and the Ladbrooke formulas for small-signal analysis. We demonstrate for the first time predictable yield optimization which is verified by device data. The benefits of simultaneous circuit-device yield optimization assisted by yield sensitivity analysis are also demonstrated.

The efficient software systems HarPE [138] and OSA90/hope [139] developed

by Optimization Systems Associates Inc. are used as a powerful environment to carry out all the calculations and verify the theoretical contributions presented in this thesis.

We conclude this thesis with Chapter 7, offering some suggestions for future research and development.

The author contributed substantially to the following original developments presented in this thesis:

1. Improvement of the Khatibzadeh and Trew model to extend the model validity and simplify the iteration layers.
2. Integration of PBMs with the HB method for physics-based circuit simulation.
3. Nonlinear circuit optimization with dynamically integrated PBMs and FAST, which treats directly the device physical parameters as design variables.
4. Statistical modeling with the Khatibzadeh and Trew model.
5. Investigation of yield optimization of MMICs using PBMs for both the passive and active devices.
6. Development of predictable yield-driven circuit design exploiting a novel statistical MESFET model.

Chapter 2

PHYSICS-BASED ANALYTICAL MESFET MODELING

2.1 INTRODUCTION

For active microwave circuit simulation and design the effectiveness of modern CAD methods relies heavily on accurate device models. ECM modeling and PBM modeling are two major approaches for device modeling.

ECM modeling assumes an equivalent circuit model which consists of linear and nonlinear circuit elements connected according to the predetermined circuit topology to represent device characteristics. Empirical equations are devised *a priori* for those nonlinear circuit elements. For instance, a number of different equations have been proposed to characterize the drain current from gate-source voltage and drain-source voltage by Curtice (1980) [43], Materka and Kacprzak (1985) [86], Curtice and Ettenberg (1985) [45], and Statz, Newman, Smith, Pucel and Haus (1987) [122].

The determination of the ECM parameters usually depends on accurate parameter extraction from measured or simulated DC and AC data. Different data are used to determine different sets of model parameters. For example, DC data can be used to extract gate, drain and source resistances (Fukui (1979) [56]) and to determine the parameters of drain currents (Curtice (1988) [47]). Bandler, Chen, Ye

and Zhang have presented a robust approach to model parameter extraction using large-scale optimization concepts (1988 [17]) and an efficient large-signal parameter extraction using harmonics (1989 [19]) from DC and AC data.

PBM modeling attempts to solve the fundamental device equations, describing device characteristics in terms of physical parameters. The fundamental device equations for PBMs may be solved numerically and analytically. Numerical models typically employ finite-difference or finite-element techniques. A number of numerical models such as two-dimensional models, temperature models and quasi-two-dimensional models, have been reported. Two-dimensional models (e.g., Kennedy and O'Brien (1970) [73], Reiser (1973) [100], Snowden, Hawes and Morgan (1983) [115], Snowden and Loret (1987) [116]) solve the basic device equations using a two-dimensional description of the active channel. Temperature models (e.g., Curtice and Yun 1981 [44]) describe the transport properties in terms of electron temperature rather than electric field. Quasi-two-dimensional models (e.g., Sandborn, East and Haddad (1987) [108], Snowden and Pantoja (1989) [117]) assume that the electric field in the undepleted active channel be one-dimensional while retaining the two-dimensional description of the conducting channel to simplify the model characterization. Numerical models play an important role in physical understanding of the device. They have, however, been hitherto regarded as cumbersome due to their computational burden. Analytical models attempt to solve the fundamental device equations analytically. These models offer a compromise between simulation efficiency and model accuracy. They are quite suitable for circuit design and optimization.

Analytical modeling can be traced back to the early pioneering work of Shockley in 1952 [111]. He invented the JFET and developed a detailed analysis based on three major assumptions: constant mobility in the material, gradual channel approximation and abrupt transition between the depletion region and the conducting channel. Shockley's analysis was improved subsequently by a number of researchers by including velocity saturation effects and nonuniform doping profile in the channel. Turner and Wilson (1969) [131] first analyzed velocity saturation effects in GaAs by postulating a finite channel opening at the drain end of the gate at the onset of drain current saturation while retaining Shockley's gradual channel approximation with a constant mobility. They assumed that the onset of velocity saturation always began precisely at the drain end of the gate. This model was modified by Lehovec and Zuleeg (1970) [80] by replacing the constant mobility with an approximate field-dependent expression for mobility. Grebene and Ghandhi (1969) [61] presented a two section model based on a piecewise linear approximation of v-E characteristic. The mobility was assumed constant below a critical electric field E_c and the electron velocity was assumed constant above E_c. The analysis was divided into two sections: gradual channel approximation analysis in low field region near the source and saturation analysis in high field region near the drain. This method was used by Pucel, Haus and Statz (1975) [95] to analyze the signal and noise properties of GaAs FETs. These models are based on one-dimensional or quasi two-dimensional analysis. Though including effects such as velocity saturation and nonuniform doping, they are DC and AC small-signal formulations which are applicable over a limited range of gate-length to channel thickness ratios. To eliminate these restrictions, a number of

large-signal analytical models were proposed. The large-signal analytical models try to solve the device equations with a minimum number of simplifying assumptions. Yamaguchi and Kodera (1976) [137] introduced the velocity vector rotation concept and approximated the gradual change in electron distribution using a sinusoidal function. Their model was constructed in a single formulation which described the current-voltage characteristics from the linear to the saturated drain current region. Based on Yamaguchi and Kodera's approach, Madjar and Rosenbaum (1981) [85] presented an large-signal model which related the terminal currents to the instantaneous terminal voltages and their time derivatives. They introduced a boundary parameter v_1 which was the only undetermined parameter in their theory. v_1 was evaluated using the condition: source conduction current was equal to drain conduction current. This condition is strictly valid for DC, and not for instantaneous currents for AC excitations. Madjar and Rosenbaum's model was modified by Khatibzadeh and Trew (1988) [76] to allow an arbitrary doping profile in the channel and to account for charge accumulation in the conducting channel at high electric fields and the associated capacitance in a self-consistent manner. A piecewise linear or quadratic v-E approximation was used and the negative differential mobility behaviour of GaAs MESFET was neglected. Chang and Day (1989) [38] used an empirical formula to approximate the v-E dependence including the negative differential mobility behaviour. The MESFET was correspondingly divided into three regions: the linear region, the knee region and the saturation region. Poisson's equation was solved in each region analytically to obtain the i-v characteristics. Bandler, Zhang and Cai (1990) [23] improved Khatibzadeh and Trew's model by

integrating v_1 with the harmonic balance equations to simplify the layers of iterations.

In the following sections, the physical structure and basic device equations of MESFETs are first briefly described. The Khatibzadeh and Trew model [76] is then discussed in detail. Finally, performance prediction and parameter extraction are given to demonstrate the model performances.

2.2 PHYSICAL STRUCTURE AND BASIC DEVICE EQUATIONS

2.2.1 Physical Structure [81]

Following the discussion of Liao (1990) [81], a simple GaAs MESFET can be schematically shown as Fig. 2.1. In GaAs MESFETs the substrate is doped with chromium (Cr) which results in a high resistivity and is commonly called semi-insulating (SI) substrate. On this nonconducting substrate a thin layer of doped n-type GaAs is grown epitaxially to form the channel region of the MESFETs which is usually referred to as the active layer. In many cases a buffer layer is grown between the SI substrate and the active layer. This layer has a high resistivity and contains very few mobile electrons. It acts effectively as an extension of the SI substrate but protects the subsequently grown active layer from any deleterious effects due to the bulk substrate which could otherwise occur. Two ohmic contacts form the source and drain electrodes. A Schottky barrier is located between them, forming the gate electrode. GaAs MESFETs can be developed by using either the epitaxial process such as liquid phase epitaxy, vapour phase epitaxy and molecular beam epitaxy, or the ion implantation method.

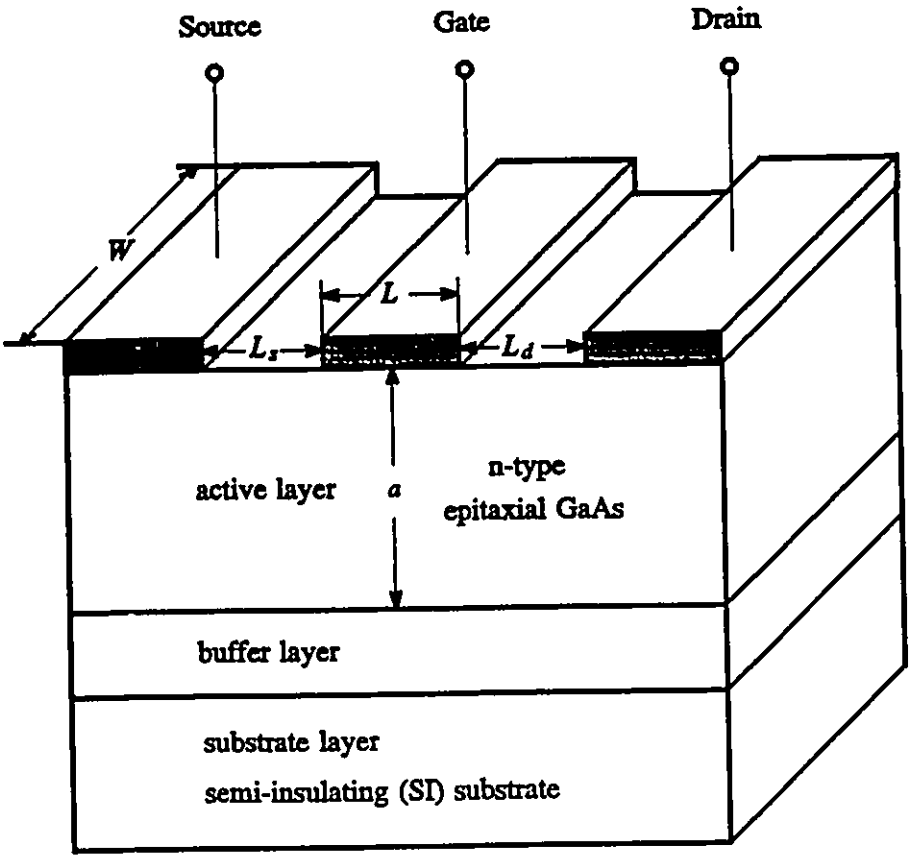

Fig. 2.1 A schematic diagram of a GaAs MESFET [81]. L is the gate length, W the gate width, a the channel thickness of active layer, L_s the gate to source spacing and L_d the gate to drain spacing.

2.2.2 Basic Device Equations [129]

The electrical properties of MESFETs can be characterized by the basic device equations which describe the static and dynamic behaviour of carriers in the channel under the influence of external fields produced by the applied voltages. The basic equations can be classified in three groups: Maxwell's equations, current-density equations and continuity equations (Sze (1981) [129]).

Maxwell's equations can be expressed as

$$\nabla \times \boldsymbol{E} = -\frac{\partial \boldsymbol{B}}{\partial t} \tag{2.1}$$

$$\nabla \times \boldsymbol{H} = \boldsymbol{J} + \frac{\partial \boldsymbol{D}}{\partial t} = \boldsymbol{J}_t \tag{2.2}$$

$$\nabla \cdot \boldsymbol{D} = \rho \tag{2.3}$$

$$\nabla \cdot \boldsymbol{B} = 0 \tag{2.4}$$

where $\boldsymbol{E}$ and $\boldsymbol{D}$ are the electric field and displacement vectors, respectively; $\boldsymbol{H}$ and $\boldsymbol{B}$ are the magnetic field and induction vector, respectively. $\boldsymbol{J}$ is the conduction current (drift current + diffusion current) density, $\boldsymbol{J}_t$ is the total current (conduction current + displacement current) density, ρ is the total electric charge density.

In addition to Maxwell's equations, the constitutive relationships between $\boldsymbol{E}$ and $\boldsymbol{D}$, $\boldsymbol{H}$ and $\boldsymbol{B}$, in a medium can be described as

$$\boldsymbol{D} = \varepsilon \boldsymbol{E} \tag{2.5}$$

$$\boldsymbol{B} = \mu \boldsymbol{H} \tag{2.6}$$

where ε and μ are the permittivity and permeability, respectively.

The current-density equation is

$$\boldsymbol{J} = -qn\boldsymbol{v} + qD_0 \nabla n \tag{2.7}$$

where q is the electron charge, n the free-electron density, v the electron velocity and D_0 the diffusion coefficient.

The continuity equation can be written as

$$\nabla \cdot J = q\frac{\partial n}{\partial t} \tag{2.8}$$

Substituting (2.5) to (2.3) and using the relation

$$E = -\nabla\psi \tag{2.9}$$

we can rewrite (2.3) as Poisson's equation

$$\nabla^2\psi = -\frac{\rho}{\varepsilon} \tag{2.10}$$

where ψ is the electrostatic potential.

Equations (2.7), (2.8) and (2.10) contribute to a "drift-diffusion" PBM which characterizes the behaviour of a MESFET (Reiser (1973) [100] and Snowden, Hawes and Morgan (1983) [115]).

2.3 THE KHATIBZADEH AND TREW MODEL [76]

Khatibzadeh and Trew (1988) [76] presented an analytic, large-signal model for GaAs MESFET. It is physics-based and describes the conduction and displacement currents of the MESFET in terms of instantaneous terminal voltages and their derivatives. This model allows an arbitrary doping profile in the channel. It also accounts for charge accumulation in the conducting channel at high electric fields and the associated capacitance in a self-consistent manner. The model is suitable for the optimization of ion-implanted and buried-channel MESFETs. The Khatibzadeh and Trew model is used as a vehicle in our research.

2.3.1 Model Formulation [76]

Following Khatibzadeh and Trew's approach [76], the MESFET is divided into two parts: intrinsic FET and extrinsic circuits as shown in Fig. 2.2. The model is formulated around the active region in the intrinsic part. This region consists of the area of the channel directly under the gate electrode. All other regions of the device are modeled phenomenologically using external linear elements in the extrinsic part. How to derive the values of these extrinsic elements in terms of physical parameters is not yet well established. Usually, their values are assumed according to practical knowledge or obtained through parameter extraction from measurements.

Fig. 2.3 shows schematically the active region and the corresponding Cartesian coordinates used for model formulation. Correspondingly, the Poisson equation, current-density equation and continuity equation can be written as

$$\nabla^2\psi(x, y) = -\frac{q}{\varepsilon}\left[N(y) - n(x, y)\right] \tag{2.11}$$

$$J(x, y) = -qn(x, y)v(x, y) + qD_0\nabla n(x, y) \tag{2.12}$$

$$\nabla\cdot J(x, y) = q\frac{\partial n(x, y)}{\partial t} \tag{2.13}$$

The total current density is

$$J_t(x, y) = J(x, y) + \varepsilon\frac{\partial E(x, y)}{\partial t} \tag{2.14}$$

where $N(y)$ is the donor concentration in the channel, which is a function of y.

v and E are assumed codirectional, i.e.,

$$v = -\mu(E)E \tag{2.15}$$

where E is the magnitude of E and $\mu(E)$ is the field-dependent mobility.

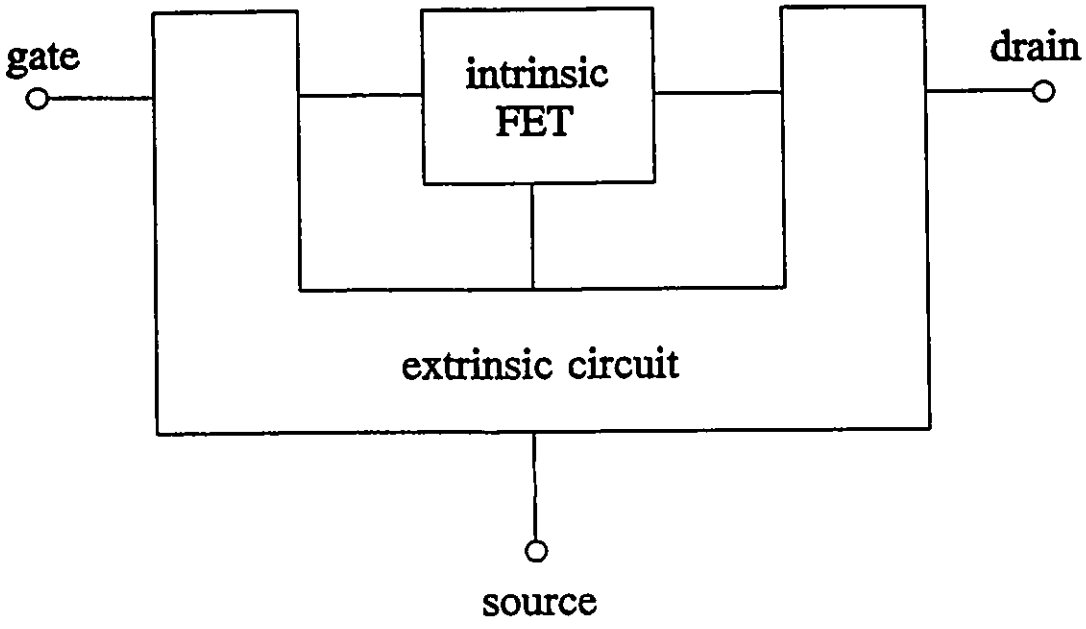

Fig. 2.2 Partition of a MESFET into intrinsic FET and its associated extrinsic circuit.

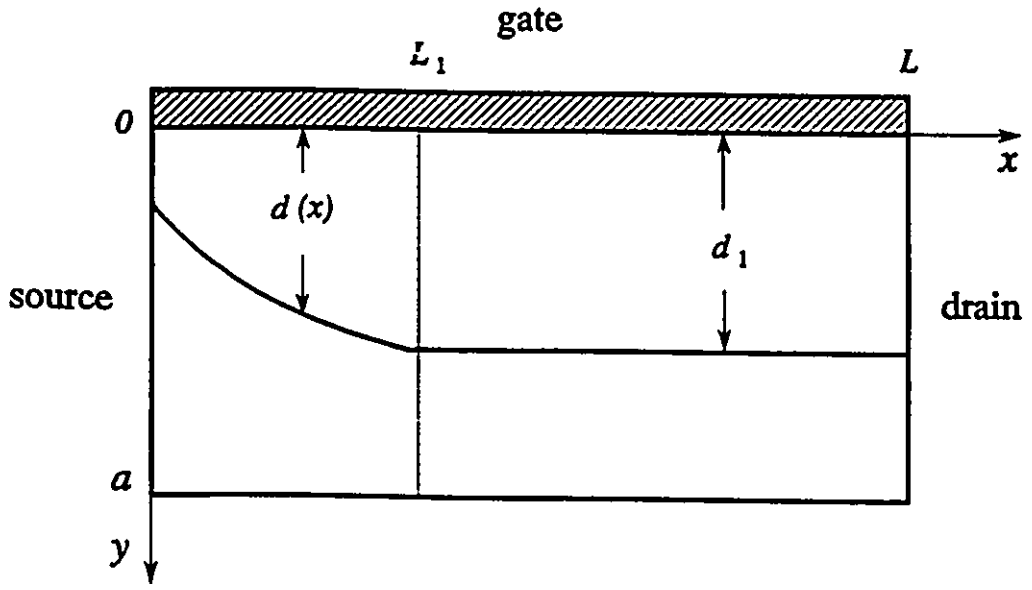

Fig. 2.3 Active region of a MESFET [76]. The plane $x = L_1$ separates the saturation region on the drain side and the linear region on the source side. L is the gate length, a the channel thickness, $d(x)$ the effective depletion-layer width as a function of x and d_1 the effective depletion-layer width in the saturation region as a constant.

Based on the magnitude of the electric field in the channel, specifically, at the $y = a$ boundary ($E(x, a)$), the device can operate in one of three modes [76]:

$$E(0, a) < E(L, a) < E_c \qquad \text{(mode-A)}$$

$$E(0, a) < E(L_1, a) = E_c < E(L, a) \qquad \text{(mode-B)}$$

$$E_c < E(0, a) < E(L, a) \qquad \text{(mode-C)}$$

The plane $x = L_1$ indicated in Fig. 2.3 separates the saturation and linear regions of the device.

The active region is divided into three parts: a depletion region under the gate Schottky barrier where $n = 0$, a free channel region where $n = N_d$ (N_d is the doping density) and a transition region where n varies smoothly from zero to N_d as indicated by Yamaguchi and Kodera (1976) [137] and Madjar and Rosenbaum (1981) [85]. The free electron density in the transition region may be expressed as [76,85,137]

$$n(x, y) = N(y)\left[1 + \gamma(x - L_1)\right] T(d(x), y) \qquad (2.16)$$

where γ and L_1 are the parameters to be determined from the boundary and bias conditions. For $x \le L_1$ (linear region), $\gamma = 0$. $T(d(x), y)$ is the transition function and can be defined as [76]

$$T(d(x), y) = 1 - \frac{1}{1 + \exp\left[\dfrac{y - d(x)}{\lambda}\right]} \qquad (2.17)$$

$d(x)$ is considered in [76] as an "effective depletion-layer width" and λ is a model parameter allowed to vary. Function (2.17) increases from almost 0 to almost 1 within the range of $y - d(x)$ from -3λ to 3λ, so according to [85,137] λ should be of the order of the Debye length λ_D. Alternatively, adapting the sinusoidal expression proposed by Yamaguchi and Kodera (1976) [137] and Madjar and Rosenbaum (1981)

[85] to the notation of Fig. 2.3 and allowing λ to vary, the transition function can be defined as

$$T(d(x), y) = \begin{cases} \frac{1}{2} + \frac{1}{2}\sin\left[\pi\frac{y - d(x)}{6\lambda}\right] & \text{if } d(x) - 3\lambda < y < d(x) + 3\lambda \\ 0 & \text{if } y \le d(x) - 3\lambda \\ 1 & \text{if } y \ge d(x) + 3\lambda. \end{cases} \tag{2.18}$$

Equation (2.16) with (2.17) or (2.18) eliminate the assumption of abrupt transition between the depletion region and the conducting channel.

2.3.2 Dependence of Electron Velocity on Electric Field

In [76,85], the dependence of the electron drift velocity v on the electric field E is modeled either by a piecewise linear approximation

$$v = \begin{cases} \mu_0 E & E \le E_c \\ v_s & E > E_c \end{cases} \tag{2.19}$$

or quadratic approximation

$$v = \begin{cases} v_s & E \ge 2E_c \\ \mu_0 E - \frac{v_s}{4E_c^2}E^2 & E < 2E_c \end{cases} \tag{2.20}$$

as shown in Fig. 2.4. This neglects the negative differential mobility of GaAs, exemplified by a typical v-E curve, also shown in Fig. 2.4. An equation with a step function was used by Chang and Day (1989) [38] to approximate the negative differential mobility, though the calculated and measured mobilities did not match well.

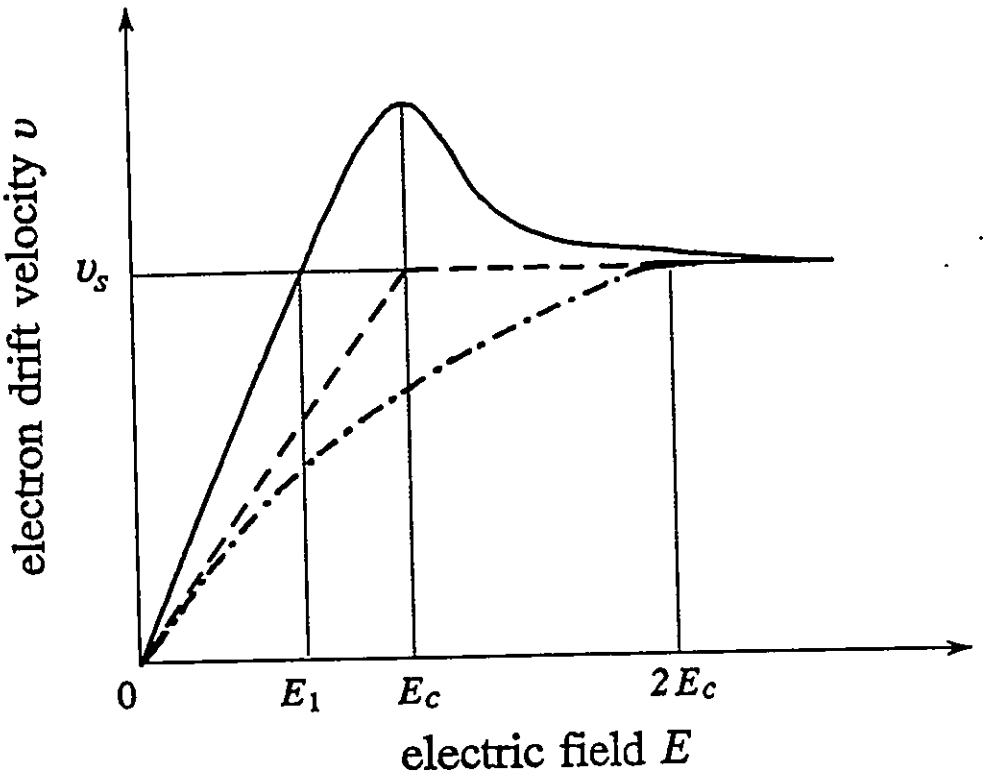

Fig. 2.4 Electron drift velocity versus electric field: (——) typical v-E curve, (---) piecewise linear approximation and (-·-) quadratic approximation.

A good fit to the measured v-E data can be achieved using the Snowden formula [115]

$$\mu(E) = \frac{300\mu_0}{T}\left[\frac{1 + \dfrac{8.5\times10^4 E^3}{\mu_0 E_0^4(1 - 5.3\times10^{-4}T)}}{1 + \left(\dfrac{E}{E_0}\right)^4}\right] \tag{2.21}$$

where

$$\mu_0 = \frac{0.8}{1 + \sqrt{N\times10^{-23}}}$$

is the doping-dependent low field mobility. Incorporating the functional form of (2.21) into (2.15) we express the v-E curve as

$$v = v_s \frac{\dfrac{E}{E_1} + \left(\dfrac{E}{E_0}\right)^\beta}{1 + \left(\dfrac{E}{E_0}\right)^\beta} \tag{2.22}$$

where v_s (the saturation velocity), E_0 (the characteristic field), E_1 and β are fitting parameters. Equations (2.21) and (2.22) can be reconciled if

$$\beta = 4$$

$$E_1 = \frac{v_{s0}}{\mu_0}$$

$$v_{s0} = \frac{T}{300}v_s = \frac{8.5\times10^4}{1 - 5.3\times10^{-4}T}$$

When T = 300°K we have $v_s = v_{s0} = \mu_0 E_1$ (as shown in Fig. 2.4). Thus E_1 is defined similarly to the critical field E_c (see Fig. 2.4) introduced in [76,85]. However, while E_1 denotes the intersection of $v = v_s$ and the line tangent at the origin to the v-E curve, E_c corresponds to the maximum velocity. Therefore, μ_0 is, in general,

interpreted differently in the two definitions.

As in [115], in our implementation β is fixed as $\beta = 4$. In Fig. 2.5 we show the v-E curve calculated by (2.22) with $v_s = 1.023\times10^5$m/s, $E_1 = 1.173\times10^5$V/m and $E_0 = 3.792\times10^5$V/m. Also shown is the experimental data used by Chang and Day (1989) [38] and attributed to Ruch and Kino (1967) [106], and Houston and Evans (1977) [66]. The match is excellent.

2.3.3 Solution for the Potential Distribution

The general solution of Poisson's equation (2.11) can be expressed as a linear superposition of two components [76,85,137]

$$\psi(x, y) = \psi_0(x, y) + \psi_1(x, y) \tag{2.23}$$

ψ_0 is the Laplacian potential due to the impressed voltages on the electrodes and satisfies the equation

$$\nabla^2\psi_0(x, y) = 0 \tag{2.24}$$

with the boundary conditions (see Fig. 2.3)

$$\psi_0(0, a) = 0 \tag{2.25a}$$

$$\psi_0(L, a) = v_0 \tag{2.25b}$$

$$\frac{\partial\psi_0(x, a)}{\partial y} = 0 \tag{2.25c}$$

$$\psi_0(x, 0) = 0 \tag{2.25d}$$

ψ_1 is due to the space charge in the channel and satisfies the equation

$$\nabla^2\psi_1(x, y) = -\frac{q}{\varepsilon}[N(y) - n(x, y)] \tag{2.26}$$

with the boundary conditions

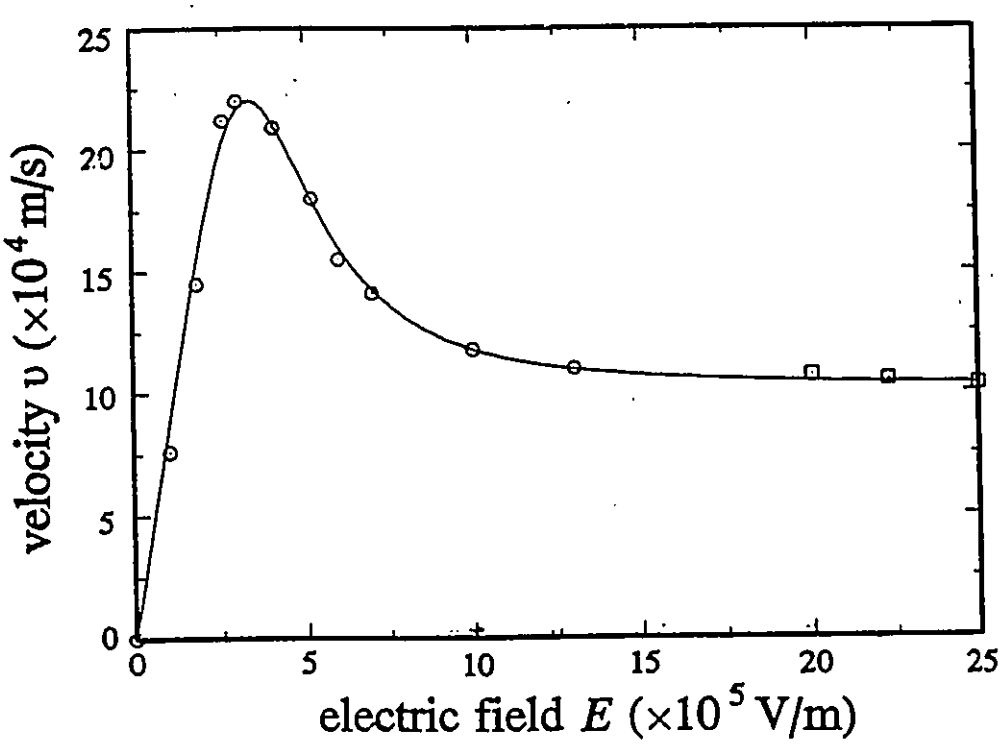

Fig. 2.5 Comparison of calculated and experimental v-E data for GaAs: (——) calculated from Equation (2.22), (○) experimental data from Ruch and Kino [106], and (□) experimental data from Houston and Evans [66].

$$\psi_1(0, a) = 0 \tag{2.27a}$$

$$\psi_1(L, a) = v_1 \tag{2.27b}$$

$$\frac{\partial \psi_1(x, a)}{\partial y} = 0 \tag{2.27c}$$

$$\psi_1(x, 0) = v_{gs} - V_{bi} \tag{2.27d}$$

where L and a are the gate length and channel thickness, respectively, V_{bi} is the built-in voltage of the gate Schottky contact, and v_{gs} is the applied intrinsic gate-source voltage. v_0 and v_1 are unknown fractions of v_{ds}, the applied intrinsic drain-source voltage, resulting from the boundary conditions (2.25b) and (2.27b) and must be solved for in order to determine the performance of the devices. Since $v_{ds} = v_1 + v_0$, it is sufficient to solve for v_1 only.

Khatibzadeh and Trew (1988) [76] showed that a simplified solution to (2.24) with the boundary conditions (2.25a)-(2.25d) is given by

$$\psi_0(x, y) = \frac{v_0}{\sinh\left(\frac{\pi L}{2a}\right)} \sinh\left(\frac{\pi x}{2a}\right) \sin\left(\frac{\pi y}{2a}\right) \tag{2.28}$$

and the solution to (2.26) with the boundary conditions (2.27a)-(2.27c) can be expressed as

$$\psi_1(x, y) = \begin{cases} -\frac{q}{\varepsilon} F_1(d(x), y) + \frac{v_1}{L} x & 0 \le x \le L_1 \\ -\frac{q}{\varepsilon} F_1(d_1, y) + \frac{v_1}{L} x + \frac{q}{\varepsilon} \gamma(x - L_1) F_2(d_1, y) & L_1 < x \le L \end{cases} \tag{2.29}$$

where

$$F_1(d(x), y) = \int_y^a \int_z^a [1 - T(d(x), \tau)] N(\tau) d\tau dz \tag{2.30}$$

$$F_2(d_1, y) = \int_y^a \int_z^a T(d_1, \tau)N(\tau)d\tau dz \tag{2.31}$$

T is the transition function defined by (2.17) and d_1 is the effective depletion-layer width in the saturation region (see Fig. 2.3). The piecewise transition function of (2.18) could be used here as well. The boundary condition (2.27d) was applied to (2.29) to solve for $d(x)$ and γ [76].

Solving for the potential ψ_1 in (2.29) involves two double integrations F_1 and F_2 which require significant computational effort. These numerical integrations are necessary if the doping profile is arbitrary. However, for uniform doping, i.e., if $N(y)$ = N_d in (2.16), the efficiency of the model can be greatly improved if (2.18) is used instead of (2.17) in (2.30) and (2.31) since (2.18) can be analytically integrated. This has been implemented in both HarPE [138] and OSA90/hope [139] and our experiments show that the simulation time can be reduced by more than two thirds as compared with using (2.17).

2.3.4 Intrinsic Currents

The gate, drain and source currents can be expressed by the equations

$$i_g = i_{gc}(\phi, v_1(\phi,t), v_{gs}(\phi,t), v_{ds}(\phi,t), t) + \frac{\partial q_g(\phi, v_1(\phi,t), v_{gs}(\phi,t), v_{ds}(\phi,t), t)}{\partial t} \tag{2.32}$$

$$i_d = i_{dc}(\phi, v_1(\phi,t), v_{gs}(\phi,t), v_{ds}(\phi,t), t) + \frac{\partial q_d(\phi, v_1(\phi,t), v_{gs}(\phi,t), v_{ds}(\phi,t), t)}{\partial t} \tag{2.33}$$

$$i_s = i_{sc}(\phi, v_1(\phi,t), v_{gs}(\phi,t), v_{ds}(\phi,t), t) + \frac{\partial q_s(\phi, v_1(\phi,t), v_{gs}(\phi,t), v_{ds}(\phi,t), t)}{\partial t} \tag{2.34}$$

where i_{gc}, i_{dc} and i_{sc} are the gate, drain and source conduction currents, respectively,

q_g, q_d and q_s stand for the total charges, respectively on the gate, drain and source electrodes, and ϕ is the parameter vector including gate length, gate width, channel thickness, doping density, etc. Equations (2.32)-(2.34) can be represented by the equivalent circuit shown in Fig. 2.6.

Under normal operation conditions, the gate is reverse biased and the gate conduction current i_{gc} can be neglected. (The gate forward biasing and drain breakdown conditions may be included by introducing diodes into the model (Khatibzadeh (1987) [75]).) The drain and source conduction currents i_{dc} and i_{sc} of (2.32)-(2.34) are calculated by integrating the current density J in (2.12) over the corresponding areas in the planes $x = L$ and $x = 0$, respectively, (see Fig. 2.3). In general, they can be written in the integral form as [75]

$$i_{dc} = \int_{x=L} J \cdot dS = -qW \int_0^a [\mu(E(L, y))n(L, y)E_x(L, y) + D\nabla_x n(L, y)]dy \quad (2.35)$$

and

$$i_{sc} = \int_{x=0} J \cdot dS = qW \int_0^a [\mu(E(0, y))n(0, y)E_x(0, y) + D\nabla_x n(0, y)]dy \quad (2.36)$$

where E_x and $\nabla_x n$ are the x components of E and ∇n, respectively, and W is the gate width. In the linear region ($0 \le x \le L_1$), the carrier concentration does not depend strongly on x, therefore the diffusion term (the second term on the right-hand-side of (2.36)) can be neglected [75].

The partial derivatives of the total charges q_g, q_d and q_s w.r.t. time t represent the displacement currents through the corresponding electrodes. Again, q_g, q_d and q_s can be written in integral form [75] as

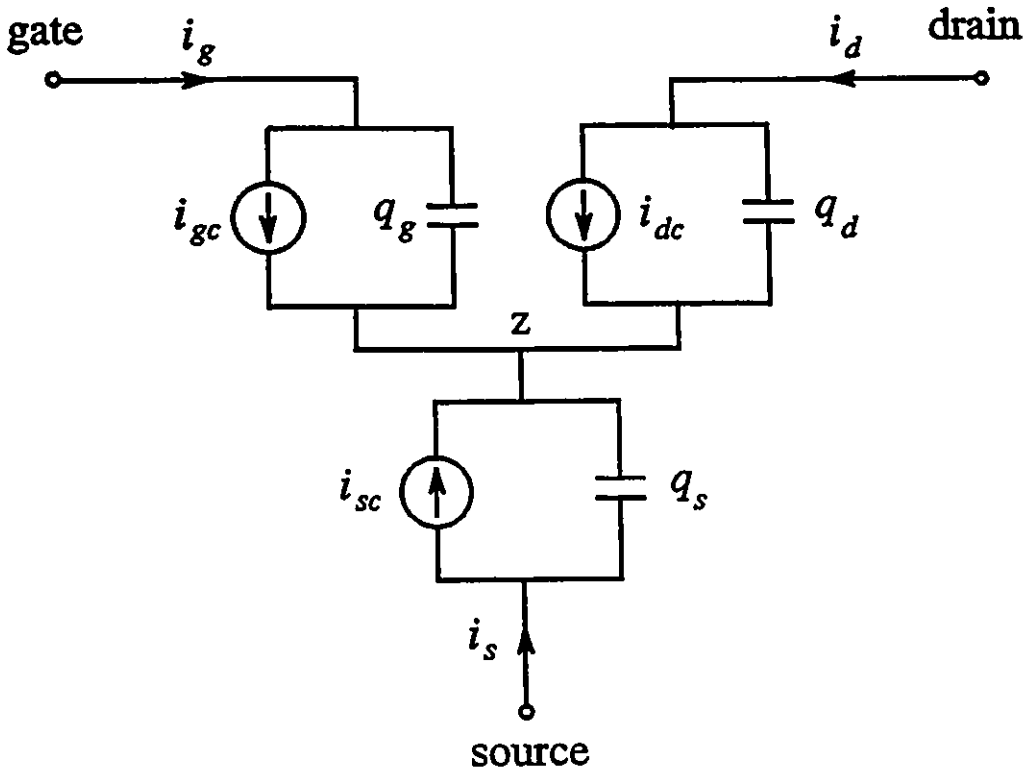

Fig. 2.6 Equivalent circuit for the intrinsic model.

$$q_g = -\varepsilon W \int_0^L E_y(x, 0)dx \tag{2.37}$$

$$q_d = -\varepsilon W \int_0^a E_x(L, y)dy \tag{2.38}$$

$$q_s = \varepsilon W \int_0^a E_x(0, y)dy \tag{2.39}$$

where E_y is the y component of E.

$E(x, y)$ can be evaluated using (2.9) after the electrostatic potential ψ is obtained. Since $E(x, y)$ and $n(x, y)$ depend on the voltages v_1, v_{gs} and v_{ds}, the conduction currents and the total charges are nonlinear functions of v_1, v_{gs} and v_{ds}. Under the normal operation conditions and neglecting the gate conduction current, the magnitude of the drain and source conduction currents are equal at DC. In [76,85,137], the solution of v_1 is obtained iteratively by forcing the difference between the drain and source conduction currents to be sufficiently small.

2.4 PERFORMANCE PREDICTION AND PARAMETER EXTRACTION

A significant advantage of the PBMs over the ECMs is that directly from the physical parameter values PBM simulation can predict device performance, or even the performance of the overall circuit embedding the device. This could be done before the device is manufactured and for any range of working conditions. Obviously, the validity of this approach strongly depends on model accuracy. We believe that the predictive potential of PBMs should and will provide device and circuit engineers with the opportunity to extend and improve their design capabilities.

Using the MESFET physical parameters given in [75] we compare DC simulation results of the PBM described in Section 2.3 to the measured DC data used in [75], as shown in Fig. 2.7. Good agreement is observed.

Parameter extraction, indispensable for ECMs [17,19,47,56,68], may also prove useful for PBMs. Firstly, as was already mentioned in Section 2.3.1, parameter extraction can be used to determine the extrinsic device parameters. Secondly, the intrinsic physical parameters, even if they are known or measured, can be fine tuned, for example, to account for measurement errors. It should be noted that, unlike ECMs, it is relatively easy to estimate a good starting point for parameter extraction of PBMs, since the model parameters are physically meaningful and tangible. Another significant application of PBM parameter extraction is for statistical modeling at the device physical and geometrical level, in which a number of devices must be characterized from measurements. This is further discussed in Chapter 5.

To illustrate PBM parameter extraction of a FET we consider the extrinsic and intrinsic model shown in Fig. 2.8. The intrinsic parameters are defined in Table 2.1. S-parameter measurements [140] in the frequency range 1GHz to 21GHz at 3 bias points (gate bias 0V, -0.84V, -1.54V and drain bias 5V) are processed simultaneously. The v-E curve obtained by fitting (2.22) to the experimental data [66,106] is used here since no v-E measurements for this particular device are available.

Parameter extraction was carried out using the ℓ_2 optimizer [14] of HarPE [138]. Measured values of gate length L, gate width W and doping density N_d were assigned as the starting values. The optimization was performed in two stages. First, the extrinsic parasitic parameters were optimized while the intrinsic physical

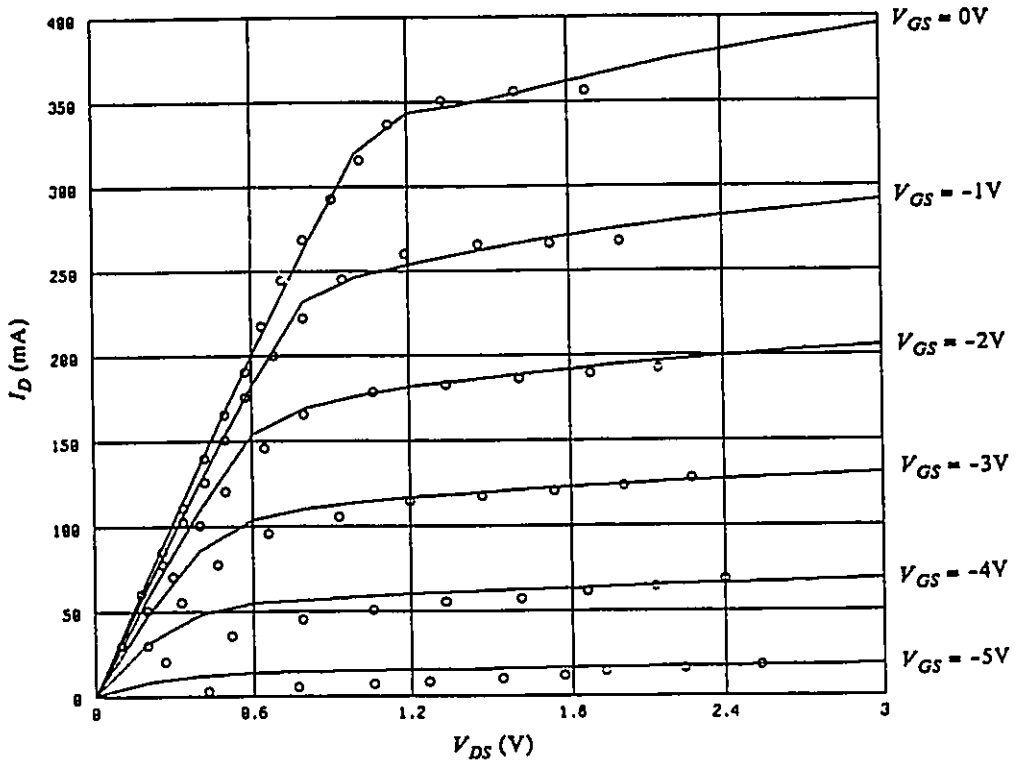

Fig. 2.7 Comparison of the simulated and measured DC characteristics: (——) simulation results with PBM (o) measured data [75].

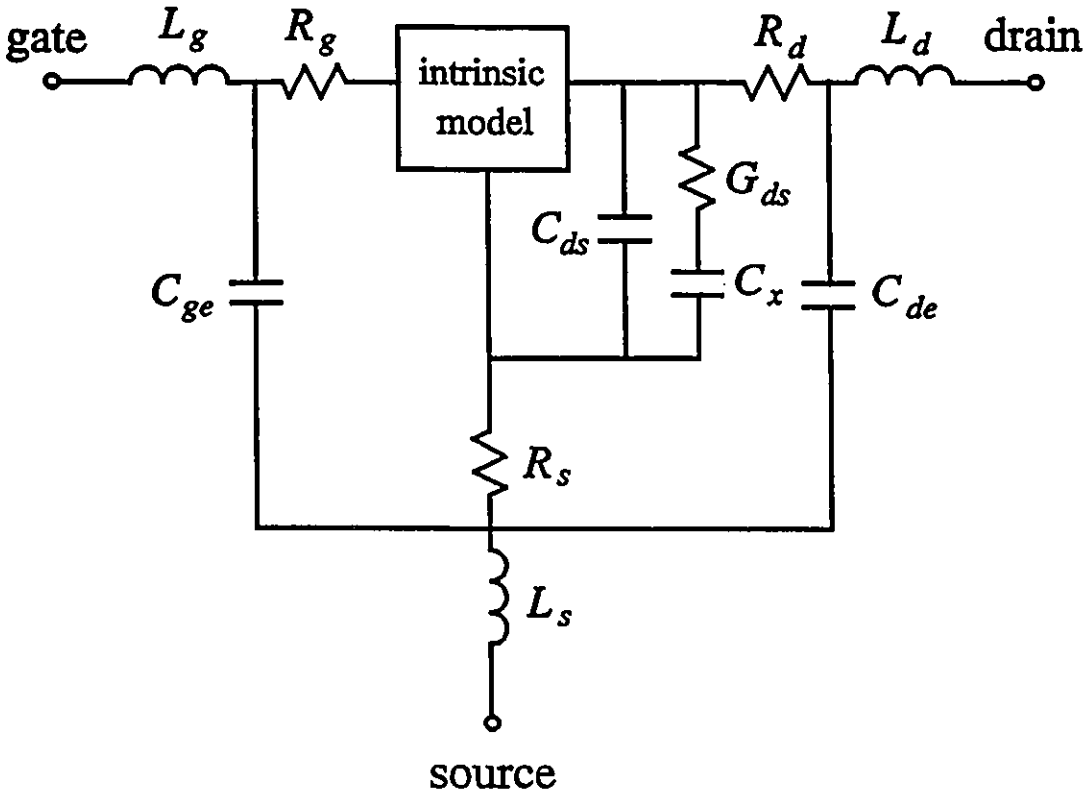

Fig. 2.8 Circuit topology for parameter extraction showing the intrinsic FET and its associated extrinsic elements [19].

TABLE 2.1

MESFET INTRINSIC PARAMETERS

Parameter	Notation	Unit
Gate Length	L	μm
Gate Width	W	μm
Channel Thickness	a	μm
Doping Density	N_d	$1/m^3$
Critical Electric Field	E_c	V/m
Saturation Velocity	v_s	m/s
Relative Permittivity	ε_r	—
Built-in Potential	V_{bi}	V
Low-Field Mobility	μ_0	m^2/Vs
High-Field Diffusion Coefficient	D_0	m^2/s

TABLE 2.2

EXTRACTED PARAMETERS FOR
THE KHATIBZADEH AND TREW MODEL

Parameter	Before Optimization	After Optimization	Plessey Data [140]
$L(\mu m)$	0.551	0.571	0.551
$W(\mu m)$	300.0	301.6	300.0
$N_d(1/m^3)$	2.235×10^{23}	2.093×10^{23}	2.235×10^{23}
$a(\mu m)$	0.200	0.167	—
$V_{bi}(V)$	0.700	0.672	—
$R_i(\Omega)$	2.200	2.302	—
$R_d^o(\Omega)$	3.500	3.524	—
$R_s(\Omega)$	2.500	2.704	—
$L_g(nH)$	0.050	0.028	—
$L_d(nH)$	0.050	0.010	—
$L_s(nH)$	0.080	0.036	—
$C_{ge}(pF)$	0.100	0.123	—
$C_{de}(pF)$	0.050	0.055	—
$G_{ds}(1/\Omega)$	0.003	0.003	—

Other parameters are fixed as

$E_1 = 1.173\times10^5 V/m$ $\quad v_s = 1.023\times10^5 m/s$
$D_0 = 0.001 m^2/s$ $\quad \epsilon_r = 12.9$
$C_x = 10pF$

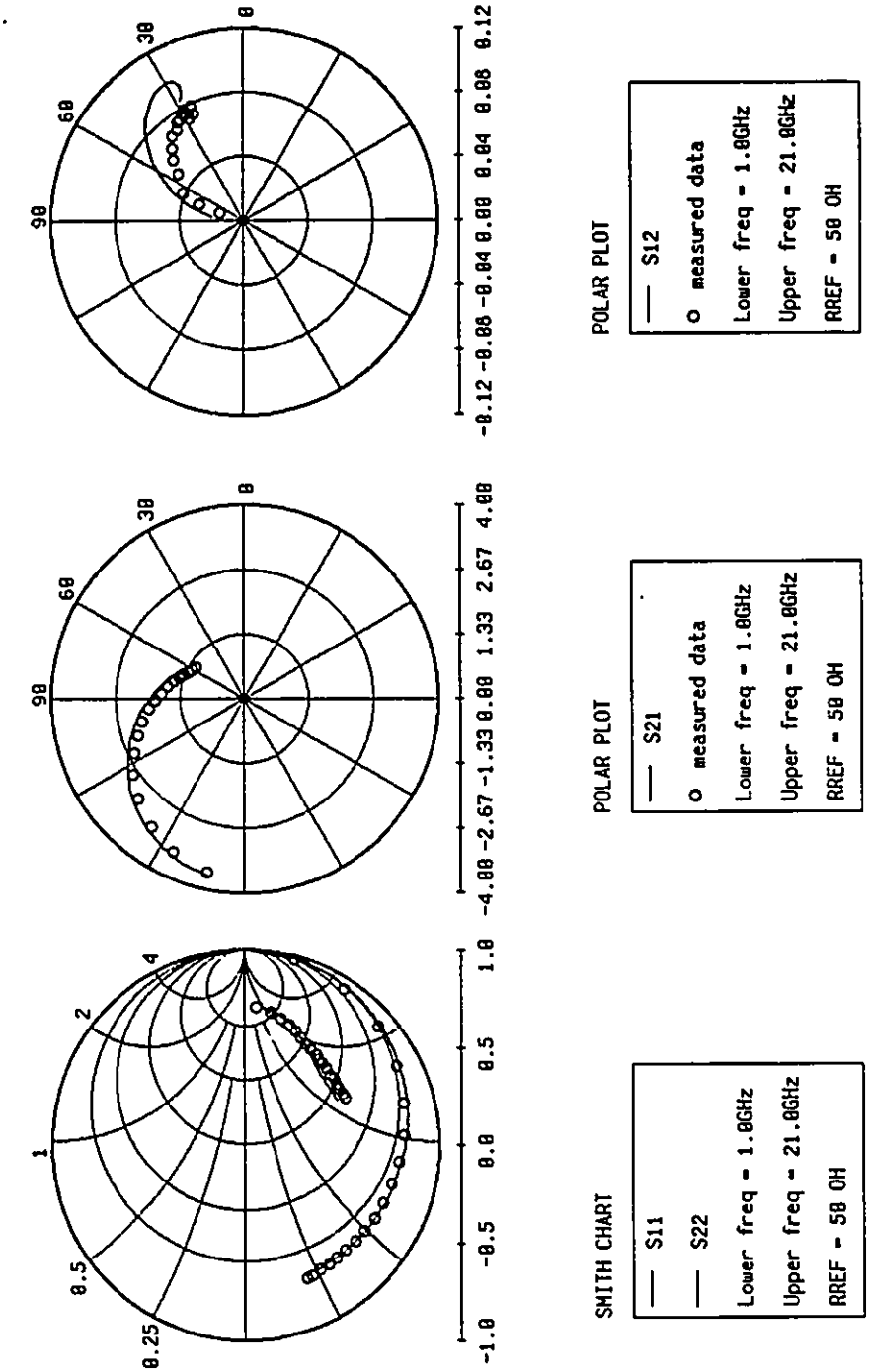

Fig. 2.9 Comparison of measured (o) and calculated (—) S parameters at bias point: $V_G = 0V$, $V_D = 5V$ for parameter extraction.

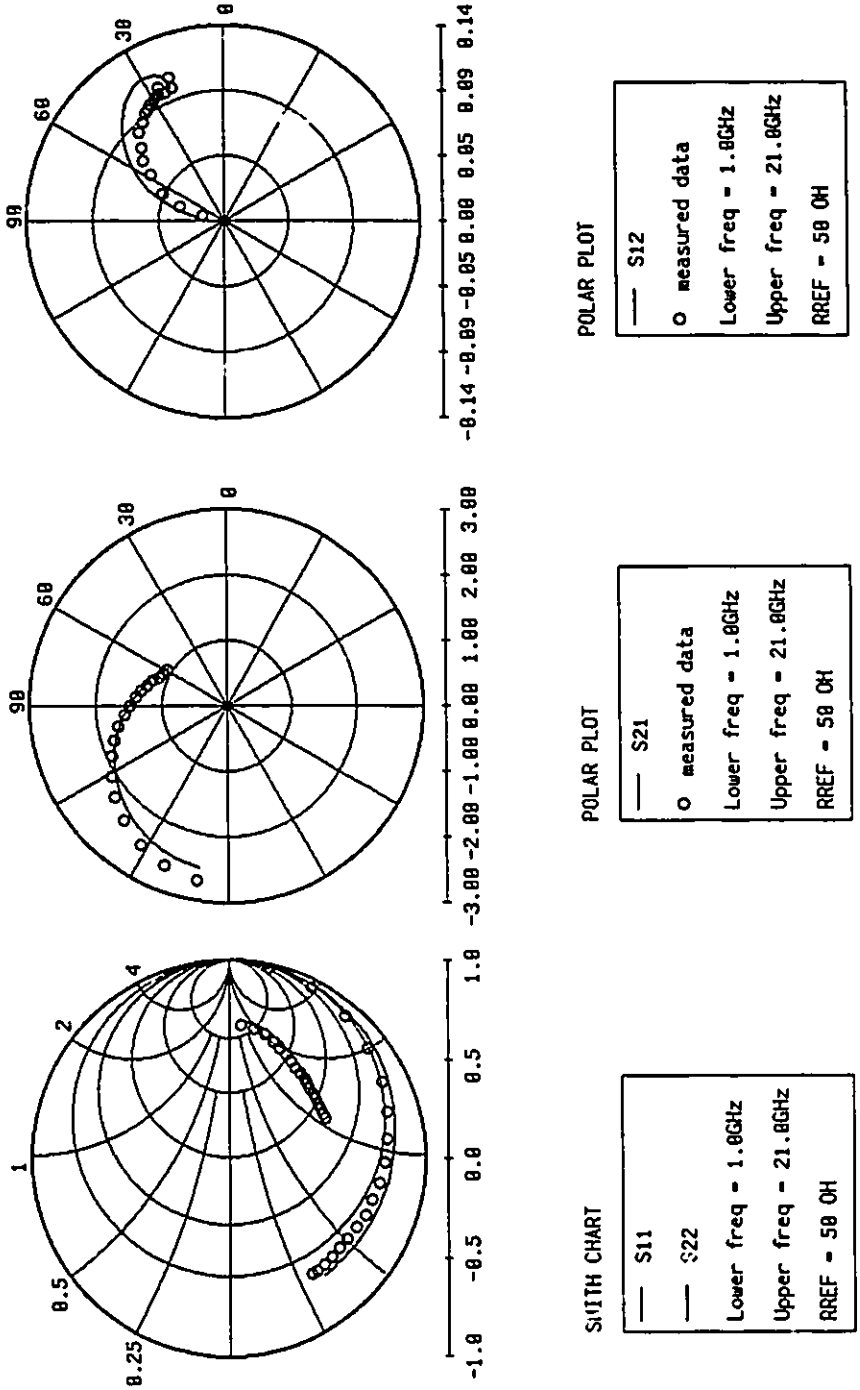

Fig. 2.10 Comparison of measured (o) and calculated (—) S parameters at bias point: $V_G = -0.84$V, $V_D = 5$V for parameter extraction.

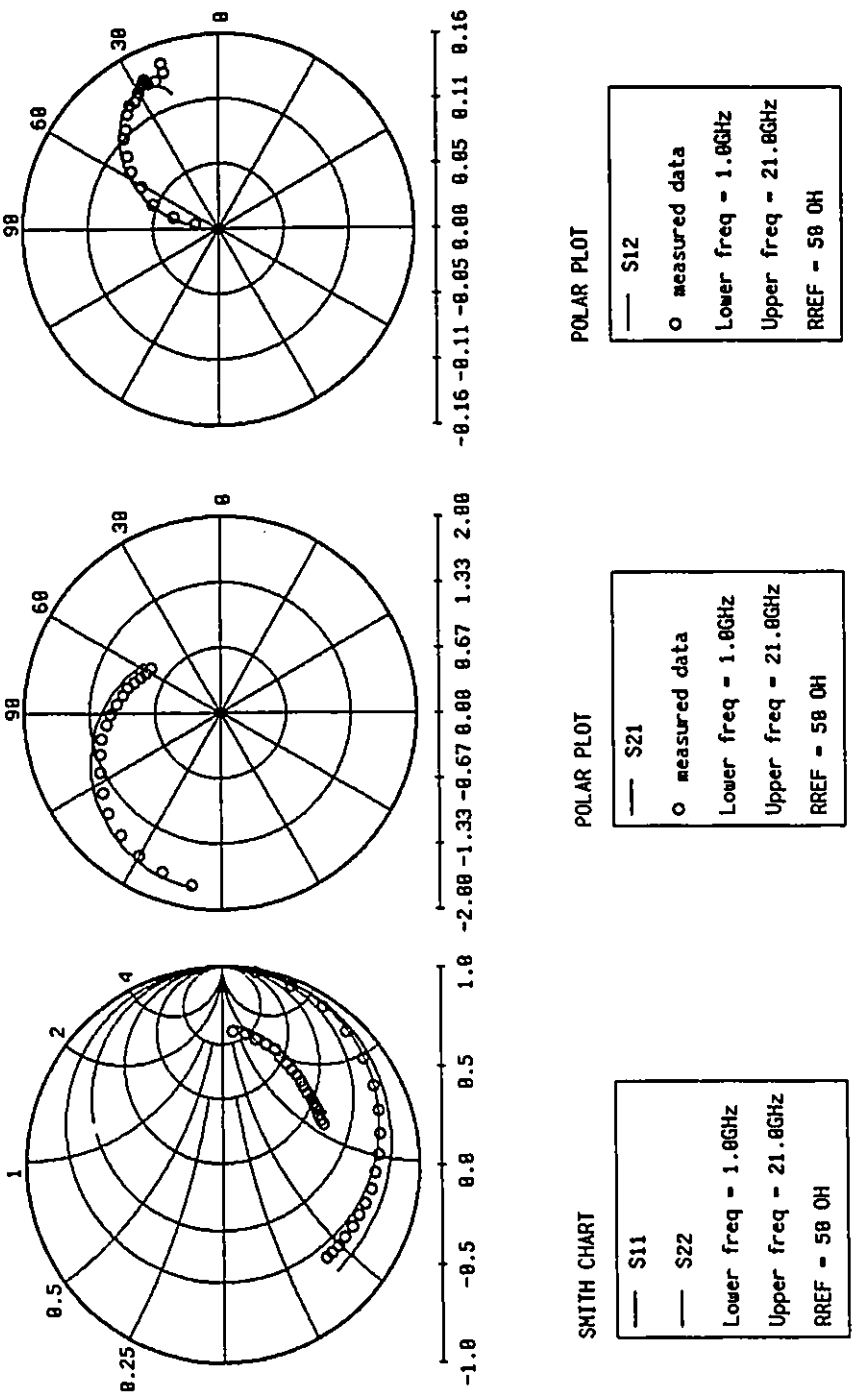

Fig. 2.11 Comparison of measured (o) and calculated (—) S parameters at bias point: $V_G = -1.54V$, $V_D = 5V$ for parameter extraction.

parameters were kept fixed. In the second stage both the intrinsic and extrinsic parameters were optimized starting from the result of the first stage. The entire parameter extraction process took approximately 5 CPU minutes and 30 iterations on a Sun SPARCstation 1. Optimizable extrinsic and intrinsic parameters before and after optimization are listed in Table 2.2. The measured [140] and simulated S parameters at the three bias points are shown in Fig. 2.9-2.11.

2.5 CONCLUSIONS

In this chapter, we described the approaches for physics-based analytical MESFET modeling. The Khatibzadeh and Trew model has been addressed in detail. The model has been exemplified by a comparison of measured and simulated DC characteristics and a parameter extraction example.

It should be pointed out that extracting parameter values by simultaneously optimizing a large number of parameters may lead to non-unique results. Some parameter values may become non-physical due to factors such as model simplifications, insufficient measurements or measurement errors. Therefore, model tuning, keeping the parameters within their physical limits, or parameter control, may be necessary. Based on practical knowledge of the device, these concepts can be accommodated in parameter extraction by applying constraints to the parameters being optimized.

Chapter 3

HARMONIC BALANCE NONLINEAR CIRCUIT ANALYSIS

3.1 INTRODUCTION

The analysis of nonlinear circuits is much more complicated than that of linear circuits. A variety of techniques for analyzing nonlinear circuits has been developed. These methods can be divided into three categories: time-domain simulation, frequency-domain simulation and mixed frequency/time-domain simulation as indicated by Gilmore and Steer (1991) [58].

Time-domain simulation methods try to solve the circuit equations entirely in the time domain using numerical methods. There are three major techniques: direct methods, associated discrete circuit model approaches and shooting methods (Gilmore and Steer (1991) [58]). The direct methods analyze the nonlinear circuits by directly solving the circuit differential equations using numerical integration (e.g., Chua and Lin (1975) [39], Skelboe (1980, 1982) [112,113], Vlach and Singhal (1983) [134], Jastrzebski and Sobhy (1984) [70], Sobhy and Jastrzebski (1985) [119]). In these methods, first, the nonlinear differential equations are converted into nonlinear algebraic equations through discretization of the time variable. Then the resulting algebraic equations are solved iteratively. The associated discrete circuit model approaches (e.g., Nagel and Pederson (1973) [90], Chua and Lin (1975) [39]) involve

the use of associated discrete circuit models. The circuit under consideration is modeled by representing the differential equations as finite difference equations at a number of time sampling points and the resulting set of nonlinear algebraic equations are solved at each time sample iteratively [58]. The shooting methods (e.g., Director (1971) [48], Aprille, Jr. and Trick (1971,1972) [3,4], Colon and Trick (1973) [40], Director and Current (1976) [49], Nakhla and Branin, Jr. (1977) [92]) iteratively simulate the circuit over one period interval. On each iteration, the initial condition is varied, attempting to make the signals at the end of the period exactly match those at the beginning. Although time-domain simulation methods are appropriate for the analysis of transient response of a nonlinear circuit, they are very time consuming for steady-state simulation. Particularly, they are not quite suitable for the simulation of microwave nonlinear circuits which usually have a number of distributed components and operate at steady-state (Kundert and Sangiovanni-Vincentelli (1986) [77]).

Frequency-domain simulation methods attempt to analyze the nonlinear circuits entirely in the frequency domain. A recent review of these techniques has been given by Steer, Chang and Rhyne (1991) [124]. There is a large number of frequency-domain analysis approaches in the literature. However, all these methods are based on functional expansions which enable the frequency components of the output spectrum to be calculated directly from the input spectrum. Frequency-domain simulation methods such as power series expansion analysis (e.g., Sea (1968) [109], Sea and Vacroux (1969) [110], Steer and Khan (1983) [123], Rhyne, Steer and Bates (1988) [102]), Volterra series analysis (e.g., Volterra (1930) [135], Bedrosian and Rice (1971) [31], Bussgang, Ehrman and Graham (1974) [35], Weiner and Spina (1980)

[136], Sandberg (1982) [107], Maas (1988) [84]) and spectral balance analysis (e.g., Ushida and Chua (1984) [132], Haywood and Chow (1988) [62], Chang, Steer and Rhyne (1989) [36]), have been used successfully for the analysis of microwave nonlinear circuits [37,63,67,79,89,101,128,130].

Mixed frequency/time-domain simulation methods analyze the nonlinear circuits in both time and frequency domains. The HB technique (e.g., Cunningham (1958) [42], Lindenlaub (1969) [82], Nakhla and Vlach (1976) [91], Mees (1981) [88], Rizzoli, Lipparini and Marazzi (1983) [104], Kundert and Sangiovanni-Vincentelli (1986) [77], Rizzoli, Cecchetti, Lipparini and Mastri (1988) [105], Gilmore and Steer (1991) [58,59]) is the basic method of mixed frequency/time-domain simulation. In HB simulation, the circuit is divided into a linear subcircuit and a nonlinear subcircuit. The linear subcircuit is evaluated in the frequency domain and the nonlinear subcircuit is calculated in the time domain. The transformation between the frequency domain and time domain is performed by the Fourier transform. The problem unknowns are the voltages or currents at DC and each harmonic in the frequency domain. The HB method is an efficient tool for simulation of steady-state responses of the circuits and has been extensively used in microwave circuit simulation [19,27,46,53,54,65]. Another method of mixed frequency/time-domain simulation is the waveform balance (or sample balance) approach. In the waveform balance method, as in the HB method, the linear subcircuit is analyzed in the frequency domain. The results are then transformed into the time domain by inverse Fourier transform and balanced with the same sample points of the nonlinear subcircuit. The problem unknowns are now the time-domain waveform samples.

This method has been used by Van Der Walt (1985) [133] for solving nonlinear pumping problems and by Hwang, Shih, Le and Itoh (1989) [69] for nonlinear modeling and verification of MMIC amplifiers.

In the following sections, the mechanism of the HB method is described. Nonlinear circuit analysis using the HB method is discussed. The integration of PBMs with the HB equation is presented. Finally, the Newton method for solving the HB equation is addressed.

3.2 THE HB METHOD

3.2.1 Fundamentals of the HB Method

As indicated by Kundert and Sangiovanni-Vincentelli (1986) [77], the HB method can be described as the extension of phasor analysis from linear to nonlinear differential equations. The HB method is used to find the steady-state solution to nonlinear differential equations by assuming the solutions to be real and periodic functions consisting of a linear combination of sinusoids. The differential equation is assumed to be such that, once the solution are substituted, the resulting equation can be rearranged into a sum of purely sinusoidal terms. Then the superposition and the orthogonality of sinusoids at different harmonics allow us to formulate the equations for each harmonic individually. These equations are solved by finding the coefficients of the sinusoids in the assumed solution. This results in the balancing of the algebraic equations at each harmonic.

Generally, a differential equation can be written as

$$f(x, \frac{dx}{dt}, \frac{d^2x}{dt^2}, ..., \frac{d^nx}{dt^n}, u) = 0 \tag{3.1}$$

where u is the stimulus periodic waveform of bounded variation with period of T_0, x is the unknown waveform to be found and f is continuous and real.

Assume that the solution x exists and is a real periodic waveform with period of T_0. Then x can be expressed as

$$x(t) = \sum_{k=-\infty}^{\infty} X(k)e^{jk\omega_0 t} \tag{3.2}$$

where

$$\omega_0 = \frac{2\pi}{T_0} \tag{3.3}$$

and

$$X(k) = \frac{1}{T_0}\int_0^{T_0} x(t)e^{-jk\omega_0 t}dt \tag{3.4}$$

are the angular frequency and the kth harmonic Fourier coefficient of $x(t)$, respectively.

Substituting the assumed solution x and its derivatives into (3.1) and writing the resulting equation as a Fourier series, we have

$$f(x, \frac{dx}{dt}, \frac{d^2x}{dt^2}, ..., \frac{d^nx}{dt^n}, u) = \sum_{k=-\infty}^{\infty} F(X, U, k)e^{jk\omega_0 t} = 0 \tag{3.5}$$

where

$$X = [\cdots\ X(-1)\ X(0)\ X(1)\ \cdots]^T \tag{3.6a}$$

$$U = [\cdots\ U(-1)\ U(0)\ U(1)\ \cdots]^T \tag{3.6b}$$

$$u(t) = \sum_{k=-\infty}^{\infty} U(k)e^{jk\omega_0 t} \tag{3.7}$$

Then X is obtained by solving the resulting nonlinear algebraic equations

$$F(X, U, k) = 0 \tag{3.8}$$

for all $k \in \{..., -1, 0, 1, ...\}$.

The principle of harmonic balance is that (3.8) is satisfied if and only if (3.1) is satisfied.

3.2.2 Solution Error of the HB Method

In the practical application of the HB method, a finite number of harmonics is used instead of an infinite number. The coefficients of the unused harmonics are assumed small enough to be neglected. Provided that the spectrum of $u(t)$ consists of N harmonics and $N \le H$, instead of (3.2), we use

$$x(t) = \sum_{k=-H}^{H} X(k)e^{jk\omega_0 t} \tag{3.9}$$

to approximate the exact solution of $x(t)$. Correspondingly, (3.5) is changed to

$$\sum_{k=-H}^{H} F(X, U, k)e^{jk\omega_0 t} = 0 \tag{3.10}$$

and (3.8) is solved for all $k \in \{-H, ..., -1, 0, 1, ..., H\}$.

This approximation by truncating the harmonics considered to a finite number H results in some solution errors. From (3.2) and (3.9), the resulting solution error can be expressed as

$$e_x = \sum_{k=-\infty}^{-(H+1)} X(k)e^{jk\omega_0 t} + \sum_{k=H+1}^{\infty} X(k)e^{jk\omega_0 t} \tag{3.11}$$

which depends on H and the magnitudes of the Fourier coefficients of the harmonics unused.

Fortunately, in many nonlinear microwave circuits, the magnitudes of the Fourier coefficients decrease with harmonics. The decreasing rate depends on the circuit nonlinearities. In order to obtain a certain accuracy, H should be selected according to the strength of the circuit nonlinearities.

Another solution error that is of interest in the HB method results from incomplete convergence problem in the iteration used to solve the nonlinear system of algebraic equations (3.8). If the Newton method is used, then this error can be ignored since it can be driven to an arbitrarily small level in relatively few iterations because of the method's quadratic convergence property (Kundert and Sangiovanni-Vincentelli (1986) [77]).

It should be noted that the size of the HB equations is directly proportional to the number of harmonics H. It is known that the trigonometric Fourier series exhibits slow convergence. Therefore, truncating the number of harmonic components, needed for efficiency or even feasibility, may strongly affect accuracy and convergence of the HB method, especially for high nonlinearities or excitations with many spectral components.

In nonlinear circuit simulation, as indicated in [77], all the variables and functions in the time domain are real and it is often desired not to use the negative harmonics in HB simulation. Under these conditions we need to split the complex quantities into their real and imaginary parts in order to use the Newton method to solve the complex HB equations. This is described in detail in the following sections.

3.3 CIRCUIT SIMULATION USING THE HB METHOD

The circuit nodal equations in the time domain can be written as [77]

$$f(v(t),\ t) = i(v(t)) + \frac{d}{dt}q(v(t)) + \int_{-\infty}^{t} y(t-\tau)v(\tau)d\tau + i_{ss}(t) = 0 \qquad (3.12)$$

where t is time, v is the vector of node voltage waveforms, i is the vector of the currents entering the nodes from nonlinear resistors or nonlinear voltage controlled current sources. q is the vector of the charges entering the nodes from nonlinear capacitors, y is the matrix-valued impulse response of linear components, and i_{ss} is the vector of independent current source waveforms.

To use the HB method, (3.12) is Fourier transformed into the frequency domain [77] as

$$F(V) = I(V) + j\Omega Q(V) + YV + I_{ss} = 0 \qquad (3.13)$$

where V, I_{ss}, I and Q are the vectors that contain the Fourier coefficients of the respective time-domain waveforms at each node and all harmonics, and Y is the nodal admittance matrix for the linear elements. Ω is the angular frequency matrix, as defined in [77].

In order to reduce the number of equations the circuit can be divided into a linear subcircuit, a nonlinear subcircuit and an excitation subcircuit, as shown in Fig. 3.1. Then, the quantities in (3.13) can be limited to the connection nodes with Y being the equivalent admittance matrix for the linear subcircuit. Further reduction can be achieved by replacing the linear and the excitation subcircuits by their Norton equivalent at the nonlinear ports. The state variables are then limited to the nonlinear port voltages, and I_{ss} and Y represent the Norton equivalent.

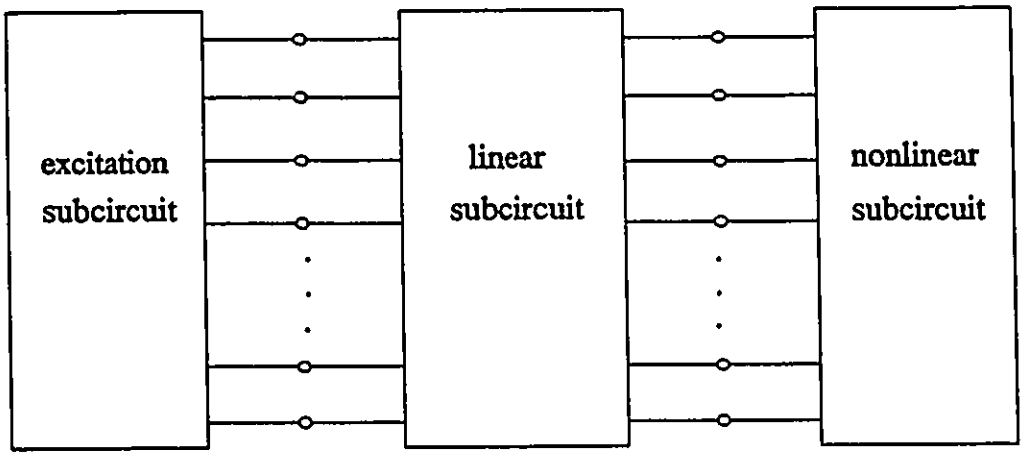

Fig. 3.1 Partition of a circuit for harmonic balance simulation.

To use the Newton method to solve the complex HB equation, (3.13) is reorganized into the following real equation form by splitting the real and imaginary parts of the complex quantities

$$\overline{F}(\overline{V}) = \overline{I}(\overline{V}) + \overline{\Omega}\,\overline{Q}(\overline{V}) + \overline{Y}\overline{V} + \overline{I}_{ss} = 0 \tag{3.14}$$

where a bar stands for real quantities resulting from their complex counterparts. For example,

$$\overline{V} = \begin{bmatrix} Real(V) \\ Imag(V) \end{bmatrix} \tag{3.15}$$

$$\overline{F} = \begin{bmatrix} Real(F) \\ Imag(F) \end{bmatrix} \tag{3.16}$$

$\overline{\Omega}$ is a frequency matrix which can be written as

$$\overline{\Omega} = \begin{bmatrix} & & & -\Omega(0) & & & \\ & & & & -\Omega(1) & & \\ & & & & & \cdots & \\ & & & & & & -\Omega(H) \\ \Omega(0) & & & & & & \\ & \Omega(1) & & & & & \\ & & \cdots & & & & \\ & & & \Omega(H) & & & \end{bmatrix} \tag{3.17}$$

where $\Omega(i)$ is a diagonal matrix whose diagonal elements are ω_i's and $\omega_0 = 0$ corresponds to DC component. H is the number of harmonics used in the simulation.

3.4 INTEGRATION OF PBMs WITH THE HB EQUATION

We now turn to the problem of efficient integration of the MESFET PBM described in Chapter 2 into the HB equation (3.14). The model is solved in the time domain for the gate, drain and source currents at given intrinsic voltages. In order to

do that, however, one must first determine the value of the intermediate parameter v_1 in (2.27b). In the original approaches of Yamaguchi and Kodera (1976) [137], Madjar and Rosenbaum (1981) [85] and Khatibzadeh and Trew (1988) [76], the "pseudo-static" DC condition $i_{dc} = -i_{sc}$ was used to solve for v_1. This condition is valid at DC only when the displacement currents of (2.32)-(2.34) assume zero values. For instantaneous currents under AC excitations both the conduction and displacement currents in (2.32)-(2.34) must be considered. Solving first for v_1 would require an additional iteration loop within the HB Newton iteration.

To avoid such a double iteration loop, our implementation treats v_1 of (2.27b) as an additional state variable, although it has no circuit interpretation. v_1 is directly integrated into the HB equation and allowed to vary w.r.t. time, RF input levels, and operating frequencies (Bandler, Zhang and Cai (1990) [23]), while satisfying the boundary conditions (2.27b). Including v_1 in the state variable vector requires augmenting (3.13) by the KCL equation for the pseudo-node "z", as indicated in Fig. 2.6. This procedure is applied to all FETs in the circuit.

To illustrate how the PBM is integrated with the HB equation, we consider a typical single FET circuit shown in Fig. 3.2. The circuit can be decomposed into a linear subcircuit, which includes all the matching circuits and extrinsic FET circuit, and a nonlinear intrinsic FET part as shown in Fig. 3.3. The state vector of this circuit can be defined as

$$v(\phi, t) = [v_{gs}(\phi, t)\ v_{ds}(\phi, t)\ v_1(\phi, t)]^T \tag{3.18}$$

where ϕ includes all the device and circuit parameters considered for simulation.

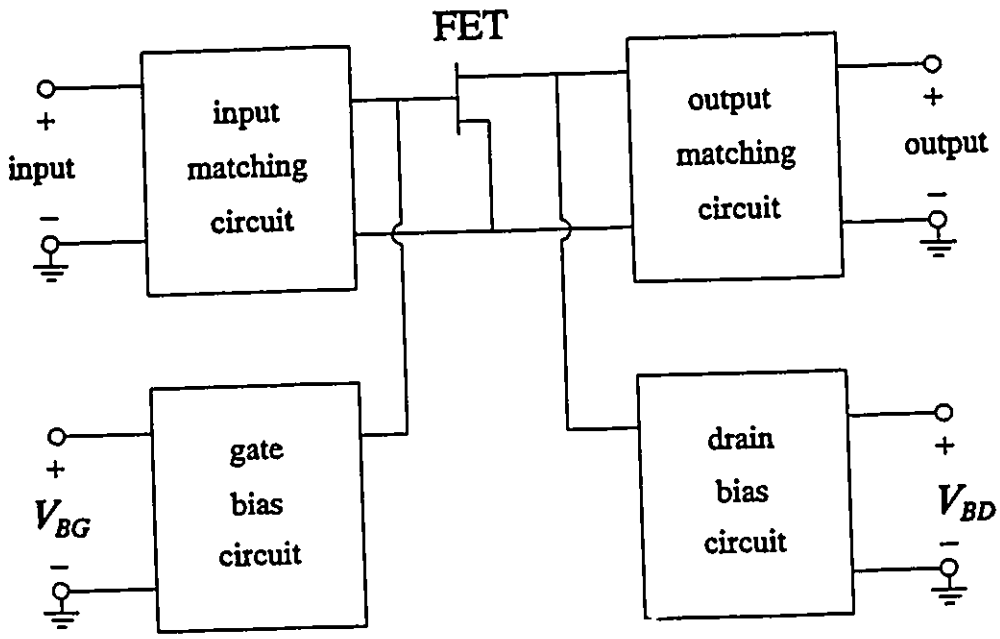

Fig. 3.2 Schematic representation of a single FET circuit.

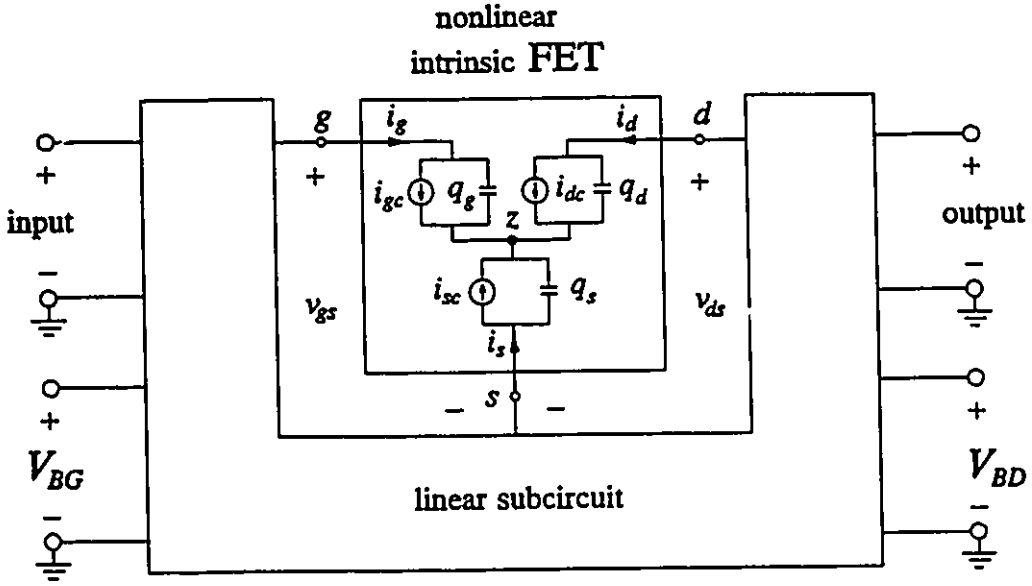

Fig. 3.3 Decomposition of a single FET circuit into a linear subcircuit and a nonlinear intrinsic FET.

The nonlinear current and charge vectors of (3.12) can be expressed as

$$i_c(\phi,\ v(\phi,\ t),\ t) = \begin{bmatrix} i_{gc}(\phi,\ v(\phi,\ t),\ t) \\ i_{dc}(\phi,\ v(\phi,\ t),\ t) \\ i_{sc}(\phi,\ v(\phi,\ t),\ t) \end{bmatrix} \tag{3.19}$$

and

$$q(\phi,\ v(\phi,\ t),\ t) = \begin{bmatrix} q_g(\phi,\ v(\phi,\ t),\ t) \\ q_d(\phi,\ v(\phi,\ t),\ t) \\ q_s(\phi,\ v(\phi,\ t),\ t) \end{bmatrix} \tag{3.20}$$

The HB equation (3.13) can be expressed as

$$\begin{aligned} F(\phi,\ V(\phi),\ k) &= A_1 I_c(\phi,\ V(\phi),\ k) + jB_1\Omega(k)Q(\phi,\ V(\phi),\ k) \\ &\quad + Y(\phi,\ k)V(\phi,\ k) + I_{ss}(k) = 0 \\ k &= 0,\ 1,\ \ldots,\ H \end{aligned} \tag{3.21}$$

where

$$I_c(\phi,\ V(\phi),\ k) = \begin{bmatrix} I_{gc}(\phi,\ V(\phi),\ k) \\ I_{dc}(\phi,\ V(\phi),\ k) \\ I_{sc}(\phi,\ V(\phi),\ k) \end{bmatrix} \tag{3.22}$$

$$Q(\phi,\ V(\phi),\ k) = \begin{bmatrix} Q_g(\phi,\ V(\phi),\ k) \\ Q_d(\phi,\ V(\phi),\ k) \\ Q_s(\phi,\ V(\phi),\ k) \end{bmatrix} \tag{3.23}$$

$$V(\phi,\ k) = \begin{bmatrix} V_{gs}(\phi,\ k) \\ V_{ds}(\phi,\ k) \\ V_1(\phi,\ k) \end{bmatrix} \tag{3.24}$$

$$Y(\phi,\ k) = \begin{bmatrix} Y_{gg}(\phi,\ k) & Y_{gd}(\phi,\ k) & 0 \\ Y_{dg}(\phi,\ k) & Y_{dd}(\phi,\ k) & 0 \\ 0 & 0 & 0 \end{bmatrix} \tag{3.25}$$

$$I_{ss}(k) = \begin{bmatrix} I_{ssg}(k) \\ I_{ssd}(k) \\ 0 \end{bmatrix} \tag{3.26}$$

This method has quadratic convergence, provided that the initial solution guess is close. The calculation of entries for the Jacobian matrix has been illustrated. The Jacobian matrix can be first used for solving the HB equation. The Jacobian matrix at the solution of the HB equation can then be reused in adjoint analysis for optimization which is discussed in Chapter 4.

$$\Omega(k) = \begin{bmatrix} \omega_k & 0 & 0 \\ 0 & \omega_k & 0 \\ 0 & 0 & \omega_k \end{bmatrix} \tag{3.27}$$

$$A_1 = B_1 = \begin{bmatrix} 1 & 0 & 0 \\ 0 & 1 & 0 \\ 1 & 1 & 1 \end{bmatrix} \tag{3.28}$$

and k is the harmonic index representing the kth harmonic, H is the number of harmonics considered in the HB simulation, $\omega_0 = 0$ corresponds to the DC component in the HB equation and

$$V(\phi) = \begin{bmatrix} V(\phi, 0) \\ V(\phi, 1) \\ \vdots \\ V(\phi, H) \end{bmatrix} \tag{3.29}$$

is the voltage vector to be solved for.

(3.21) can be expressed in the compact form

$$F(\phi, V(\phi)) = AI_c(\phi, V(\phi)) + jB\Omega Q(\phi, V(\phi)) + Y(\phi)V(\phi) + I_{ss} = 0 \tag{3.30}$$

where

$$I_c(\phi, V(\phi)) = \begin{bmatrix} I_c(\phi, V(\phi), 0) \\ I_c(\phi, V(\phi), 1) \\ \vdots \\ I_c(\phi, V(\phi), H) \end{bmatrix} \tag{3.31}$$

$$Q(\phi, V(\phi)) = \begin{bmatrix} Q(\phi, V(\phi), 0) \\ Q(\phi, V(\phi), 1) \\ \vdots \\ Q(\phi, V(\phi), H) \end{bmatrix} \tag{3.32}$$

$$Y(\phi) = \begin{bmatrix} Y(\phi, 0) & & & \\ & Y(\phi, 1) & & \\ & & \ddots & \\ & & & Y(\phi, H) \end{bmatrix} \tag{3.33}$$

$$I_{ss} = \begin{bmatrix} I_{ss}(0) \\ I_{ss}(1) \\ \vdots \\ I_{ss}(H) \end{bmatrix} \tag{3.34}$$

$$\Omega = \begin{bmatrix} \Omega(0) & & & \\ & \Omega(1) & & \\ & & \ddots & \\ & & & \Omega(H) \end{bmatrix} \tag{3.35}$$

$$A = \begin{bmatrix} A_1 & & & \\ & A_1 & & \\ & & \ddots & \\ & & & A_1 \end{bmatrix} \tag{3.36}$$

$$B = \begin{bmatrix} B_1 & & & \\ & B_1 & & \\ & & \ddots & \\ & & & B_1 \end{bmatrix} \tag{3.37}$$

In practice, the complex HB equation (3.30) is reorganized into the following real equation form by splitting its real and imaginary parts.

$$\overline{F}(\phi, \overline{V}(\phi)) = \overline{A}\,\overline{I}_c(\phi, \overline{V}(\phi)) + \overline{B}\,\overline{\Omega}\,\overline{Q}(\phi, \overline{V}(\phi)) + \overline{Y}(\phi)\overline{V}(\phi) + \overline{I}_{ss} = 0 \tag{3.38}$$

where

$$\overline{F}(\phi, \overline{V}(\phi)) = \begin{bmatrix} F^R(\phi, \overline{V}(\phi), 0) \\ F^R(\phi, \overline{V}(\phi), 1) \\ \vdots \\ F^R(\phi, \overline{V}(\phi), H) \\ F^I(\phi, \overline{V}(\phi), 0) \\ F^I(\phi, \overline{V}(\phi), 1) \\ \vdots \\ F^I(\phi, \overline{V}(\phi), H) \end{bmatrix} \tag{3.39}$$

$$\overline{I}_c(\phi, \overline{V}(\phi)) = \begin{bmatrix} I_c^R(\phi, \overline{V}(\phi), 0) \\ I_c^R(\phi, \overline{V}(\phi), 1) \\ \vdots \\ I_c^R(\phi, \overline{V}(\phi), H) \\ I_c^I(\phi, \overline{V}(\phi), 0) \\ I_c^I(\phi, \overline{V}(\phi), 1) \\ \vdots \\ I_c^I(\phi, \overline{V}(\phi), H) \end{bmatrix} \tag{3.40}$$

$$\overline{Q}(\phi, \overline{V}(\phi)) = \begin{bmatrix} Q^R(\phi, \overline{V}(\phi), 0) \\ Q^R(\phi, \overline{V}(\phi), 1) \\ \vdots \\ Q^R(\phi, \overline{V}(\phi), H) \\ Q^I(\phi, \overline{V}(\phi), 0) \\ Q^I(\phi, \overline{V}(\phi), 1) \\ \vdots \\ Q^I(\phi, \overline{V}(\phi), H) \end{bmatrix} \tag{3.41}$$

$$\overline{V}(\phi) = \begin{bmatrix} V^R(\phi, 0) \\ V^R(\phi, 1) \\ \vdots \\ V^R(\phi, H) \\ V^I(\phi, 0) \\ V^I(\phi, 1) \\ \vdots \\ V^I(\phi, H) \end{bmatrix} \tag{3.42}$$

$$\overline{I}_{ss} = \begin{bmatrix} I_{ss}^R(0) \\ I_{ss}^R(1) \\ \vdots \\ I_{ss}^R(H) \\ I_{ss}^I(0) \\ I_{ss}^I(1) \\ \vdots \\ I_{ss}^I(H) \end{bmatrix} \tag{3.43}$$

$$\overline{Y}(\phi) = \begin{bmatrix} Y^R(\phi, 0) & & & -Y^I(\phi, 0) & & \\ & Y^R(\phi, 1) & & & -Y^I(\phi, 1) & \\ & & \ddots & & & \ddots \\ & & Y^R(\phi, H) & & & -Y^I(\phi, H) \\ Y^I(\phi, 0) & & & Y^R(\phi, 0) & & \\ & Y^I(\phi, 1) & & & Y^R(\phi, 1) & \\ & & \ddots & & & \ddots \\ & & Y^I(\phi, H) & & & Y^R(\phi, H) \end{bmatrix} \tag{3.44}$$

$$\overline{\Omega} = \begin{bmatrix} & & & -\Omega(0) & & \\ & & & & -\Omega(1) & \\ & & & & & \ddots \\ & & & & & -\Omega(H) \\ \Omega(0) & & & & & \\ & \Omega(1) & & & & \\ & & \ddots & & & \\ & & \Omega(H) & & & \end{bmatrix} \tag{3.45}$$

$$\overline{A} = \begin{bmatrix} A & \\ & A \end{bmatrix} \tag{3.46}$$

$$\overline{B} = \begin{bmatrix} B & \\ & B \end{bmatrix} \tag{3.47}$$

and the superscripts R and I represent respectively the real and imaginary parts of the corresponding complex component.

The solution of (3.38) ensures current continuity for all harmonics, i.e.,

$$\overline{I}_g + \overline{I}_d + \overline{I}_s = 0 \tag{3.48}$$

This ensures the current continuity condition

$$i_g(t) + i_d(t) + i_s(t) = 0 \tag{3.49}$$

in the time domain. Therefore, our formulation is valid not only for DC but also for small- and large-signal RF operations, and it does not require a double iteration loop.

3.5 NEWTON METHOD FOR SOLVING THE HB EQUATION

The Newton update for solving the HB equation can be written as

$$\overline{V}_{new}(\phi) = \overline{V}_{old}(\phi) - \left[\overline{J}(\phi, \overline{V}_{old}(\phi))\right]^{-1}\overline{F}(\phi, \overline{V}_{old}(\phi)) \tag{3.50}$$

where $\overline{J}(\phi, \overline{V}(\phi))$ is the Jacobian matrix used in the algorithm. From (3.38), we see that the Jacobian has the form

$$\overline{J}(\phi, \overline{V}(\phi)) = \overline{A}\left[\frac{\partial \overline{I}_c^T(\phi, \overline{V}(\phi))}{\partial \overline{V}(\phi)}\right]^T + \overline{B\Omega}\left[\frac{\partial \overline{Q}^T(\phi, \overline{V}(\phi))}{\partial \overline{V}(\phi)}\right]^T + \overline{Y}(\phi) \tag{3.51}$$

Note that in solving the HB equation, ϕ is constant and $\overline{V}(\phi)$ is variable. Following [77], in order to calculate the entries of $\overline{J}(\phi, \overline{V}(\phi))$, we must first obtain the time-domain derivatives of i_c and q w.r.t. v. The time-domain derivatives of i_c and q w.r.t. v are evaluated by differentiating the corresponding terms of (2.32)-(2.34) w.r.t. v. After the derivatives of i_c and q w.r.t. v are obtained, the entries of the Jacobian matrix $\overline{J}$ can be evaluated by the Fourier transform.

Since there are three state variables v_{gs}, v_{ds} and v_1, the entries of $\overline{J}(\phi, \overline{V}(\phi))$ include the derivatives of $\overline{I}_c$ and $\overline{Q}$ w.r.t. $\overline{V}_{gs}$, $\overline{V}_{ds}$ and $\overline{V}_1$. For instance, if $\overline{I}_{dc}(\phi, \overline{V}(\phi), k)$ denotes the split real and imaginary parts of the kth harmonic component of the drain conduction current and $\overline{V}_1(\phi, l)$ represents the split real and imaginary parts of the lth harmonic component of variable v_1, then

$$\frac{\partial \overline{I}_{dc}^T(\phi, \overline{V}(\phi), k)}{\partial \overline{V}_1(\phi, l)} = \begin{bmatrix} G_{v_1}^R(k-l) + G_{v_1}^R(k+l) & G_{v_1}^I(k+l) - G_{v_1}^I(k-l) \\ G_{v_1}^I(k-l) + G_{v_1}^I(k+l) & G_{v_1}^R(k-l) - G_{v_1}^R(k+l) \end{bmatrix}^T \tag{3.52}$$

where

$$G^R_{v_1}(i) \triangleq \frac{1}{T_0}\int_0^{T_0} \frac{\partial i_{dc}(\phi,\ v(\phi),\ t)}{\partial v_1(\phi,\ t)} \cos(\omega_i t)dt \tag{3.53a}$$

and

$$G^I_{v_1}(i) \triangleq -\frac{1}{T_0}\int_0^{T_0} \frac{\partial i_{dc}(\phi,\ v(\phi),\ t)}{\partial v_1(\phi,\ t)} \sin(\omega_i t)dt \tag{3.53b}$$

and ω_i is the ith harmonic frequency. T_0 is the fundamental period. The time-domain derivative in (3.53) is evaluated by differentiating (2.35) w.r.t. v_1, i.e.,

$$\frac{\partial i_{dc}}{\partial v_1} = -qW\int_0^a \left[\frac{\partial \mu}{\partial E}\frac{\partial E}{\partial v_1}nE_x + \mu\frac{\partial n}{\partial v_1}E_x + \mu n\frac{\partial E_x}{\partial v_1} + D\frac{\partial(\nabla_x n)}{\partial v_1}\right]_{x=L} dy \tag{3.54}$$

(3.54) involves additional integrations, so in our actual implementation the perturbation technique is used instead.

The Jacobian matrix $\overline{J}$ is used in (3.50) to solve the HB equation iteratively.

3.6 CONCLUSIONS

The fundamental techniques of the HB method and its solution error has been discussed. Nonlinear circuit analysis using the HB method has been addressed. The PBMs are integrated with the HB equation which is demonstrated by the formulation of the HB equation for a typical single FET circuit. One of the advantages of integrating PBMs with the HB equation is that the effect of device physical parameters on circuit performances can be directly obtained. This provides an opportunity for design engineers to foresee the circuit responses before the device and circuit are actually fabricated. It facilitates physics-based circuit optimization which is able to directly optimize the device physical parameters.

An efficient Newton method for solving the HB equation has been described.

Chapter 4

GRADIENT-BASED OPTIMIZATION FOR CIRCUIT DESIGN

4.1 INTRODUCTION

Gradient-based optimization is one of the most efficient techniques for circuit design. Many powerful gradient-based algorithms have been developed in recent years for nonlinear optimization and applied to circuit CAD problems. For example, Bandler, Kellermann and Madsen (1985) [12] presented a minimax algorithm for microwave circuit design. Bandler, Chen and Daijavad (1986) [13] presented an efficient ℓ_1 algorithm for microwave device modeling. Bandler and Chen (1988) [15] reviewed optimization techniques suitable for modern microwave CAD and addressed realistic design and modeling problems. Due to their effectiveness and efficiency, gradient-based optimization methods have gained increasing applications in performance-driven and yield-driven circuit design.

Gradient calculation is the basis of gradient-based optimization. The algorithms need the gradients of all circuit responses considered with respect to all design variables which are usually obtained by sensitivity analysis. There is a number of sensitivity analysis techniques in the literature. Generally, they can be classified into two categories: exact sensitivity techniques and approximate sensitivity techniques. The exact sensitivity techniques calculate the gradients analytically and

explicitly. This method is accurate and efficient. However, for some applications, explicit sensitivity expressions may not be available or may be very difficult and tedious to obtain, especially for large-scale circuits. Therefore, exact sensitivity may not be suitable for general-purpose CAD software systems. Approximate sensitivity techniques estimate the gradients using numerical approximation methods. Though this approach is less accurate than exact sensitivity techniques, it provides a powerful tool for sensitivity analysis used for circuit design. It is very suitable for general-purpose CAD. Some methods for sensitivity analysis using both exact and approximate sensitivity techniques are discussed in this chapter.

Circuit optimization with the HB method has become an important tool for nonlinear microwave circuit design. It has been successfully applied to both performance-driven circuit design (e.g., Filicori, Monaco and Naldi (1979) [54], Rizzoli, Lipparini and Marazzi (1983) [104], Gilmore (1986) [57], Bandler, Zhang and Cai (1990) [23]) and yield-driven design (e.g., Bandler, Zhang, Song and Biernacki (1990) [24]). Circuit optimization with the HB method relies on efficient gradient calculations in the frequency domain. Bandler, Zhang and Biernacki proposed the *E*xact *A*djoint *S*ensitivity *T*echnique (EAST) (1988) [18] and *F*easible *A*djoint *S*ensitivity *T*echnique (FAST) (1989) [21] for HB simulation and optimization. FAST is an efficient technique for high-speed gradient calculation. It is described in detail in this chapter.

Microwave circuit design optimization with ECMs has been extensively studied and is available in some commercial software packages. Such optimization adjusts passive components to achieve desired circuit performance or yield with fi ·ed

active devices. Little work has been devoted so far to design optimization with PBMs. This chapter addresses aspects of physics-based circuit design using gradient optimization and HB simulation.

Finally, a broadband feedback amplifier design and a frequency doubler design are provided as examples to demonstrate small-signal and large-signal circuit design with PBMs.

4.2 SENSITIVITY ANALYSIS TECHNIQUES

To facilitate efficient gradient-based optimization for circuit design we need to provide the optimizer with gradients, i.e., the partial derivatives of circuit responses w.r.t. design variables. This is commonly referred to as sensitivity analysis. In this section, several sensitivity analysis techniques are discussed.

4.2.1 Perturbation Approximate Sensitivity Technique [16]

The most popular method of sensitivity analysis is the conventional *P*erturbation *A*pproximate *S*ensitivity *T*echnique (PAST) as described by Bandler, Chen, Daijavad and Madsen (1988) [16]. Let $f(\phi)$ denote a generic response function of the circuits and ϕ_i be a generic design variable in ϕ, then in PAST, the first-order derivative of $f(\phi)$ w.r.t. ϕ_i is estimated by

$$\frac{\partial f(\phi)}{\partial \phi_i} \approx \frac{f(\phi + \Delta\phi_i u_i) - f(\phi)}{\Delta\phi_i} \tag{4.1}$$

where $\Delta\phi_i u_i$ denotes the perturbation of the ith variable, $\Delta\phi_i$ is the perturbation size and u_i is a unit vector which has 1 in the ith position and zeros elsewhere. This

method is straightforward and easy to implement. However, it may not be accurate enough and the computational effort involved, especially for large-scale problems, may be prohibitive.

4.2.2 Integrated Gradient Approximation Technique [16]

Bandler, Chen, Daijavad and Madsen (1988) [16] proposed an *I*ntegrated *G*radient *A*pproximation *T*echnique (IGAT) which utilizes the Broyden update (Broyden (1965) [34])

$$\nabla f(\phi_{new}) = \nabla f(\phi_{old}) + \frac{f(\phi_{new}) - f(\phi_{old}) - (\nabla f(\phi_{old}))^T \Delta\phi}{\Delta\phi^T \Delta\phi} \Delta\phi \,. \tag{4.2}$$

and the special iteration of Powell (1970) [94]. Perturbations with (4.1) are used to obtain an initial approximation as well as regular corrections. ϕ_{old} and ϕ_{new} are two different points and $\Delta\phi = \phi_{new} - \phi_{old}$. The values of the function f at ϕ_{old} and ϕ_{new} are assumed available. If ϕ_{old} and ϕ_{new} are iterates of the optimization process, the gradient update requires no additional function evaluations, regardless of the dimension of the problem.

IGAT is robust and has been applied to both microwave circuit nominal design [16] and yield optimization (Bandler, Zhang, Song and Biernacki (1990) [24]).

4.2.3 Exact Adjoint Sensitivity Technique [18]

Efficient and accurate sensitivity analysis for HB can be achieved by *E*xact *A*djoint *S*ensitivity *T*echnique (EAST) developed by Bandler, Zhang and Biernacki (1988) [18], which is a generalization of the linear adjoint sensitivity analysis

technique.

The general formula for computing the exact sensitivity of an output voltage V_{out} w.r.t. a parameter ϕ_i of an element at branch b can be expressed by [18]

$$\frac{\partial \overline{V}_{out}}{\partial \phi_i} = \begin{cases} -\sum_k Real\left[\hat{V}_b(k)V_b^*(k)G_b^*(k)\right] & \text{if } \phi_i \in \text{linear subcircuit} \\ -\sum_k Real\left[\hat{V}_b(k)G_b^*(k)\right] & \text{if } \phi_i \in \text{NVCCS or NR or real part of a CDS} \\ -\sum_k Imag\left[\hat{V}_b(k)G_b^*(k)\right] & \text{if } \phi_i \in \text{NC or imaginary part of a CDS} \end{cases} \tag{4.3}$$

where the complex quantities $V_b(k)$ and $\hat{V}_b(k)$ are the voltages of branch b at harmonic k and are obtained from the original and adjoint networks, respectively. $G_b(k)$ denotes the sensitivity expression of the element containing variable ϕ_i [18]. * stands for the conjugate of a complex number, NVCCS for nonlinear voltage controlled current source, NR for nonlinear resistor, NC for nonlinear capacitor and CDS for complex driving source. This technique exhibits high accuracy and computational efficiency but suffers from implementation complexity.

4.2.4 Feasible Adjoint Sensitivity Technique [21]

To combine the efficiency of EAST and simplicity of PAST, Bandler, Zhang and Biernacki (1989) [21] proposed the *F*easible *A*djoint *S*ensitivity *T*echnique (FAST). It features high speed gradient computation as well as ease in implementation. It is particularly suitable for general purpose CAD programs.

Suppose we have

$$h(\phi, y) = 0 \tag{4.4}$$

and want to find $\frac{\partial y}{\partial \phi_i}$. Differentiating both sides of (4.4) w.r.t. ϕ_i, gives

$$\frac{\partial h(\phi, y)}{\partial \phi_i} + \left[\frac{\partial h^T(\phi, y)}{\partial y}\right]^T \frac{\partial y}{\partial \phi_i} = 0 \tag{4.5}$$

From (4.5), we can find that

$$\frac{\partial y}{\partial \phi_i} = - J^{-1} \frac{\partial h(\phi, y)}{\partial \phi_i} \tag{4.6}$$

where

$$J = \left[\frac{\partial h^T(\phi, y)}{\partial y}\right]^T \tag{4.7}$$

is the Jacobian matrix. If we use the approximation

$$\frac{\partial h(\phi, y)}{\partial \phi_i} \approx \frac{h(\phi+\Delta\phi_i u_i, y) - h(\phi, y)}{\Delta\phi_i} = \frac{h(\phi+\Delta\phi_i u_i, y)}{\Delta\phi_i} \tag{4.8}$$

then (4.6) becomes

$$\frac{\partial y}{\partial \phi_i} \approx - J^{-1} \frac{h(\phi+\Delta\phi_i u_i, y)}{\Delta\phi_i} \tag{4.9}$$

Now, applying (4.9) to the HB equation

$$\overline{F}(\phi, \overline{V}) = 0 \tag{4.10}$$

as indicated in (3.38), we have

$$\frac{\partial \overline{V}}{\partial \phi_i} \approx - \overline{J}^{-1} \frac{\overline{F}(\phi+\Delta\phi_i u_i, \overline{V})}{\Delta\phi_i} \tag{4.11}$$

where the Jacobian matrix

$$\overline{J} = \left[\frac{\partial \overline{F}^T(\phi, \overline{V})}{\partial \overline{V}}\right]^T \tag{4.12}$$

is evaluated by (3.51). (4.11) is much easier to implement than (4.3) in EAST. The

function $\overline{F}$ in (4.11) is evaluated by perturbation and can be readily implemented. The Jacobian matrix $\overline{J}$ is available at the solution of the HB equation (4.10). The only additional computational effort involved is one simulation of $\overline{F}$ with $\phi = \phi + \Delta\phi$. Therefore, it is feasible and efficient for sensitivity analysis in general-purpose microwave CAD.

4.3 INTEGRATION OF FAST WITH PBMs

We choose FAST here for incorporating PBMs into efficient gradient-based optimization.

Consider a vector of circuit responses

$$R(\phi) = \Re(\phi, \overline{V}(\phi)) \tag{4.13}$$

which may include output voltages, currents, powers, power gains, etc. Let S be a set of design specifications. Then the objective function for a design problem can be expressed as

$$U(\phi) = U(R(\phi), S) \tag{4.14}$$

The corresponding design optimization problem is to

$$\underset{\phi}{minimize} \quad U(\phi) \tag{4.15}$$

In order to use a gradient-based optimizer to solve (4.15), the derivatives of U w.r.t. each variable ϕ_i in ϕ need to be calculated. Let ϕ_i be a generic design variable such as a device dimension or doping density. The sensitivity of U w.r.t. ϕ_i can be obtained by differentiating (4.14) w.r.t. ϕ_i

$$\frac{\partial U}{\partial \phi_i} = \left[\frac{\partial U}{\partial \vec{R}}\right]^T \frac{\partial R}{\partial \phi_i} \tag{4.16}$$

$\frac{\partial U}{\partial R}$ depends on the form of the objective function. $\frac{\partial R}{\partial \phi_i}$ can be derived from (4.13) as

$$\frac{\partial R(\phi)}{\partial \phi_i} = \frac{\partial \Re(\phi, \overline{V}(\phi))}{\partial \phi_i} + \left[\frac{\partial \Re^T(\phi, \overline{V}(\phi))}{\partial \overline{V}(\phi)}\right]^T \frac{\partial \overline{V}(\phi)}{\partial \phi_i} \tag{4.17}$$

where $\frac{\partial \Re}{\partial \phi_i}$ and $\frac{\partial \Re^T}{\partial \overline{V}}$ may be calculated analytically or by perturbation. The FAST technique is applied to calculate $\frac{\partial \overline{V}}{\partial \phi_i}$.

Assume that the solution of the HB equation is $\overline{V} = \overline{V}_{sol}$, i.e.,

$$\overline{F}(\phi, \overline{V}_{sol}) = 0 \tag{4.18}$$

The FAST technique approximates the gradient by

$$\frac{\partial \overline{V}}{\partial \phi_i} \approx -\overline{J}^{-1} \frac{\overline{F}(\phi + \Delta\phi_i u_i, \overline{V}_{sol})}{\Delta \phi_i} \tag{4.19}$$

If the response in (4.13) is an output voltage, which is very common in circuit design, the sensitivity analysis using FAST is even more straightforward. Suppose the output voltage $\overline{V}_{out}$ can be computed from $\overline{V}$ as

$$\overline{V}_{out} = \overline{e}^T \overline{V} \tag{4.20}$$

where $\overline{e}$ is a vector containing 1's and 0's used to select the real or imaginary part of the output voltage of interest. Then the approximate sensitivity of the output voltage $\overline{V}_{out}$ w.r.t. ϕ_i can be calculated by

$$\frac{\partial \overline{V}_{out}}{\partial \phi_i} \approx -\hat{\overline{V}}^T \frac{\overline{F}(\phi + \Delta\phi_i u_i, \overline{V}_{sol})}{\Delta \phi_i} \tag{4.21}$$

Here $\hat{\overline{V}}$ is obtained by solving the adjoint system

$$\overline{J}^T \hat{\overline{V}} = \overline{e} \tag{4.22}$$

where $\overline{J}$ is the Jacobian matrix at the solution of the HB equation. In an efficient

implementation, it can be available in the form of LU factors.

As an example, consider the sensitivity of an output voltage w.r.t. the gate width W of a FET, i.e., $\frac{\partial \overline{V}_{out}}{\partial W}$. We need to obtain the adjoint solution $\hat{\overline{V}}$ and evaluate the HB residual function $\overline{F}(W+\Delta W, \overline{V}_{sol})$. By reusing the Jacobian matrix available at the HB solution, the adjoint system can be solved with relatively little additional effort. The HB residual function is evaluated from (3.38) as

$$\overline{F}(W+\Delta W, \overline{V}_{sol}) = \overline{A}\,\overline{I}_c(W+\Delta W, \overline{V}_{sol}) + \overline{B}\,\overline{\Omega Q}(W+\Delta W, \overline{V}_{sol}) + \overline{Y}\,\overline{V}_{sol} + \overline{I}_{ss} \quad (4.23)$$

Note that $\overline{V}_{sol}$ is constant at this stage, so no iterations are necessary. For instance, i_{dc}, needed to evaluate the first term in the right hand side of (4.23), can be calculated by replacing W by $W + \Delta W$ in (2.35), where E and n are determined from v_{sol}, the inverse Fourier transform of $\overline{V}_{sol}$. The resulting i_{dc} is then transformed to the frequency domain and used in (4.23). This provides a high speed yet simple gradient evaluation procedure for gradient optimizers.

4.4 ALGORITHM FOR OPTIMIZATION

The algorithm for optimization of a nonlinear MESFET circuit using FAST and HB can be described as follows:

Step 1 Initialization for Optimization.

Step 1.1 Input the circuit topology, design specifications, matching circuit elements and device physical parameters.

Step 1.2 Initialize the design variable vector ϕ. Assign values to all parameters in the circuit including the physical parameters and parasitic parameters of the FETs.

Step 2 Time Domain Simulation.

Step 2.1 Initialize $\overline{V}(\phi)$.

Step 2.2 Convert $\overline{V}(\phi)$ to $v(\phi, t)$, i.e., v_1, v_{gs} and v_{ds}, using the inverse Fourier transform. Calculate the gate, drain and source conduction currents $i_c(\phi, v(\phi, t), t)$ and gate, drain and source total charges $q(\phi, v(\phi, t), t)$.

Step 3 Frequency Domain Simulation.

Step 3.1 Use the forward Fourier transform to obtain $\overline{I}_c(\phi, \overline{V}(\phi))$ and $\overline{Q}(\phi, \overline{V}(\phi))$ from $i(\phi, v(\phi, t), t)$ and $q(\phi, v(\phi, t), t)$.

Step 3.2 Solve the HB equation using the Newton update (3.50). Note that at this stage ϕ is constant and $\overline{V}(\phi)$ is variable. If $\overline{V}(\phi)$ is the solution of the HB equation $\overline{F}(\phi, \overline{V}(\phi)) = 0$, then go to *Step 4*. Otherwise, update $\overline{V}(\phi)$ and go to *Step 2.2*.

Step 4 Optimization of Parameters ϕ.

Step 4.1 If ϕ is optimal, stop.

Step 4.2 Solve the adjoint system (4.22) and calculate $\frac{\partial \overline{V}_{out}(\phi)}{\partial \phi_i}$ with (4.21) or calculate $\frac{\partial \overline{V}(\phi)}{\partial \phi_i}$ with (4.19) using the Jacobian matrix at the solution of the HB equation. Evaluate $\frac{\partial R(\phi)}{\partial \phi_i}$ using (4.17) and then $\frac{\partial U(\phi)}{\partial \phi_i}$ using (4.16), for $i = 1, 2, ..., n$, where n is the number of optimizable parameters.

Step 4.3 Update ϕ according to the optimization algorithm. Go to *Step 2*.

This algorithm is illustrated by the flowchart in Fig. 4.1.

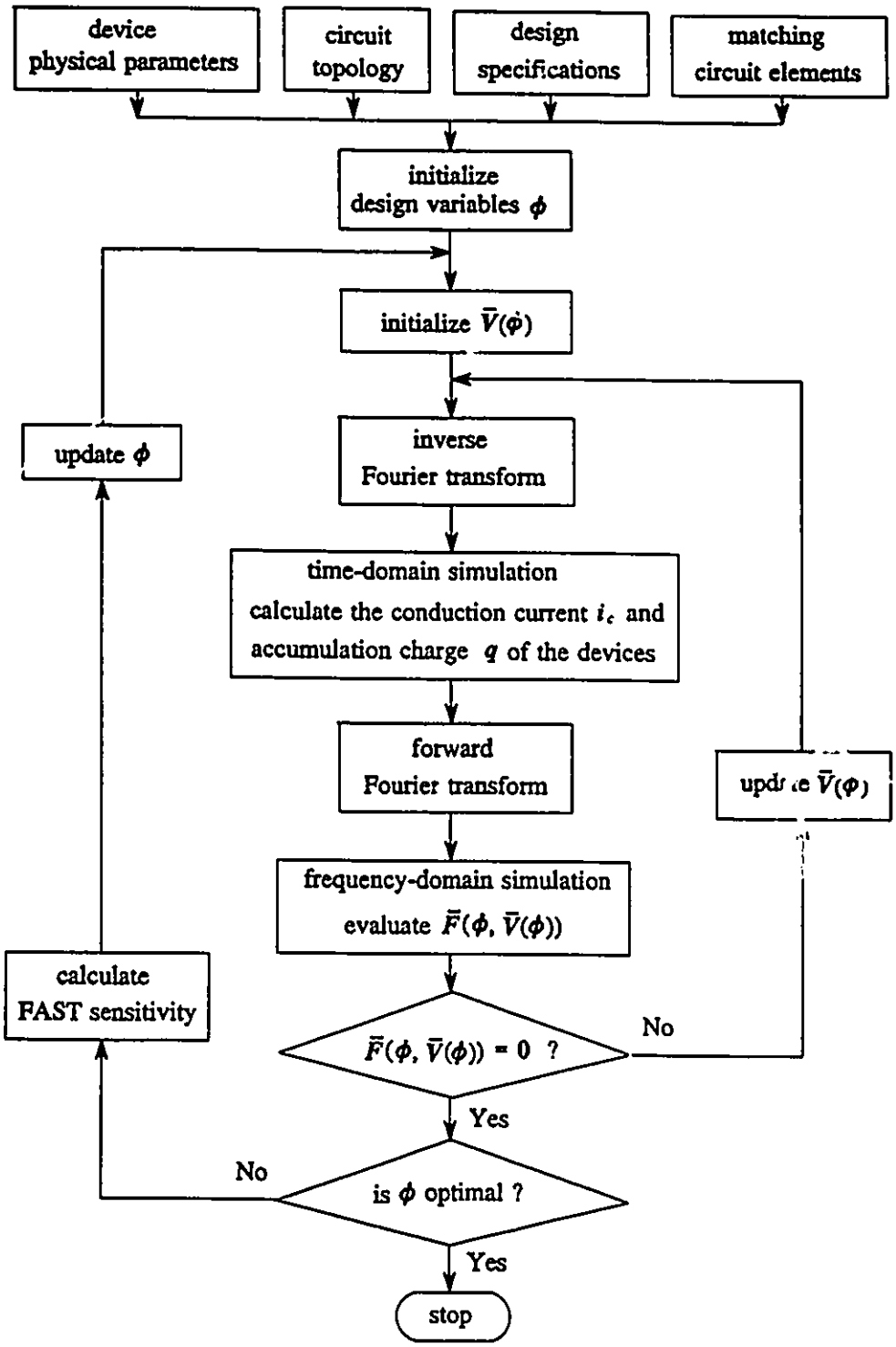

Fig. 4.1 Flowchart for design optimization of a nonlinear FET circuit using HB.

4.5 CIRCUIT DESIGN EXAMPLES

A small-signal circuit design and a large-signal circuit design are considered as examples to show design optimization with PBMs. The powerful and efficient CAD system OSA90/hope [139] is used to carry out the optimization for the design of these two circuits.

4.5.1 A Small-Signal Amplifier Design

A broadband MMIC small-signal feedback amplifier (Rigby, Suffolk and Pengelly (1983) [103]) is considered. The circuit diagram for this amplifier is shown in Fig. 4.2. A MESFET of dimensions 900μm×0.5μm is selected for this amplifier. High impedance transmission lines are used to realize "inductors". The feedback loop comprises a transmission line, a resistor and a capacitor in series. The gate bias is applied through a high value resistor. The off-chip drain bias is applied through a 15nH inductor which consists of a 5nH inductor on the chip and a 10nH inductor off-chip. The design specifications are at frequency range 1GHz to 6GHz:

gain = 6dB ± 0.5dB,

input VSWR < 3,

output VSWR < 2.

The circuit topology for the intrinsic FET and its associated extrinsic elements in Fig. 2.8 are selected for the FET. The FET parameters are listed in Table 4.1. As in conventional circuit design, we optimize only the elements in the matching circuits while the FET parameters are kept fixed. The feedback resistor R_2, capacitors C_1, C_3, C_5, and transmission lines TL_1, TL_2, TL_3, TL_4, TL_5 are selected as design variables.

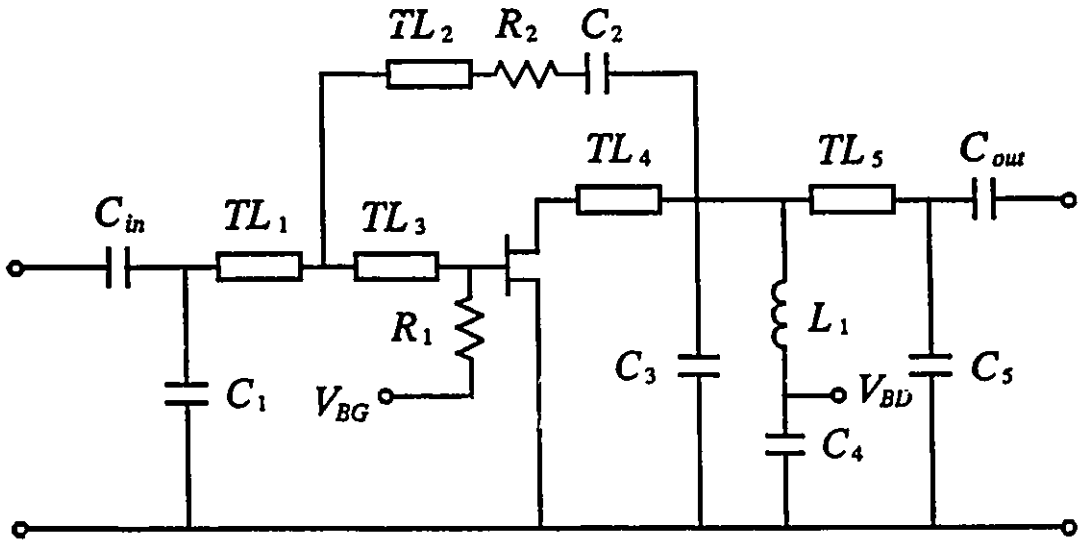

Fig. 4.2 Circuit diagram for the MMIC small-signal feedback amplifier.

TABLE 4.1

MESFET PARAMETER VALUES
USED FOR THE FEEDBACK AMPLIFIER DESIGN

Parameter	Values	Parameter	Values
$L(\mu m)$	0.5	$R_g(\Omega)$	1.5
$W(\mu m)$	900	$R_s(\Omega)$	0.9
$N_d(1/m^3)$	1.5×10^{23}	$R_d(\Omega)$	0.5
$a(\mu m)$	0.2	L_g(nH)	0.06
V_{bi}(V)	0.6	L_s(nH)	0.35
$D_0(m^2/s)$	1.0×10^{-3}	L_d(nH)	0.73
E_c(V/m)	3.5×10^5	C_{ds}(pF)	0.001
v_s(m/s)	1.0×10^6	C_{gc}(pF)	0.003
ε_r	12.9	C_{dc}(pF)	0.24
		C_x(pF)	10
		$G_{ds}(1/\Omega)$	2.8×10-5

The other elements are fixed as: $R_1 = 2500\Omega$, $C_2 = 40$pF, $C_4 = 150$pF, $L_1 = 15$nH. The impedance for all transmission lines is 85Ω and fixed.

The built-in minimax optimizer of OSA90/hope is used to perform design optimization. It takes 21 iterations (about 3 minutes CPU time) for the optimization tc converge on a Sun SPARCstation 1. All the specifications are satisfied. The values of the design variables before and after optimization are listed in Table 4.2. Fig. 4.3 shows the gain versus frequency before and after optimization. The input VSWR and output VSWR before and after optimization are shown in Fig. 4.4 and Fig. 4.5, respectively.

4.5.2 A Large-Signal Frequency Doubler Design

A frequency doubler used by Bandler, Zhang, Song and Biernacki (1990) [24] for yield optimization is adopted here to demonstrate large-signal circuit design. The schematic of the frequency doubler is shown in Fig. 4.6. It consists of a common-source FET with a lumped input matching network and a microstrip output matching and filter section. Responses of interest are the conversion gain and spectral purity, which are defined respectively by

$$\text{conversion gain} = 10\times \log\left[\frac{P_{out}(2)}{P_{in}(1)}\right]$$

and

$$\text{spectral purity} = 10\times \log\left[\frac{P_{out}(2)}{\sum\limits_{\substack{i=1\\ i\neq 2}}^{H} P_{out}(i)}\right]$$

where $P_{out}(i)$ is the power of the ith harmonic at the output port, $P_{in}(i)$ is the power

The other elements are fixed as: $R_1 = 2500\Omega$, $C_2 = 40$pF, $C_4 = 150$pF, $L_1 = 15$nH. The impedance for all transmission lines is 85Ω and fixed.

The built-in minimax optimizer of OSA90/hope is used to perform design optimization. It takes 21 iterations (about 3 minutes CPU time) for the optimization to converge on a Sun SPARCstation 1. All the specifications are satisfied. The values of the design variables before and after optimization are listed in Table 4.2. Fig. 4.3 shows the gain versus frequency before and after optimization. The input VSWR and output VSWR before and after optimization are shown in Fig. 4.4 and Fig. 4.5, respectively.

4.5.2 A Large-Signal Frequency Doubler Design

A frequency doubler used by Bandler, Zhang, Song and Biernacki (1990) [24] for yield optimization is adopted here to demonstrate large-signal circuit design. The schematic of the frequency doubler is shown in Fig. 4.6. It consists of a common-source FET with a lumped input matching network and a microstrip output matching and filter section. Responses of interest are the conversion gain and spectral purity, which are defined respectively by

$$\text{conversion gain} = 10\times \log\left(\frac{P_{out}(2)}{P_{in}(1)}\right)$$

and

$$\text{spectral purity} = 10\times \log\left(\frac{P_{out}(2)}{\sum_{\substack{i=1\\ i\neq 2}}^{H} P_{out}(i)}\right)$$

where $P_{out}(i)$ is the power of the ith harmonic at the output port, $P_{in}(i)$ is the power

TABLE 4.2

DESIGN VARIABLE VALUES BEFORE AND AFTER OPTIMIZATION FOR THE FEEDBACK AMPLIFIER

Parameter	Before Optimization	After Optimization
$R_2(\Omega)$	254	193.1
C_1(pF)	0.28	0.095
C_3(pF)	0.22	0.137
C_5(pF)	0.11	0.083
TL_1(m)	0.96×10^{-3}	0.867×10^{-3}
TL_2(m)	1.6×10^{-3}	0.816×10^{-3}
TL_3(m)	0.42×10^{-3}	0.396×10^{-3}
TL_4(m)	1.8×10^{-3}	0.392×10^{-3}
TL_5(m)	0.49×10^{-3}	0.570×10^{-3}

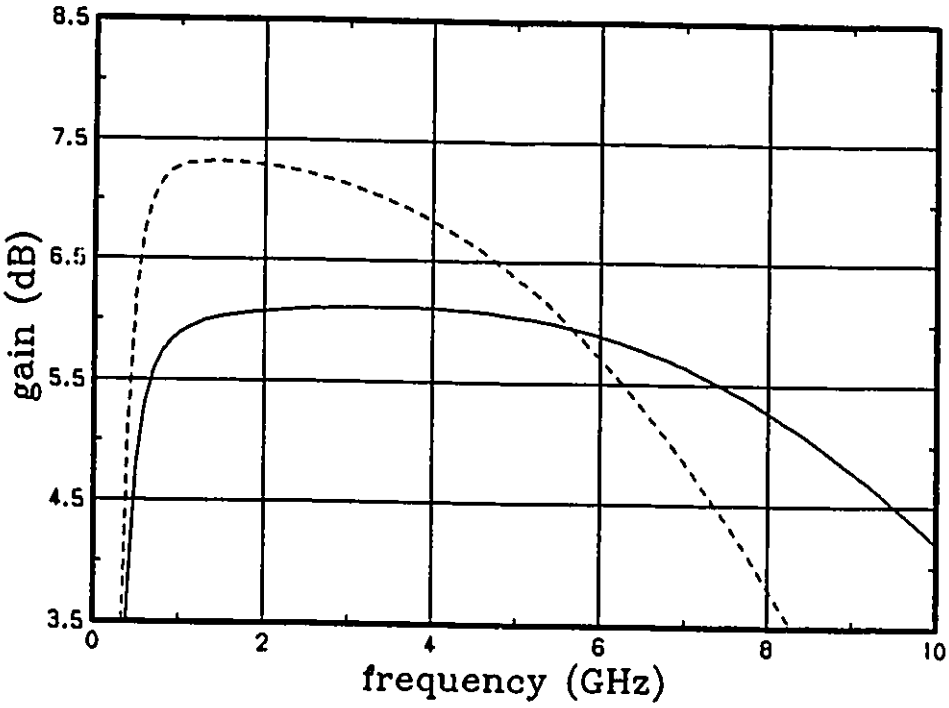

Fig. 4.3 Gain versus frequency of the MMIC small-signal feedback amplifier before (---) and after (——) optimization.

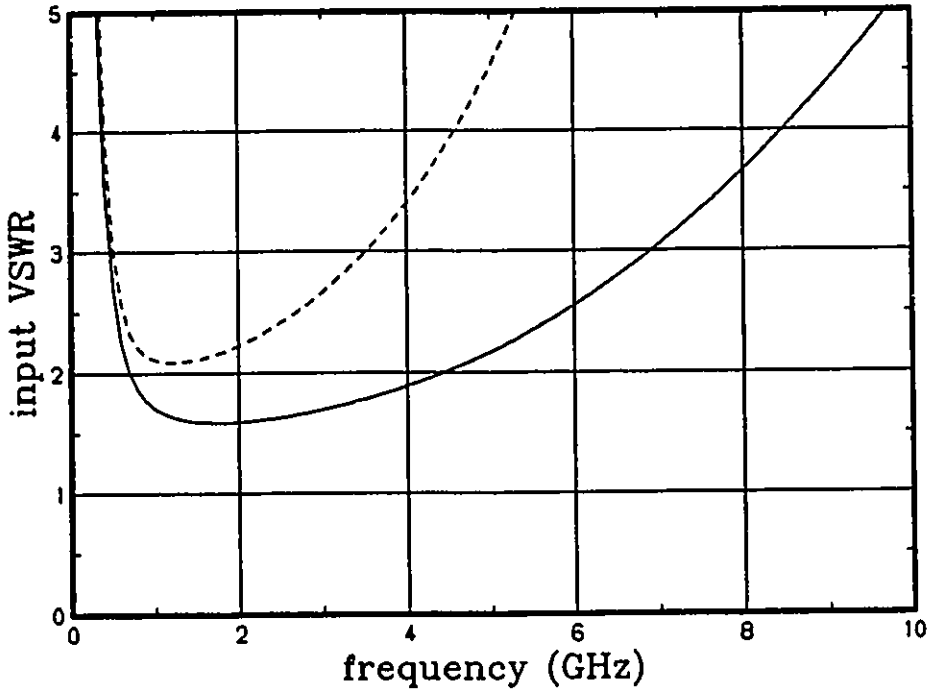

Fig. 4.4 Input VSWR versus frequency of the MMIC small-signal feedback amplifier before (---) and after (——) optimization.

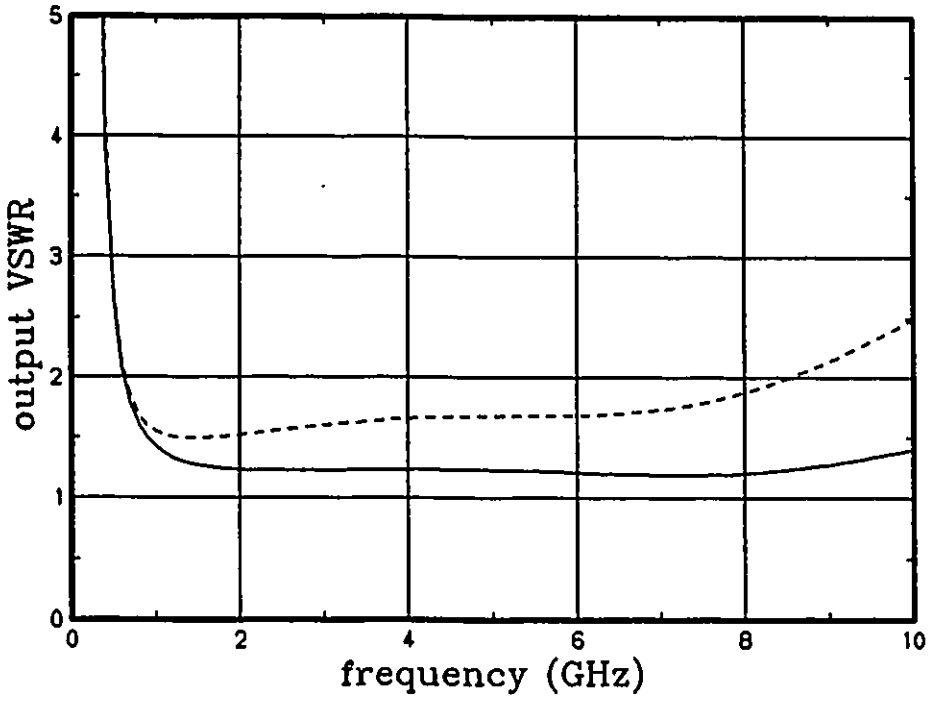

Fig. 4.5 Output VSWR versus frequency of the MMIC small-signal feedback amplifier before (---) and after (——) optimization.

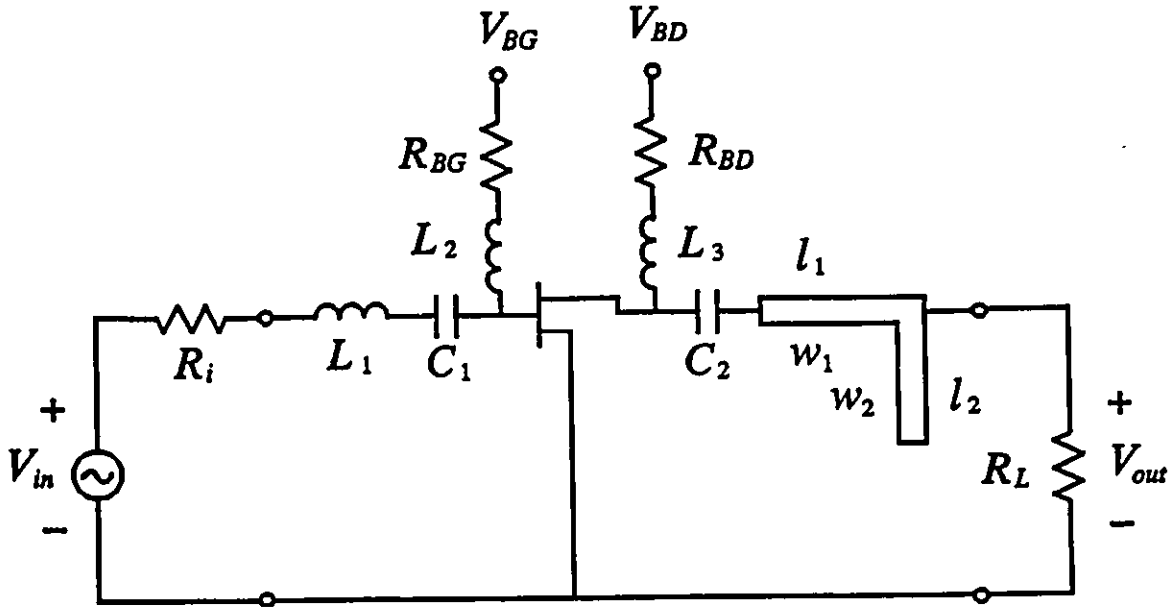

Fig. 4.6 Circuit diagram of the FET microwave frequency doubler.

of the ith harmonic at the input port, and $i = 1$ corresponds to the fundamental frequency.

The fundamental frequency is 5GHz. The design specifications are

conversion gain > 2.5dB

spectral purity > 19dB

at $P_{in}(1) = 2$dBm.

According to [24], the extrinsic circuits for the MESFET shown in Fig. 4.7 is selected. The parameters for the MESFET are listed in Table 4.3. In this circuit design, both the matching circuits and device are optimized. The design variables include the input inductance L_1, microstrip lengths l_1 and l_2, FET gate length L, gate width W, channel thickness a and doping density N_d. The other elements in the matching circuits are fixed as $C_1 = 20$pF, $C_2 = 20$pF, $L_2 = 15$nH, $L_3 = 15$nH, $R_{BG} = 10\Omega$, $R_{BD} = 10\Omega$, $w_1 = 0.1\times10^{-3}$m, $w_2 = 0.635\times10^{-3}$m. Both the source resistance R_i and load resistance R_L are 50Ω.

The minimax optimizer of OSA90/hope is also used for this circuit design. The design optimization takes 21 iterations (approximately 3.5 CPU minutes) on a Sun SPARCstation 1. All the design specifications are satisfied. The values of the design variables before and after optimization are listed in Table 4.4. The conversion gain and spectral purity versus available input power before and after optimization are shown in Fig. 4.8 and Fig. 4.9, respectively. The input voltage waveform and output voltage waveforms before and after optimization are shown in Fig. 4.10. We can easily see that a very good result is obtained after optimization.

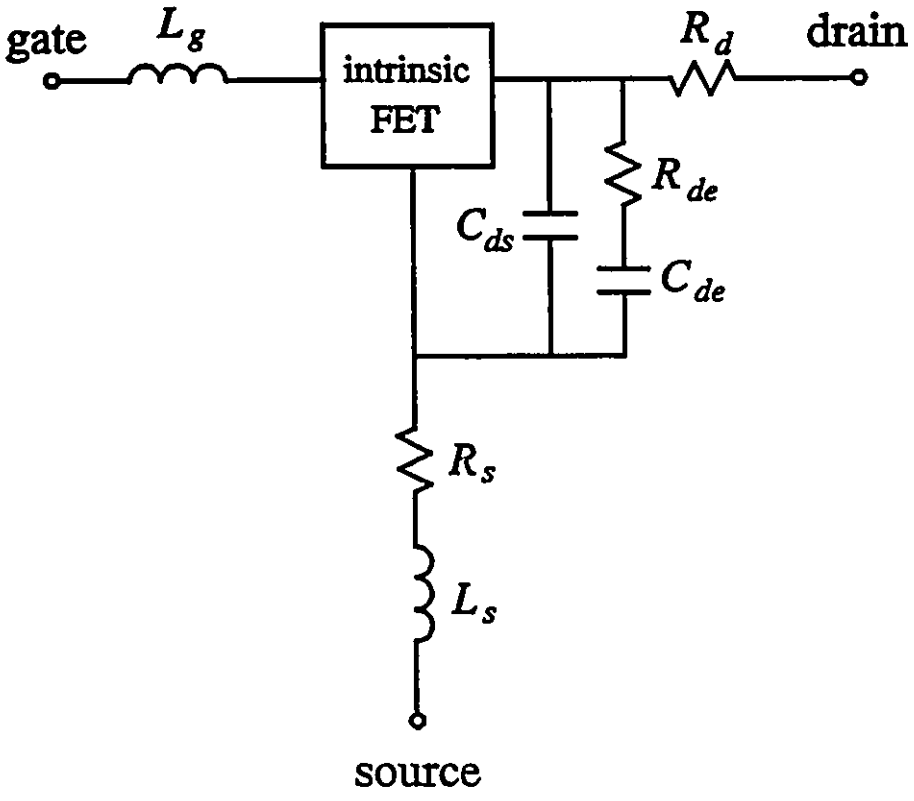

Fig. 4.7 Intrinsic FET and its associated extrinsic elements used for the frequency doubler design.

TABLE 4.3

MESFET PARAMETER VALUES
USED FOR THE FREQUENCY DOUBLER DESIGN

Parameter	Values	Parameter	Values
$L(\mu m)$	0.55	$R_s(\Omega)$	1.1
$W(\mu m)$	400	$R_d(\Omega)$	3.1
$N_d(1/m^3)$	1.75×10^{23}	L_g(nH)	0.17
$a(\mu m)$	0.3	L_s(nH)	0.07
V_{bi}(V)	0.6	$R_{dc}(\Omega)$	455
$D_0(m^2/s)$	1.0×10^{-3}	C_{ds}(pF)	0.12
E_c(V/m)	4.4×10^{5}	C_{dc}(pF)	1.14
$\mu_0(m^2/Vs)$	0.4		
ϵ_r	12.9		

TABLE 4.4

DESIGN VARIABLE VALUES BEFORE AND AFTER OPTIMIZATION FOR THE FREQUENCY DOUBLER

Parameter	Before Optimization	After Optimization
$L(\mu m)$	0.55	0.549
$W(\mu m)$	400	415.3
$a(\mu m)$	0.3	0.288
$N_d(1/m^3)$	1.75×10^{23}	1.78×10^{23}
$L_1(nH)$	5.0	5.164
$l_1(m)$	1.0×10^{-3}	1.01×10^{-3}
$l_2(m)$	5.3×10^{-3}	5.986×10^{-3}

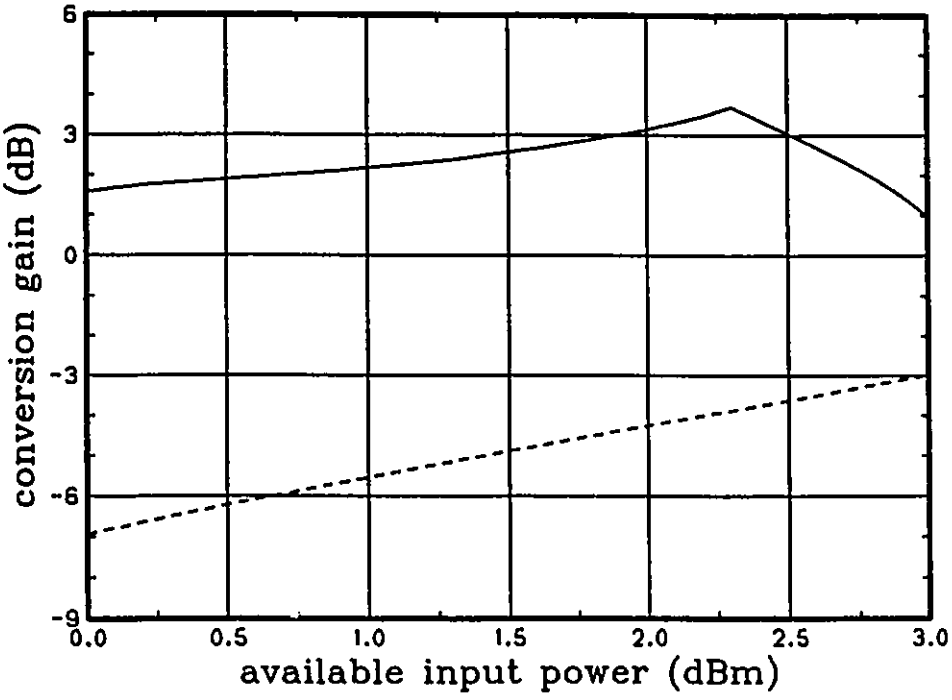

Fig. 4.8 Conversion gain versus input power of the frequency doubler before (---) and after (——) optimization.

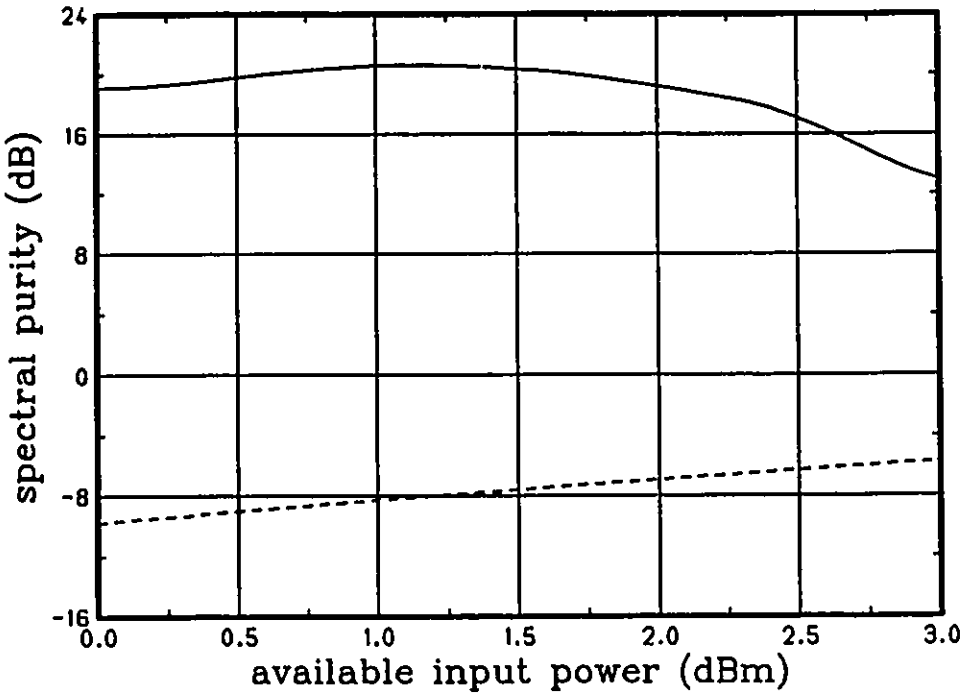

Fig. 4.9 Spectral purity versus input power of the frequency doubler before (---) and after (——) optimization.

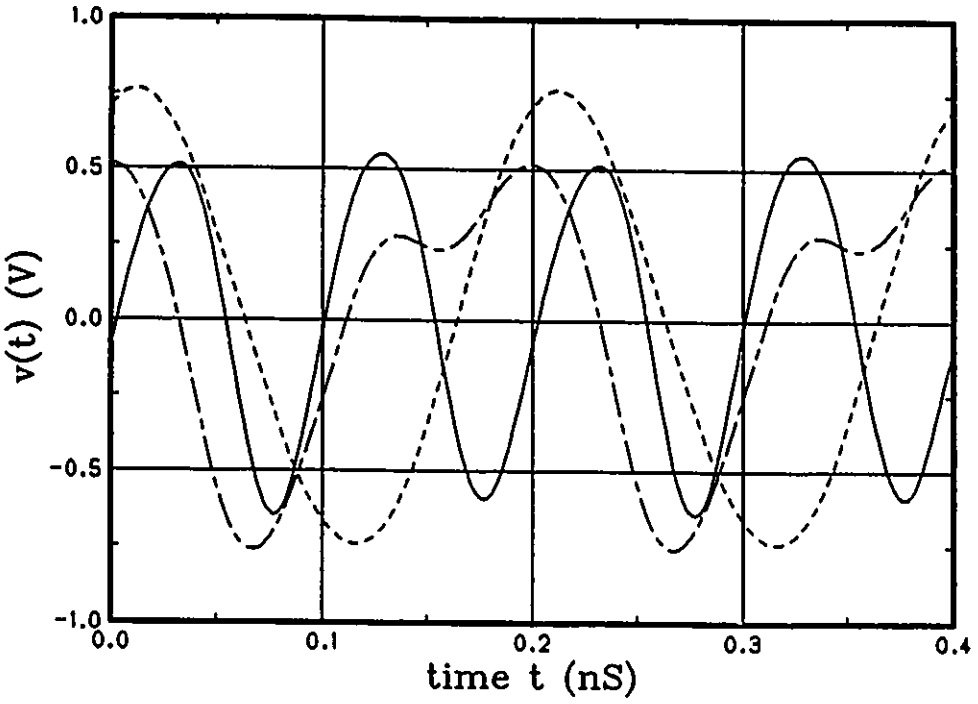

Fig. 4.10 Input voltage waveform (---) and output voltage waveform of the frequency doubler before (---) and after (——) optimization.

4.6 CONCLUSIONS

In this chapter, we addressed gradient-based optimization methods for circuit design. A number of sensitivity analysis techniques have been discussed. FAST has been emphasized for its computational efficiency and easy implementation. We integrated FAST with PBMs using the HB method. This integration permits efficient physics-based design optimization. The algorithm of optimization for MESFET circuits using the HB method has been illustrated. Two circuit design examples have been given to demonstrate the efficiency of gradient-based optimization.

Chapter 5

STATISTICAL MODELING

5.1 INTRODUCTION

Statistical modeling has been seriously studied for metal-oxide semiconductor (MOS) and complementary metal-oxide semiconductor (CMOS) circuits for more than a decade. A large number of research papers has been published in this area. Some of these results are reviewed here.

Dutton, Divekar, Gonzalez, Hansen and Antoniadis (1977) [52] and Divekar, Dutton and McCalla (1977) [51] studied the correlation of fabrication process and electrical device parameter variations and experimented on bipolar junction transistors. In their studies, the method of factor analysis was used to analyze the correlations between the device parameters. The process-dependent parameters which control the device parameters and the key factors which control the parameter correlations were identified.

Styblinski (1977) [126] studied four physical models of resistor correlations for monolithic integrated circuits based on the physical phenomena using factor analysis methods. He concluded that a simple model with two common factors was sufficiently accurate for practical purposes.

The fundamental concepts in statistical modeling for integrated circuits (IC) were described by Rankin (1982) [99]. He surveyed two alternative approaches to the

characterization of ICs for statistical design. The first was based on a direct description of the distributions of the electrical parameters of standard ECMs (e.g., SPICE model) which were extracted from the measured data. The second approach was based on PBMs. Modeling equations were used to relate the ECMs to the device physical parameters. Then the device responses were predicted by those ECMs.

A compact statistical model for MOSFETs was proposed by Liu and Singhal (1985) [83] to simulate the statistical variations in the device characteristics resulting from parameter variations in the process. Statistical analysis was applied to large samples of measured data to identify the critical process parameters. Multi-parameter linear regression and single parameter nonlinear regression were used to determine the model parameters.

Cox, Yang, Mahant-Shetti and Chatterjee (1985) [41] developed an automated system to obtain the process statistical variations and extract SPICE model parameters for a large number of MOS devices. Statistical modeling using only four statistical variables, namely gate length, width, oxide thickness and flat-band voltage was claimed suitable for efficient parametric yield estimation of MOS VLSI circuits.

The methodology of parameter extraction was used by Herr and Barnes (1986) [64] for statistical circuit simulation modeling of CMOS and by Spanos and Director (1986) [121] for statistical IC process characterization. In [64], the parameters of the model were extracted by parameter extraction and then the distribution of these parameters were generated. In [121] a hierarchial approach to relate the process disturbance to circuit responses was used. The statistical moments associated with a set of independently varying parameters were extracted by parameter extraction.

Microwave device statistical modeling has a comparatively short history to that of MOS and CMOS in ICs. Purviance, Criss and Monteith (1988) [96] used a small-signal equivalent circuit model to study the sensitivity of the design center and the yield estimate of a FET amplifier as a function of the model statistics. Two different FET statistical models, uniform uncorrelated parameter distributions and marginal parameter distributions with correlation, were studied. They showed that the design center was insensitive but the yield estimates were sensitive to the statistical models. Purviance, Petzold and Potratz (1989) [97] presented a linear statistical FET model using principal component analysis at the S-parameter level. Uncorrelated principal components which were linear combinations of the original variables were used as the statistical parameters to simplify the model. However, these principal components do not have any physical meaning and direct relations to physical process parameters.

Bandler, Biernacki, Chen, Loman, Renault and Zhang (1989) [20] combined discrete and normal distributions to characterize the distributions substantially different from normal. This approach preserves the statistical properties derived from the sample. The relation between model statistical confidence and sample size was discussed. Their investigation showed that a reasonable sample size is between 20 and 50 under the assumption of a normal distribution. Bandler, Biernacki, Chen, Song, Ye and Zhang (1991) [25] presented statistical modeling of GaAs MESFETs based on the statistical extraction of MESFET ECM parameters and physical parameters from wafer measurements.

In this chapter, we discuss statistical modeling of FETs at different levels with emphasis on physics-based statistical modeling. A sample of device models is

obtained by parameter extraction for individual devices from measurements and then postprocessed to obtain the parameter statistics which form the statistical model. Monte Carlo simulation is used for model verification. Statistical modeling with ECMs and PBMs are presented.

5.2 STATISTICAL MODELING AT DIFFERENT LEVELS

A statistical model can be considered at the equivalent circuit model level (statistical ECMs), the physical-based model level (statistical PBMs) and the device response level (statistical RLMs), as shown in Fig. 5.1.

ECM statistical modeling attempts to characterize the distribution of the equivalent circuit parameters such as inductors and capacitors [20,96]. The main advantage of this approach is that many ECMs are available in microwave CAD software and ECM simulation is usually efficient. However, it is difficult or even impossible to relate the statistical distributions of ECM parameters to those of the device physical parameters. Statistical variations in a single physical parameter may affect many ECM parameters, and at the same time each ECM parameter may be affected by many physical parameters. Consequently, the equivalent circuit model parameters are correlated and such correlations are difficult to estimate. Furthermore, this nonlinear mapping may result in complicated and non-Gaussian distributions.

Statistical PBMs characterize the distributions of device physical parameters [25]. With PBMs it is easier to identify the parameters that are subject to significant statistical variations and the parameters which are correlated (e.g., geometrical dimensions). The statistics of some physical parameters may even be directly available

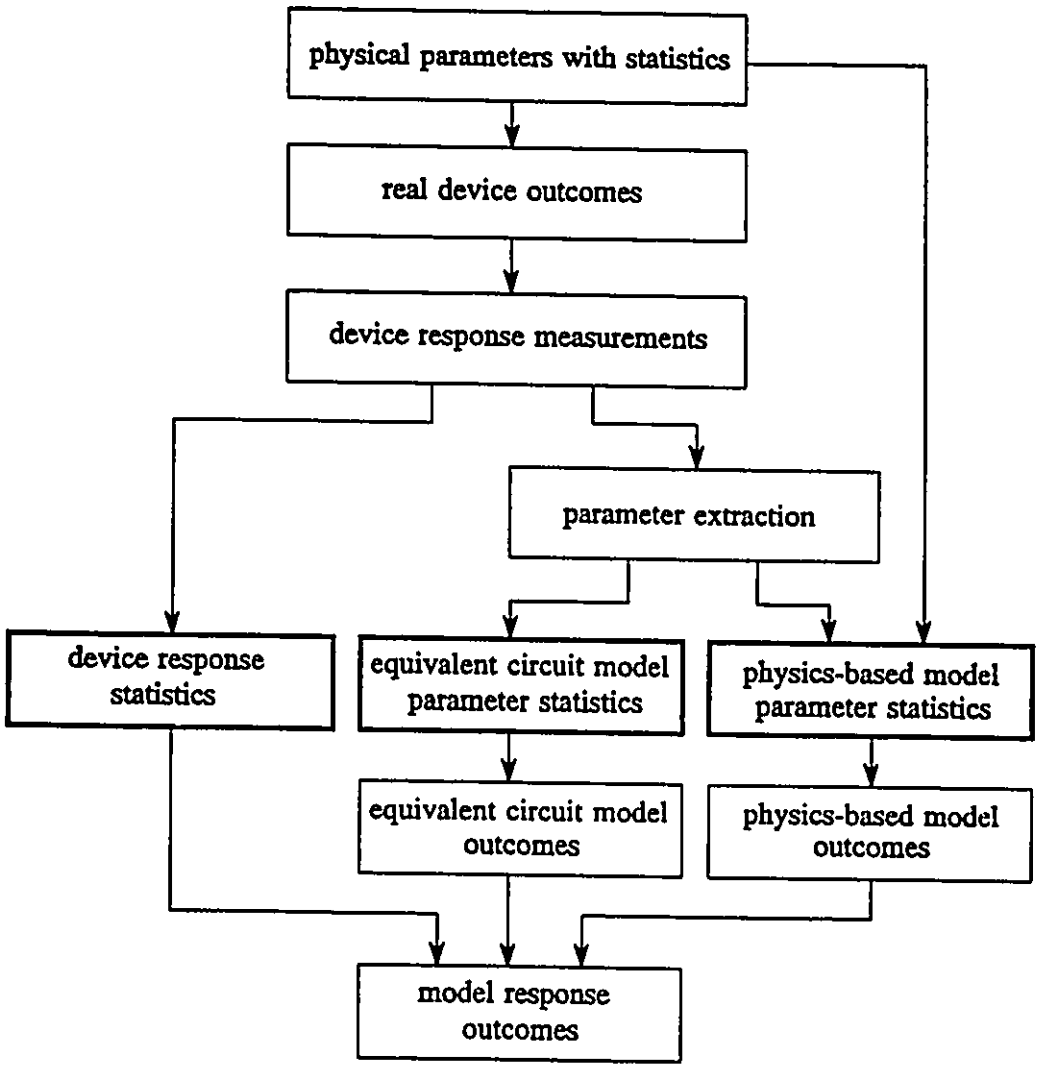

Fig. 5.1 Different levels of statistical modeling.

from measurements. At this level, the typical assumption of a normal distribution is often justified. Unlike ECMs, by attempting to characterize statistical behaviour of the parameters that are actually subject to random variations in the real world, PBM statistical modeling is closer to reality and we believe it is more accurate and reliable. An obvious disadvantage of PBMs is that simulation may be more time consuming.

Statistical RLMs directly use the distributions of the device responses obtained from measurements. The device responses can be small-signal or large-signal, for instance, S parameters. The properties of a FET statistical data base has been investigated by Purviance, Meehan and Collins (1990) [98]. A statistical model called "truth model" was proposed. The truth model is an empirical discrete density function obtained from measured samples. It has been used for design centering and yield prediction (Meehan, Wandinger and Fisher (1991) [87]).

5.3 STATISTICAL PARAMETER EXTRACTION AND ESTIMATION

5.3.1 Statistical Parameter Extraction

Our approach to statistical modeling is based on parameter extraction and statistical estimation through postprocessing. It requires measurements taken on a large sample of devices, which may include DC, small-signal and large-signal data. For each device, the model parameters are extracted from the corresponding measurements, resulting in a sample of models. Efficient, consistent and reliable parameter extraction is essential for this approach.

Suppose we have K sets of measurement data, each containing m measured

responses

$$S^i = [S_1^i \; S_2^i \; \ldots \; S_m^i]^T \tag{5.1}$$

corresponding to the ith device, $i = 1, 2, \ldots, K$, where K is the total number of devices measured. Let

$$\phi^i = [\phi_1^i \; \phi_2^i \; \ldots \; \phi_n^i]^T \tag{5.2}$$

denote the model parameters of the ith device and

$$R(\phi^i) = [R_1(\phi^i) \; R_2(\phi^i) \; \ldots \; R_m(\phi^i)]^T \tag{5.3}$$

be the model responses corresponding to the measurements S^i. The parameter extraction problem can be formulated as (Bandler, Chen and Daijavad (1986) [13])

$$\min_{\phi^i} \sum_{j=1}^{m} w_j^i \, | R_j(\phi^i) - S_j^i |^p \qquad 1 \le p \tag{5.4}$$

where w_j^i is a weighting factor and $p = 1$ or $p = 2$ leads to ℓ_1 or ℓ_2 (least squares) optimization, respectively. Optimization is performed for each device measured, i.e., for $i = 1, 2, \ldots, K$.

5.3.2 Statistical Parameter Estimation

The statistical models are represented by parameter distributions and correlations. The common distributions used for statistical modeling are uniform and normal distributions which can be respectively described, for a random variable ϕ_i, as

$$p(\phi_i) = \begin{cases} \dfrac{1}{c - b} & b \le \phi_i \le c \\ 0 & \text{otherwise} \end{cases} \tag{5.5}$$

and

$$p(\phi_i) = \frac{1}{\sigma_{\phi_i}\sqrt{2\pi}} \exp\left[-\frac{(\phi_i - \nu_{\phi_i})^2}{2\sigma_{\phi_i}^2}\right] \tag{5.6}$$

where $p(\phi_i)$ is the probability density function, ν_{ϕ_i} is the mean and $\sigma_{\phi_i}^2$ is the variance.

In our study of statistical modeling, we use uniform distribution to describe the statistical characteristics of linear elements such as resistors, capacitors and inductors at the equivalent circuit level and normal distribution to characterize the statistical properties of physical parameters such as gate length, gate width and doping density of a FET.

If a multidimensional normal distribution is assumed for the model parameters, it is described by the mean values, standard deviations and pairwise correlation coefficients. They can be estimated by postprocessing the sample resulting from parameter extraction. The mean values of parameters ϕ_i, ν_{ϕ_i}, is estimated by

$$\nu_{\phi_i} = \frac{\sum_{l=1}^{K} \phi_i^l}{K} \tag{5.7}$$

The standard deviation σ_{ϕ_i} is calculated using

$$\sigma_{\phi_i} = \sqrt{\frac{\sum_{l=1}^{K} (\phi_i^l - \nu_{\phi_i})^2}{K - 1}} \tag{5.8}$$

The correlation coefficient between parameter ϕ_i and ϕ_j, $r_{\phi_i\phi_j}$, is evaluated by

$$r_{\phi_i\phi_j} = \frac{\sum_{l=1}^{K} (\phi_i^l - \nu_{\phi_i})(\phi_j^l - \nu_{\phi_j})}{\sqrt{\sum_{l=1}^{K} (\phi_i^l - \nu_{\phi_i})^2 \sum_{l=1}^{K} (\phi_j^l - \nu_{\phi_j})^2}} \tag{5.9}$$

In cases where the sample distribution appears substantially different from

normal, we utilize the marginal discrete density function (DDF) approach (Bandler, Biernacki, Chen, Loman, Renault and Zhang (1989) [20]). A discretized joint probability density function has also been proposed to deal with such cases (e.g, Dutton, Divekar, Gonzalez, Hasen and Antoniadis (1977) [52], Abdel-Malek and Bandler (1980) [1,2]).

5.3.3 Monte Carlo Simulation for Model Verification

For statistical modeling to be useful in statistical analysis and design or yield analysis and optimization, we must be able to predict the statistical behaviour of the actual devices through Monte Carlo simulation, i.e., the model responses and the actual device responses must be statistically consistent.

To this end, Monte Carlo simulation is used for model verification by comparing the statistical distribution of the simulated device responses to that of the measured data.

Monte Carlo simulation is a practical means of studying the statistical behaviour of devices and circuits. In the Monte Carlo simulation, a random number generator is applied to generate random parameter sets from the parameter statistical distributions provided by the device statistical models. These parameter sets are used as the device parameters for circuit simulation to obtain the corresponding device or circuit responses. The resulting responses are postprocessed to obtain their statistical distributions which are then compared to the corresponding distributions of the measured data to verify the device statistical model. The entire procedure of this model verification with N outcomes used in the Monte Carlo simulation can be

illustrated by Fig. 5.2.

5.4 STATISTICAL MODELING WITH ECMs [25]

In order to have a comparison of statistical modeling between ECMs and PBMs, statistical modeling using a typical ECM model proposed by Materka and Kacprzak (1985) [86] is presented. This work was originally carried out by Bandler, Biernacki, Chen, Song, Ye and Zhang (1991) [25].

The materka and Kacprzak model is a nonlinear ECM FET model. The circuit diagram of the model is shown in Fig. 5.3. The intrinsic elements are defined as

$$i_{ds} = F[v_g(t - \tau),\ v_d(t)]\left[1 + S_s\frac{v_d(t)}{I_{DSS}}\right] \tag{5.10}$$

$$F(v_g,\ v_d) = I_{DSS}\left[1 - \frac{v_g}{V_{P0} + \gamma v_d}\right]^{(E+K_E v_g)}\tanh\left[\frac{S_1 v_d}{I_{DSS}(1 - K_G v_g)}\right] \tag{5.11}$$

$$i_{gs} = I_{G0}[\exp(\alpha_G v_g) - 1] \tag{5.12}$$

$$i_{dg} = I_{B0}\exp[\alpha_B(v_{dg} - V_{BC})] \tag{5.13}$$

$$R_{in} = \begin{cases} R_{10}(1 - K_R v_g) \\ 0 \qquad\qquad \text{if } K_R v_g \geq 1 \end{cases} \tag{5.14}$$

$$C_{gs} = \begin{cases} C_{10}(1 - K_1 v_g)^{-1/2} + C_{1S} \\ C_{10}\sqrt{5} + C_{1S} \qquad \text{if } K_1 v_g \geq 0.8 \end{cases} \tag{5.15}$$

$$C_{dg} = \begin{cases} C_{F0}(1 + K_F v_{dg})^{-1/2} \\ C_{F0}\sqrt{5} \qquad \text{if } -K_F v_{dg} \geq 0.8 \end{cases} \tag{5.16}$$

The model parameters corresponding to these intrinsic elements include I_{DSS}, V_{P0}, γ, E, K_E, S_1, K_G, τ, S_S, I_{G0}, α_G, I_{B0}, α_B, V_{BC}, R_{10}, K_R, C_{10}, K_1, C_{1S}, C_{F0} and K_F.

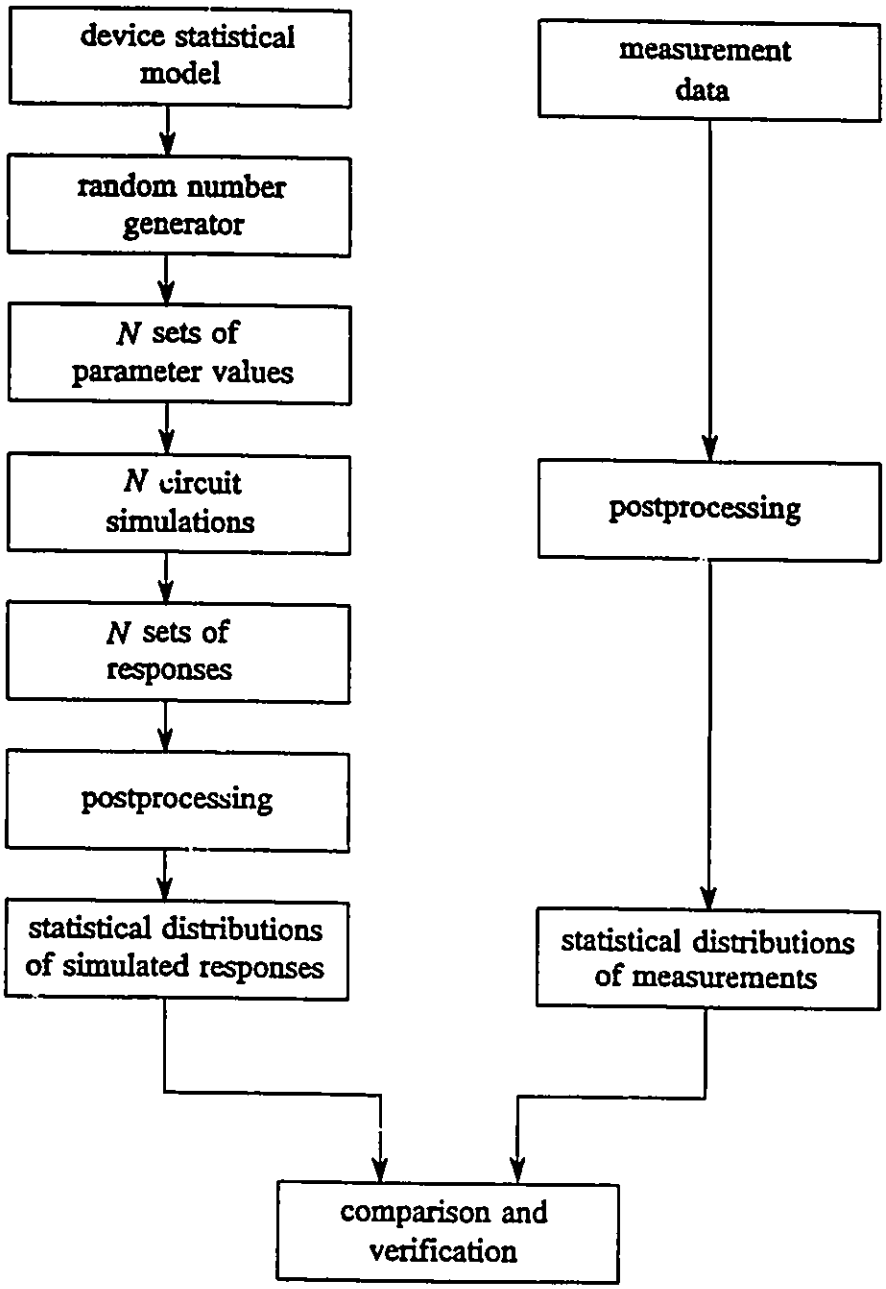

Fig. 5.2 Statistical model verification using Monte Carlo simulation.

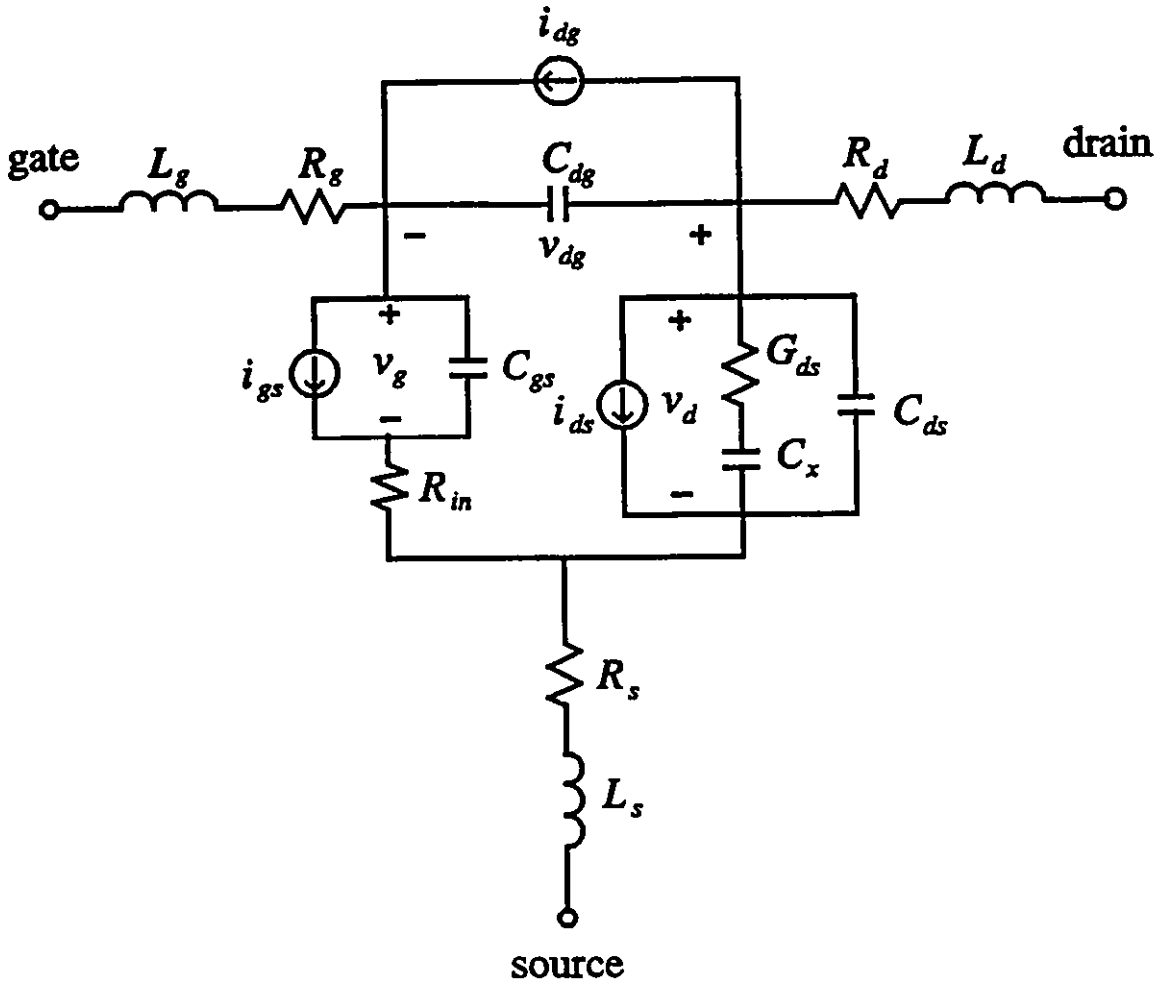

Fig. 5.3 Circuit diagram for the Materka and Kacprzak FET model.

The linear extrinsic parameters are R_g, R_d, R_s, L_g, L_d, L_s, G_{ds}, C_{ds} and C_x.

The measurements used for statistical modeling include 69 individual devices (data sets) selected from two wafers provided by Plessey Research Caswell [140]. Each device represents a four finger 0.5μm GaAs MESFET with equal finger width of 75μm. Each data set contains small-signal S parameters measured under three different bias conditions and at frequencies from 1GHz to 21GHz with a 0.4GHz step. DC drain bias current is also included in the measurements.

HarPE [138] was used to extract the statistical device models. The measurements used for parameter extraction include DC bias currents at three bias points and S parameters for those bias points at frequencies from 1GHz to 21GHz with a 2GHz step. The linear parameter C_x is fixed at 2pF for the model.

Model parameters for each individual device were extracted by matching simultaneously the DC and small-signal S-parameter responses to the corresponding measurements. The resulting 69 models were postprocessed to obtain the mean values of the parameters. In order to improve the consistency of the parameter extraction process, individual device models were extracted again using those mean values as new initial parameter values. The new resulting sample of models was then postprocessed to obtain the parameter statistics, including the mean values, standard deviations, DDFs, as well as the correlations among the parameters.

The parameter statistics (mean values and standard deviations) of the Materka and Kacprzak model are listed in Table 5.1. Fig. 5.4 shows the match between the S parameters computed from a nominal simulation (i.e., the parameters assume their mean value) and the mean values of the measured S parameters at the bias point

TABLE 5.1

STATISTICAL PARAMETERS
FOR THE MATERKA AND KACPRZAK MODEL [25]

Parameter	Mean Value	Standard Deviation (%)
I_{DSS}(mA)	47.56	11.2
V_{P0}(V)	-1.488	11.9
γ	-0.1065	7.51
E	1.661	2.40
K_E(1/V)	4.676×10^{-3}	5.70
τ(pS)	2.187	3.45
S_S(1/Ω)	1.565×10^{-3}	9.75
R_{10}(Ω)	7.588	7.40
K_R(1/V)	0.3375	16.9
C_{10}(pF)	0.3698	3.55
C_{1S}(pF)	1.230×10^{-3}	28.5
K_I(1/V)	1.238	8.73
C_{F0}(pF)	1.625×10^{-2}	4.57
K_F(1/V)	-0.1180	3.17
L_g(nH)	3.422×10^{-2}	17.8
R_g(Ω)	9.508×10^{-3}	7.73
R_d(Ω)	2.445	32.8
L_d(nH)	5.035×10^{-2}	28.6
R_s(Ω)	0.7753	40.2
L_s(nH)	1.427×10^{-2}	21.9
G_{ds}(1/Ω)	1.838×10^{-3}	5.02
C_{ds}(pF)	5.838×10^{-2}	3.35

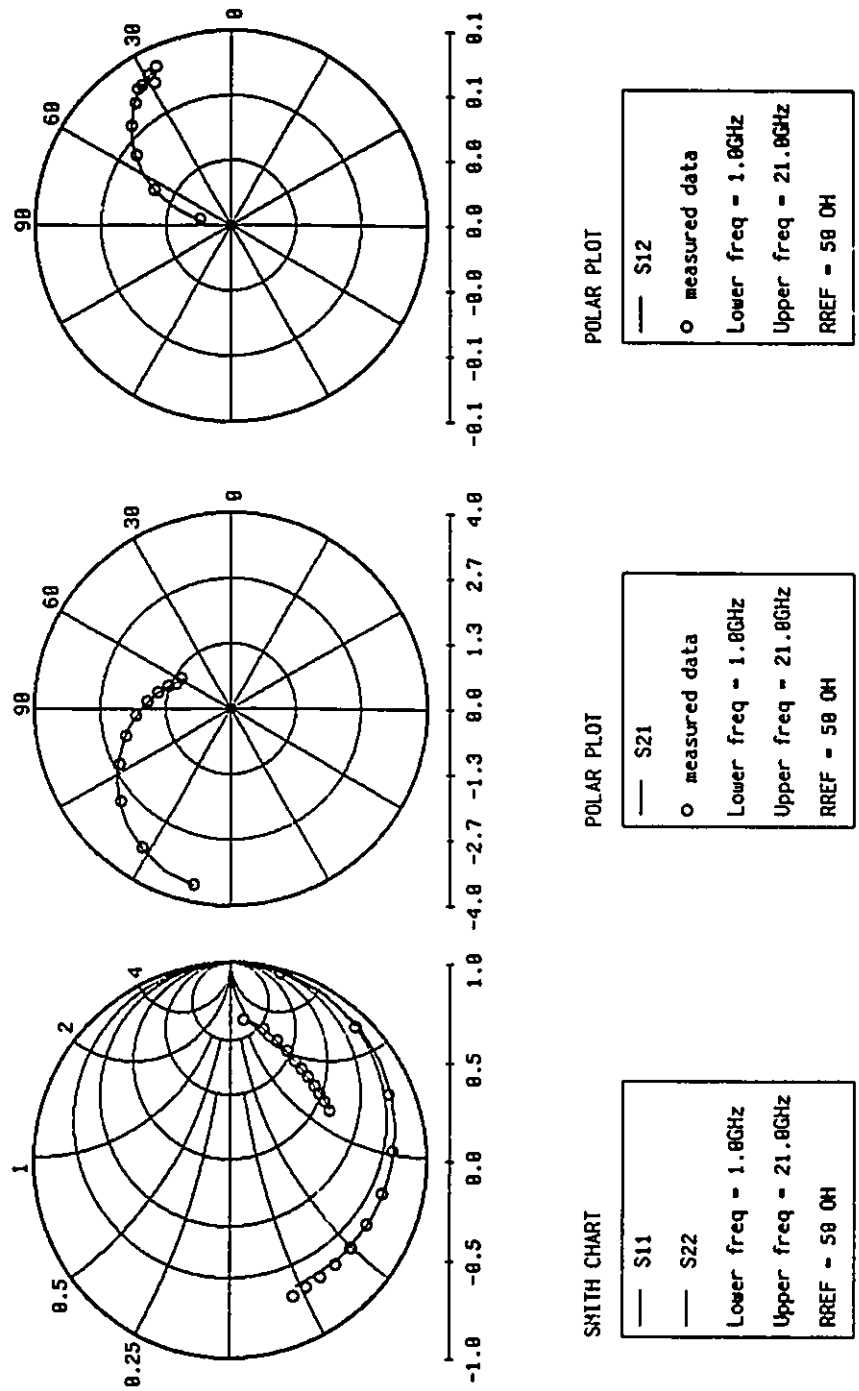

Fig. 5.4 S parameter fit [28]. Circles represent the measured mean-valued S parameters at bias $V_{GS} = 0V$ and $V_{DS} = 5V$. Solid lines are model responses simulated from the mean parameter values of the Materka and Kacprzak model.

V_{GS} = 0V and V_{DS} = 5V. Excellent fit is observed.

The statistical model was examined by Monte Carlo simulation. The statistical S-parameter responses generated by the model were compared with the measurements. The comparison was made at the bias point V_{GS} = 0V and V_{DS} = 5V and at the frequency 11GHz. Monte Carlo simulation was performed with 400 outcomes from the mean values, standard deviations, correlations and DDFs of the model parameters.

The mean values and standard deviations of the measured S parameters and the simulated S parameters from the model are listed in Table 5.2. Histograms of one S parameter is plotted in Fig. 5.5. Though the mean value match appears in good agreement, large mismatch of the standard deviations exists. This indicates that modeling at equivalent circuit parameter level can provide accurate fit for individual devices since it has very few constraints, but may fail to satisfactorily reproduce the original measurement statistics.

5.5 STATISTICAL MODELING WITH PBMs

In this section, we use the Khatibzadeh and Trew model and the Ladbrooke model to demonstrate statistical modeling with PBMs.

5.5.1 Statistical Modeling Using the Khatibzadeh and Trew Model

The Khatibzadeh and Trew model has been discussed in detail in Chapter 2. The model parameters used for statistical modeling include the intrinsic physical parameters listed in Table 2.1 and the extrinsic linear elements shown in Fig. 2.8. The high-field diffusion coefficient D_0 and the linear element C_x are fixed at 0.001m^2/s

TABLE 5.2

MEAN VALUES AND STANDARD DEVIATIONS OF MEASURED S PARAMETERS AND SIMULATED S PARAMETERS FROM THE MATERKA AND KACPRZAK MODEL AT 11GHz [25]

	Measured S parameters		Simulated S parameters	
	Mean	Dev. (%)	Mean	Dev. (%)
$\lvert S_{11}\rvert$	0.773	0.988	0.7725	1.74
$\angle S_{11}$	-114.3	1.36	-114.9	1.63
$\lvert S_{21}\rvert$	1.911	0.802	1.933	15.2
$\angle S_{21}$	93.35	0.856	93.43	0.86
$\lvert S_{12}\rvert$	0.0765	3.77	0.07564	5.07
$\angle S_{12}$	34.00	2.51	33.72	2.14
$\lvert S_{22}\rvert$	0.5957	1.48	0.5935	4.19
$\angle S_{11}$	-38.69	2.10	-37.85	3.31

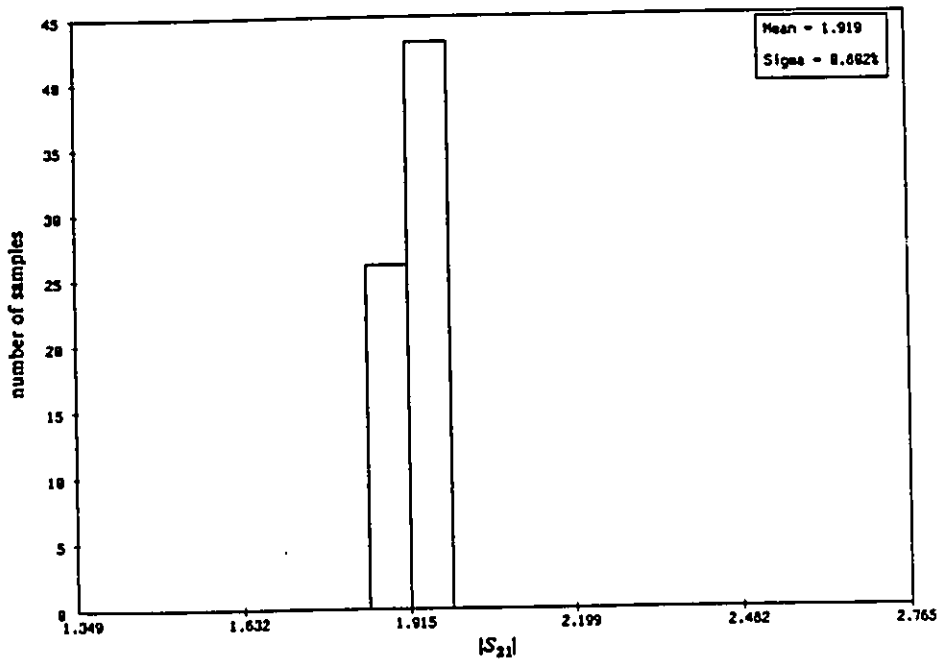

(a)

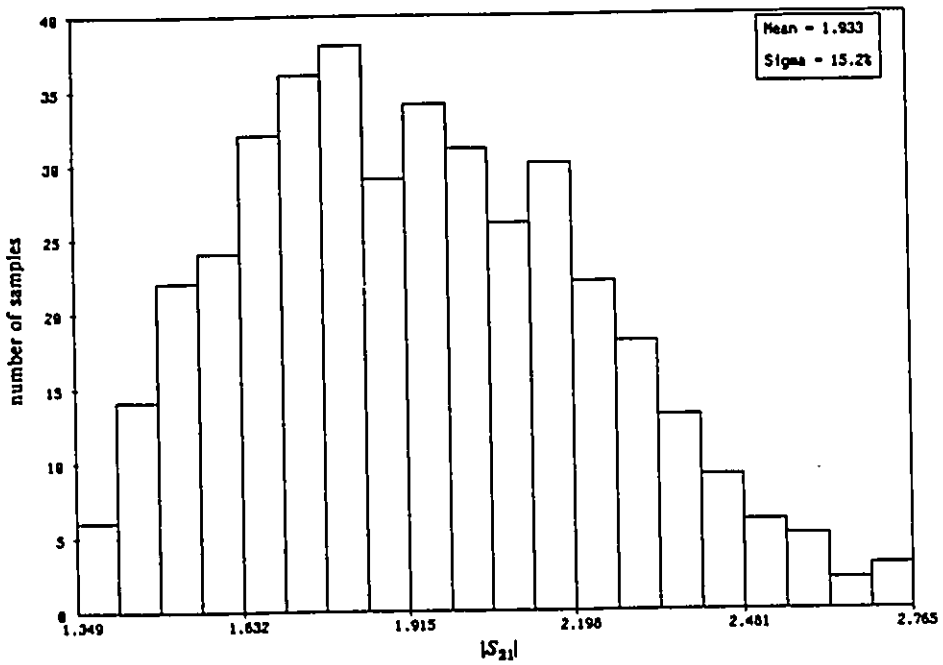

(b)

Fig. 5.5 Histograms of $|S_{21}|$ at V_{GS}=0V and V_{DS}=5V and at 11GHz from (a) measurements and (b) the Materka and Kacprzak model [25].

and 3pF, respectively.

The measurements provided by Plessey Research Caswell [140] used for statistical modeling with the Materka and Kacprzak model are used here for statistical modeling with the Khatibzadeh and Trew model.

HarPE [138] is also used to carry out statistical modeling. The same procedure such as parameter extraction and postprocessing used in Section 5.4 is applied to the Khatibzadeh and Trew model.

The parameter mean values and standard deviations for the Khatibzadeh and Trew model are listed in Table 5.3. The standard deviations of the model parameters appear vary small. The histograms of the FET gate length L, gate width W, channel thickness a and doping density N_d are shown in Fig 5.6 and Fig. 5.7.

Monte Carlo simulation with 400 outcomes is used to examine the resulting statistical model. The simulated S-parameter statistical responses are compared with the measured data at bias point $V_{GS} = 0$V and $V_{DS} = 5$V and at frequency 11GHz. The mean values and the standard deviations of the simulated and measured data are listed in Table 5.4. The histograms of one S parameter are shown in Fig. 5.8. From Table 5.4, we can see that the standard deviations of the S parameters from the Khatibzadeh and Trew model are smaller than those from the measurements except for $|S_{21}|$. This is consistent with the observation that the parameter standard deviations in the Khatibzadeh and Trew model are very small (see Table 5.3). Comparing Table 5.4 with Table 5.2, we can see that the standard deviation match provided by the Khatibzadeh and Trew model are better than that given by the Materka and Kacprzak model, especially for the most important S parameter $|S_{21}|$. On the other hand, the

TABLE 5.3

STATISTICAL PARAMETERS
FOR THE KHATIBZADEH AND TREW MODEL

Parameter	Mean Value	Standard Deviation (%)
$L(\mu m)$	0.5496	1.29
$a(\mu m)$	0.1310	1.38
$W(\mu m)$	295.24	1.48
$N_d(1/m^3)$	2.219×10^{23}	0.98
$V_{bi}(V)$	0.699	1.62
$\mu_0(m^2/Vs)$	0.3932	1.16
$E_c(V/m)$	3.255×10^{5}	1.38
ε_r	12.693	2.10
$L_g(nH)$	2.94×10^{-2}	0.13
$R_g(\Omega)$	3.50	0.12
$R_d(\Omega)$	4.001	0.06
$L_d(nH)$	8.0×10^{-3}	0.06
$R_s(\Omega)$	1.697	0.17
$L_s(nH)$	3.9×10^{-2}	0.85
$G_{ds}(1/\Omega)$	3.6×10^{-3}	0.61
$C_{dc}(pF)$	5.27×10^{-2}	0.78
$C_{gc}(pF)$	0.1504	1.89

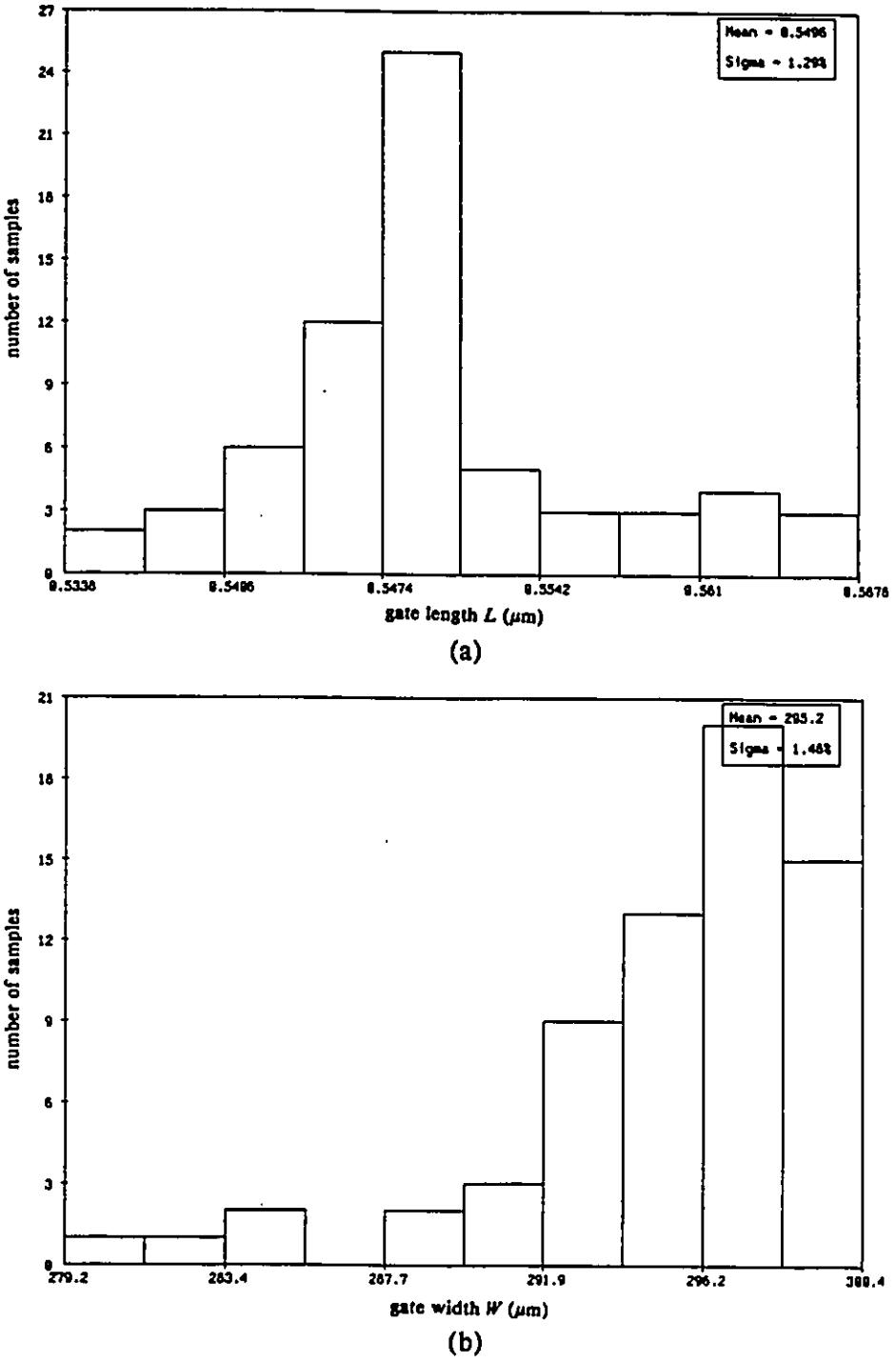

Fig. 5.6 Histograms of (a) gate length L and (b) gate width W of the Khatibzadeh and Trew model.

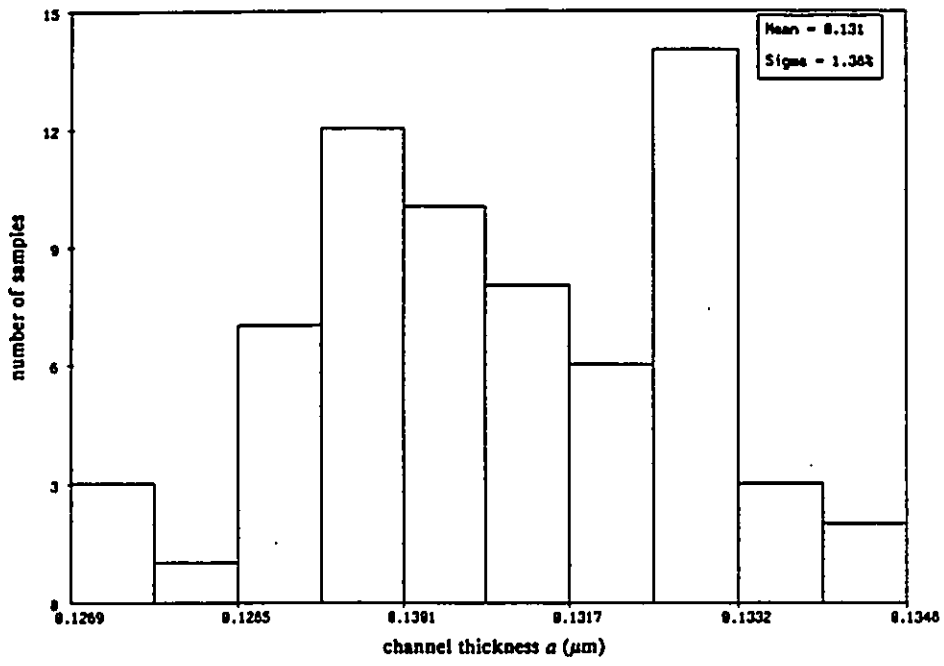

(a)

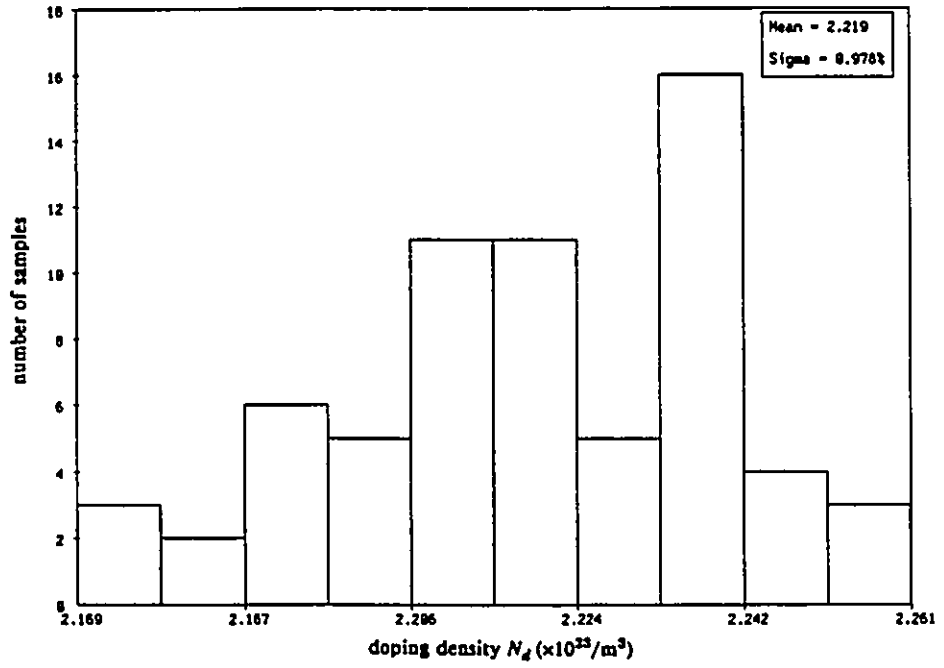

(b)

Fig. 5.7 Histograms of (a) channel thickness a and (b) doping density N_d of the Khatibzadeh and Trew model.

TABLE 5.4

MEAN VALUES AND STANDARD DEVIATIONS OF MEASURED S PARAMETERS AND SIMULATED S PARAMETERS FROM THE KHATIBZADEH AND TREW MODEL AT 11GHz

	Measured S parameters		Simulated S parameters	
	Mean	Dev. (%)	Mean	Dev. (%)
$\|S_{11}\|$	0.773	0.988	0.8085	0.32
$\angle S_{11}$	-114.3	1.36	-116.2	0.69
$\|S_{21}\|$	1.911	0.802	1.834	1.22
$\angle S_{21}$	93.35	0.856	91.69	0.33
$\|S_{12}\|$	0.0765	3.77	0.0785	2.07
$\angle S_{12}$	34.00	2.51	31.61	0.94
$\|S_{22}\|$	0.5957	1.48	0.5446	1.11
$\angle S_{11}$	-38.69	2.10	-40.64	0.98

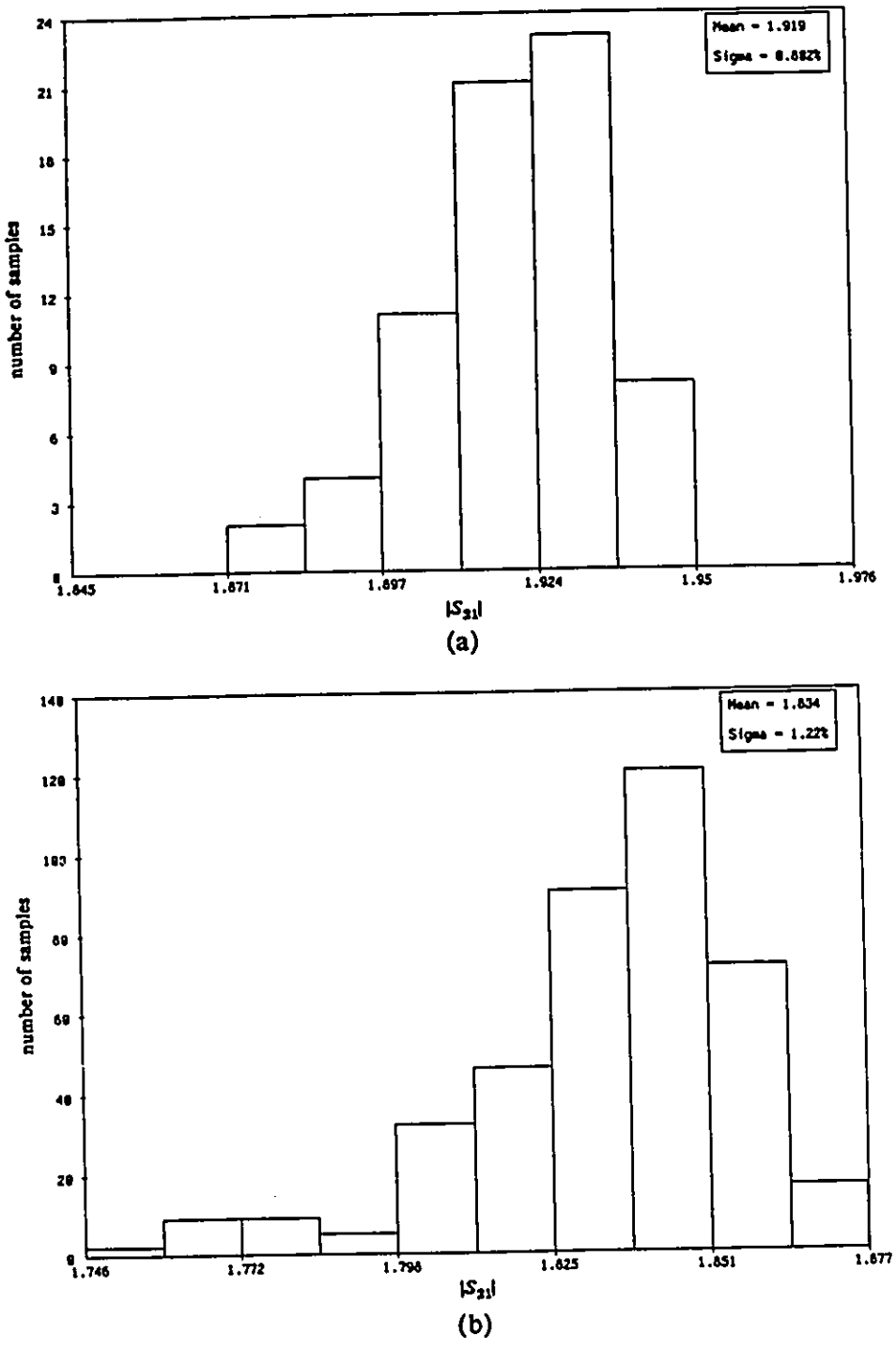

Fig. 5.8 Histograms of $|S_{21}|$ at V_{GS}=0V and V_{DS}=5V and at 11GHz from (a) measurements and (b) the Khatibzadeh and Trew model.

mean value match from the materka and Kacprzak model is better than that from the Khatibzadeh and Trew model.

5.5.2 Statistical Modeling Using the Ladbrooke Model [25]

Bandler, Biernacki, Chen, Song, Ye and Zhang (1991) [25] presented statistical modeling of MESFETs using the Ladbrooke model (Ladbrooke (1989) [78]). The Ladbrooke model is a small-signal model which uses an equivalent circuit whose components are derived from the physical parameters and the bias conditions, such that the model is defined in terms of the device physical parameters.

The model includes the intrinsic FET parameters

$$\{ L, W, a, N_d, V_{b0}, v_s, E_c, \mu_0, \varepsilon, L_{G0}, a_0, r_{01}, r_{02}, r_{03}\}$$

and the linear extrinsic elements

$$\{L_g, R_g, L_d, R_d, L_s, R_s, G_{ds}, C_{ds}, C_x\}$$

where L, W, a, N_d, v_s, E_c, μ_0, as in the Khatibzadeh and Trew model, denote the gate length, gate width, channel thickness, doping density, saturation electron drift velocity, critical electric field, low-field mobility of GaAs, respectively. V_{b0} is the zero-bias barrier potential, ε the permittivity of GaAs, L_{G0}, the inductance from gate bond wires and pads, a_0 the proportionality coefficient, and r_{01}, r_{02} and r_{03} are fitting coefficients [25].

The equivalent circuit of the Ladbrooke model is shown in Fig. 5.9. The bias-dependent small-signal parameters, namely, g_m, C_{gs}, C_{gd}, R_i, L_g, r_0, and τ, are derived using the modified Ladbrooke formulas once the DC operating point is solved for.

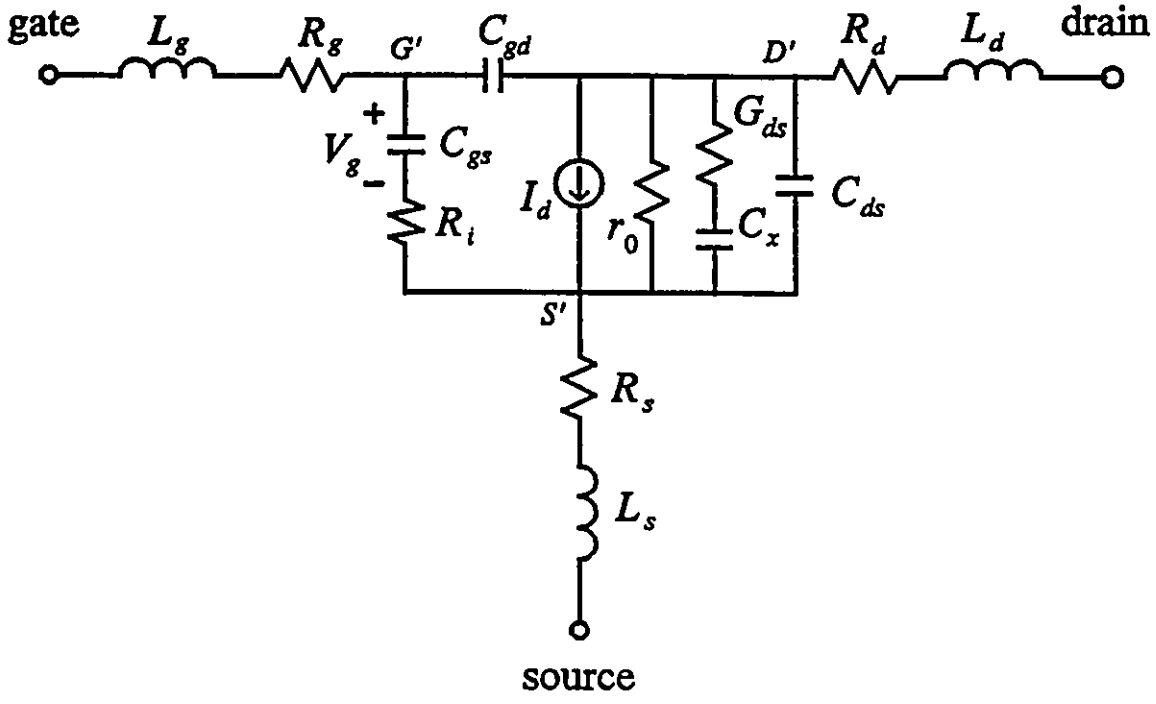

Fig. 5.9 Small-signal equivalent circuit of the Ladbrooke model where $I_d=g_m V_g e^{-j\omega\tau}$ [25].

The formulas are [25,78]

$$g_m = \frac{\varepsilon v_s W}{d} \tag{5.17}$$

$$C_{gs} = \frac{\varepsilon W L}{d}\left[1 + \frac{X}{2L} - \frac{2d}{L + 2X}\right] \tag{5.18}$$

$$C_{gd} = \frac{2\varepsilon W}{1 + \frac{2X}{L}} \tag{5.19}$$

$$R_i = \frac{L}{\mu_0 q N_d W (a - d)} \tag{5.20}$$

$$L_g = \frac{\mu_0 d W}{m^2 L} + L_{g0} \tag{5.21}$$

$$r_0 = r_{01} V_{D'S'}(r_{02} - V_{G'S'}) + r_{03} \tag{5.22}$$

$$\tau = \frac{1}{v_s}\left[\frac{X}{2} - \frac{2dL}{L + 2X}\right] \tag{5.23}$$

where m is the number of the gate fingers. The equivalent depletion depth d and the space-charge layer extension X are defined by [25,78]

$$d = \sqrt{\frac{2\varepsilon(V_{B0} - V_{G'S'})}{qN_d}} \tag{5.24}$$

$$X = a_0(V_{D'G'} + V_{B0})\sqrt{\frac{2\varepsilon}{qN_d(V_{B0} - V_{G'S'})}} \tag{5.25}$$

where $V_{D'S'}$, $V_{G'S'}$ and $V_{D'G'}$ are DC intrinsic voltages from D' to S', from G' to S' and from D' to G', respectively, as shown in Fig. 5.9.

In this model, the DC operating point must be first solved for to determine the bias-dependent parameters. In [78], the DC operating point was calculated separately by adding a substrate current to the channel current. This approach was also used in [25] to determine the DC operating point.

HarPE [138] was also used in [25] to perform statistical modeling. The same procedure as for the Materka and Kacprzak model and the Khatibzadeh and Trew model was applied to the Ladbrooke model. The FET gate width W and the linear element C_x were fixed at 300μm and 2pF, respectively.

The parameter mean values and standard deviations for the Ladbrooke model are listed in Table 5.5. The histograms of the FET gate length L, channel thickness a and doping density N_d are shown in Fig. 5.10 and Fig. 5.11. Comparing Table 5.5 with Table 5.3, we can observe that the parameter standard deviations of the Ladbrooke model are bigger than those of the Khatibzadeh and Trew model.

The Ladbrooke statistical model was also examined by Monte Carlo simulation with 400 outcomes. The simulated S-parameter statistical responses was compared with the measured data at bias point V_{GS} = 0V and V_{DS} = 5V and at frequency 11GHz. The mean values and the standard deviations of the simulated and measured data are listed in Table 5.6. The histograms of one S parameter are shown in Fig. 5.12. We can see from Table 5.6 that the standard deviation match by the Ladbrooke model is good though some mean value discrepancies exist. According to [25], the error in the mean value estimate is largely due to the deficiency of the model in matching the measurements of individual devices. Such deficiency can be viewed as a *deterministic* factor resulting in a deterministic shift in the estimated mean value. If adjusted for such a shift, the discrepancies in the mean values estimated by the Ladbrooke model would be reduced.

TABLE 5.5

STATISTICAL PARAMETERS
FOR THE LADBROOKE MODEL [25]

Parameter	Mean Value	Standard Deviation (%)
$L(\mu m)$	0.5558	2.39
$a(\mu m)$	0.1059	3.64
$N_d(1/m^3)$	3.140×10^{23}	1.71
$V_{B0}(V)$	0.6785	4.94
$v_s(m/s)$	7.608×10^{4}	3.48
a_0	1.031	7.03
$r_{01}(\Omega/V^2)$	1.09×10^{-2}	0.44
$r_{02}(V)$	628.2	6.86
$r_{03}(\Omega)$	13.99	0.44
$R_g(\Omega)$	3.392	4.99
$L_{g0}(nH)$	2.414×10^{-2}	20.7
$L_d(nH)$	6.117×10^{-2}	18.6
$L_s(nH)$	2.209×10^{-2}	10.6
$G_{ds}(1/\Omega)$	2.163×10^{-3}	2.72
$C_{ds}(pF)$	5.429×10^{-2}	2.71

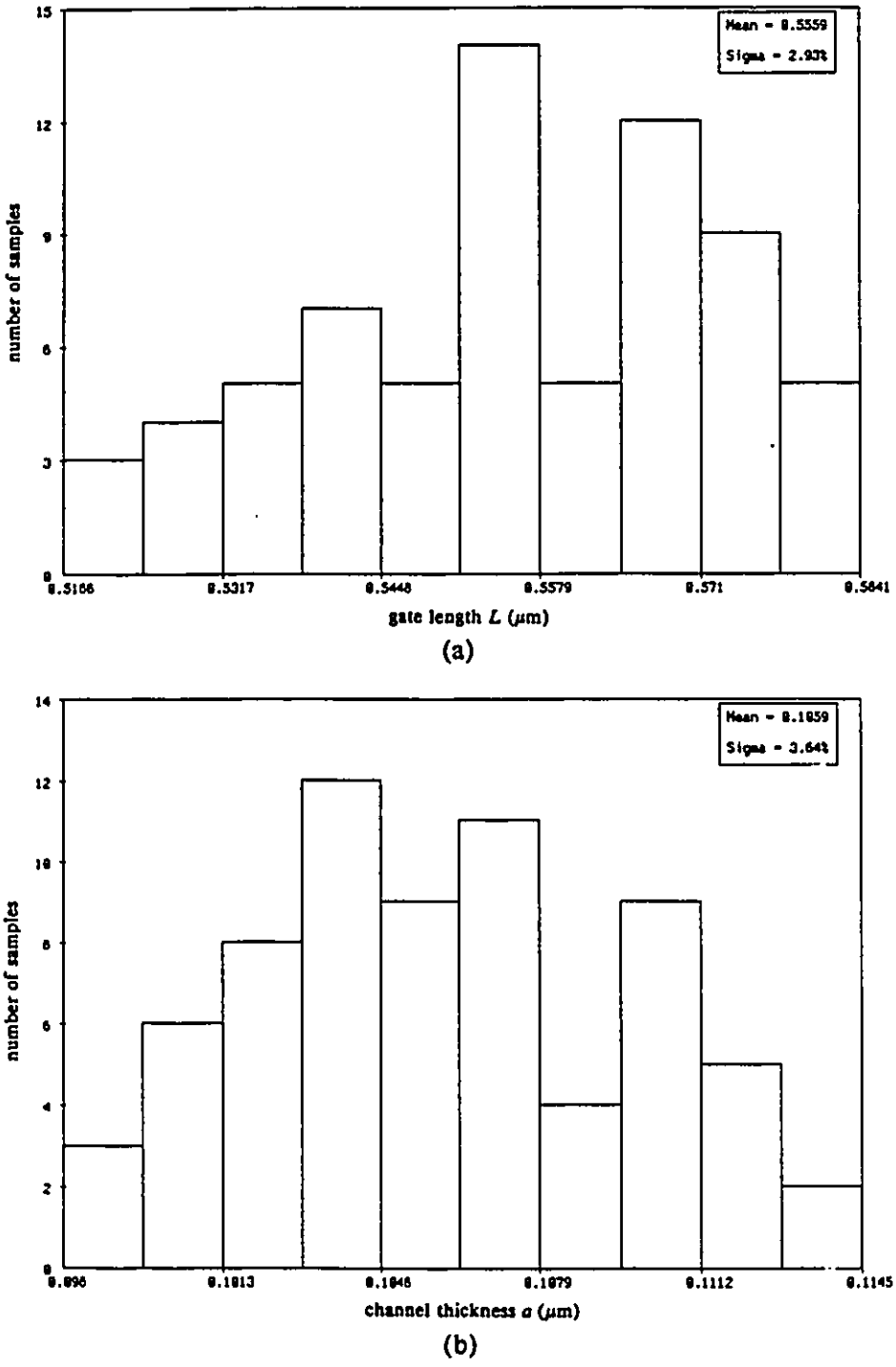

Fig. 5.10 Histograms of (a) gate length L and (b) channel thickness a of the Ladbrooke model [25].

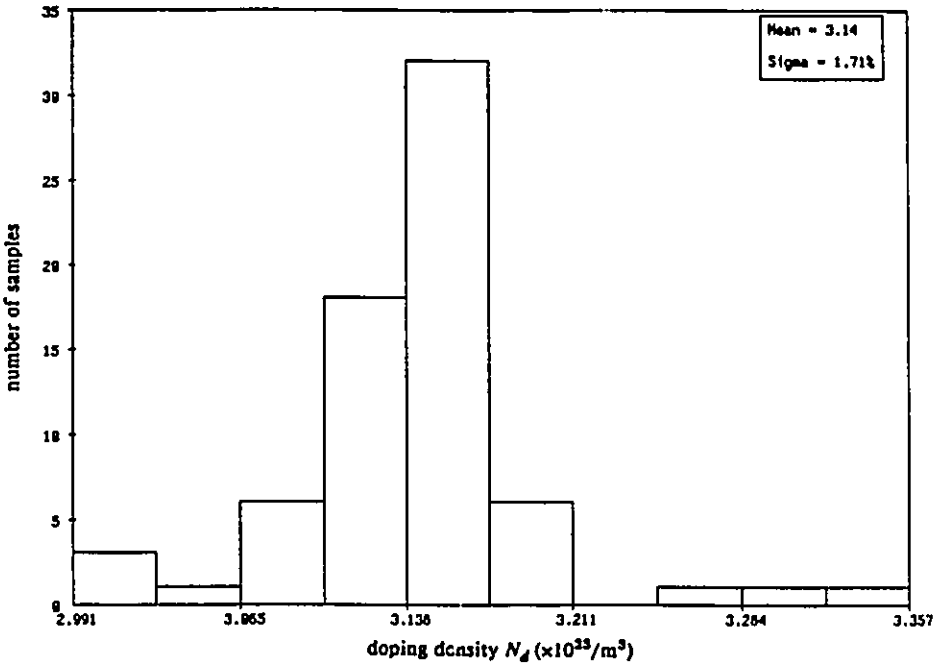

Fig. 5.11 Histograms of doping density N_d of the Ladbrooke model [25].

TABLE 5.6

MEAN VALUES AND STANDARD DEVIATIONS
OF MEASURED S PARAMETERS AND SIMULATED S PARAMETERS
FROM THE LADBROOKE MODEL AT 11GHz [25]

	Measured S parameters		Simulated S parameters	
	Mean	Dev. (%)	Mean	Dev. (%)
$\lvert S_{11}\rvert$	0.773	0.988	0.7856	0.764
$\angle S_{11}$	-114.3	1.36	-119.3	1.10
$\lvert S_{21}\rvert$	1.911	0.802	1.679	1.34
$\angle S_{21}$	93.35	0.856	94.06	0.835
$\lvert S_{12}\rvert$	0.0765	3.77	0.07542	3.68
$\angle S_{12}$	34.00	2.51	31.98	2.33
$\lvert S_{22}\rvert$	0.5957	1.48	0.5838	1.54
$\angle S_{11}$	-38.69	2.10	-36.86	1.42

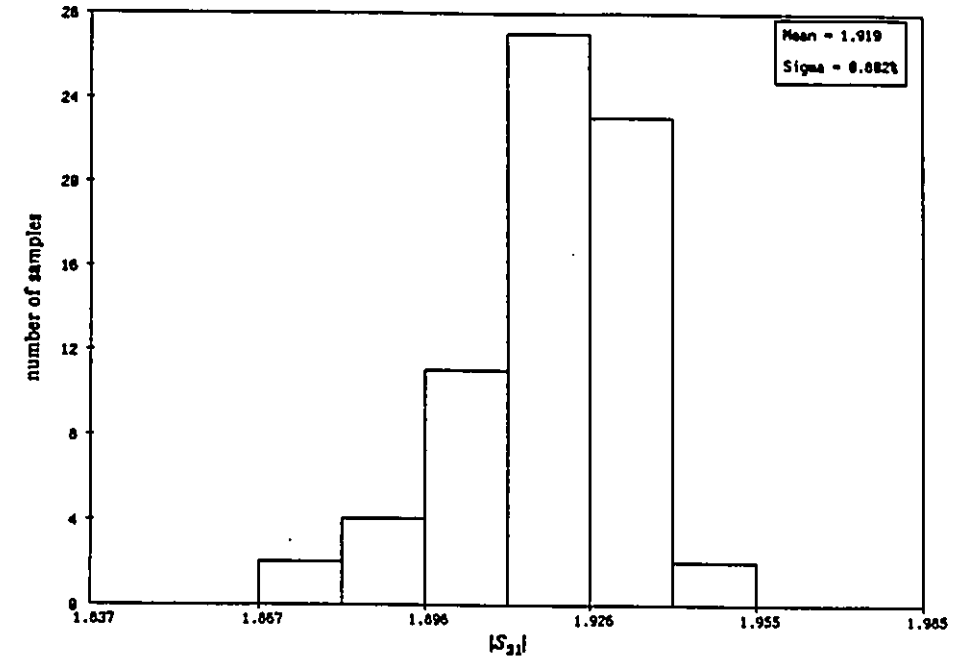

(a)

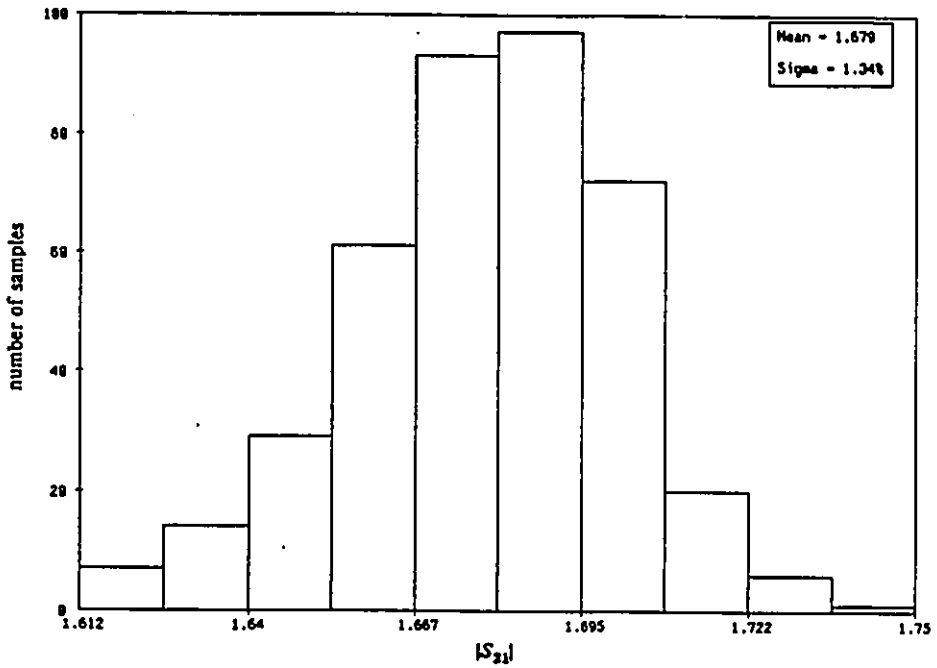

(b)

Fig. 5.12 Histograms of $|S_{21}|$ at V_{GS}=0V and V_{DS}=5V and at 11GHz from (a) measurements and (b) the Ladbrooke model [25].

5.5 CONCLUSIONS

In this chapter, we presented statistical modeling at different levels. Parameter extraction for individual devices by matching the device responses to the corresponding measurements and statistical estimation by postprocessing the sample of models extracted have been addressed. Statistical model verification using Monte Carlo simulation was illustrated.

Statistical modeling with ECMs was demonstrated using the Materka and Kacprzak model. Even though for individual device models the fit of the Materka and Kacprzak model responses to the measurements is excellent, the statistical model based on the extracted Materka and Kacprzak model sample failed to satisfactorily reproduce the original measurement statistics.

Statistical modeling with PBMs was carried out using the Khatibzadeh and Trew model and the Ladbrooke model. The standard deviations of the simulated S parameters from both the Khatibzadeh and Trew model and the Ladbrooke model provide a better match to the measured data than those from the Materka and Kacprzak model. This indicates that PBMs are more suitable for statistical modeling. However, the mean values from both the Khatibzadeh and Trew model and the Ladbrooke model do not fit the measurements as well as the Materka and Kacprzak model. This shows that the PBMs are not flexible enough to provide a very good fit to the measurements for individual devices while the ECMs have more freedom. Among the two PBMs, the Ladbrooke model provides better results than the Khatibzadeh and Trew model. However, the DC operating points have to be determined separately.

Chapter 6

YIELD-DRIVEN CIRCUIT DESIGN

6.1 INTRODUCTION

In integrated circuit (IC) manufacturing, fabricated circuits and devices exhibit parameter values deviating randomly from their nominal (or designed) values. These random variations result in statistical spreads of circuit or device responses and directly affect production yield, as some manufactured circuits or devices violate the design specifications. Therefore, yield optimization is now accepted as an indispensable component of circuit design methodology.

Yield optimization techniques can be traced back to the early 1970s. The pioneering work was carried out by many researchers including Karafin (1971) [72], Pinel and Roberts (1972) [93], Bandler (1972,1973) [6], (1973) [7] and (1974) [8], and Bandler, Liu and Tromp (1976) [9,10]. Most of them dealt with design tolerances, optimal tuning and alignment problems.

A number of approximation approaches to yield optimization were developed during the late 1970s and 1980s. Several typical methods are discussed here.

Director and Hachtel (1977) [50] presented a simplicial approximation approach for design centering. It is a geometric based method which locates and approximates the boundary of the feasible region in an n-dimensional design space with a polyhedron of bounding $(n - 1)$-simplices. The design centering problem is

solved by determining the center of the largest hypersphere inscribed within this polyhedron. The center of the largest hypersphere can be found by linear programming. This approach is based on an essential assumption of a convex acceptable region which limits its application.

Bandler and Abdel-Malek (1978) [11] proposed a method of updated approximations and cuts for optimal design centering, tolerancing and yield determination. In this method low-order multidimensional polynomial approximations are made to all the constraints. These approximations are continually updated during optimization. The yield and yield sensitivities are evaluated using an analytical approach based on the hypervolume formula of the intersection of the non-acceptable region and the tolerance region derived from linear cuts of the tolerance region.

A statistical exploration approach to design centering was presented by Soin and Spence (1980) [120]. They used Monte Carlo analysis to constitute a random sampling, or statistical exploration, of the tolerance region. Following the Monte Carlo analysis, which identifies each circuit outcome as 'pass' or 'fail' accordingly, the centers of gravity of both the pass and fail outcomes are determined. The line joining these two points determines the direction along which a new nominal point is to be found to increase the yield. The actual distance from the old nominal point to the new nominal point is some fraction λ of the distance between the two centers of gravity. In this method, the relation between the yield and two gravity centers is not clear and the fraction λ is very difficult to obtain for general cases.

Statistical design centering and tolerancing using parametric sampling was presented by Singhal and Pinel (1981) [114]. The main principle of their method is

to replace the original probability density function by some other density function called the sampling density. The sampled statistical outcomes and the circuit responses are generated only once using the Monte Carlo analysis with a sampling distribution and stored in a database for yield estimation and optimization. Thus the Monte Carlo analysis is outside the design loop and no new circuit simulations are required during the optimization if the tolerance region is inside the database. However, a new database has to be generated when the optimization leads some outcomes out of the present database.

Styblinski and Ruszczynski (1983) [127] proposed a stochastic approximation approach to statistical circuit design. In their method, yield optimization is considered as a problem of finding the maximum of a regression function. The stochastic approximation approach is used to solve this problem. An algorithm analogous to the conjugate gradient method was introduced with the gradient of yield initially estimated based on one outcome only. Fast initial convergence of this algorithm was demonstrated by an example with the starting point selected outside the acceptable region. However, the algorithm exhibits slow convergence when close to the solution.

A quadratic approximation method was given by Biernacki and Styblinski (1986) [32]. They used a quadratic model in polynomial form to approximate the circuit responses. The model was created using the so called maximally flat quadratic interpolation. This approach was further developed by Biernacki, Bandler, Song and Zhang (1989) [33] and Bandler, Biernacki, Chen, Song, Ye and Zhang (1991) [26] to increase the efficiency and include approximation to the gradients of the circuit responses w.r.t. the design variables.

Bandler and Chen (1988) [15] proposed a one-sided ℓ_1 centering approach. A generalized ℓ_p function is created from the error functions. Based on the ℓ_p function, a one-sided ℓ_1 objective function which approximates the number of unacceptable outcomes is formulated. Then the maximization of yield is converted to the minimization of this objective function. One important feature of this approach is its capability of accommodating arbitrary distributions. This approach has been used by Bandler, Zhang, Song and Biernacki (1989,1991) [22,24] for yield optimization of nonlinear circuits. It was also applied to physics-based yield optimization (Bandler, Cai, Biernacki, Chen and Zhang (1991) [28] and Bandler, Ye, Cai, Biernacki and Chen (1992) [30]). Very promising results were demonstrated.

In this chapter, we present yield-driven circuit design using PBMs. We integrate the concept of yield optimization with PBMs and the FAST sensitivity technique and directly consider as design variables the physical parameters, both for active and passive devices. Statistical PBMs are employed to generate random circuit outcomes for simulation. FAST is utilized to permit high-speed gradient-based yield optimization. Formulation of one-sided ℓ_1 yield optimization with the generalized ℓ_p function is described. Predictable yield-driven circuit design exploiting a novel statistical MESFET model is presented.

6.2 FORMULATION OF YIELD OPTIMIZATION

Assume that there are N_{fail} failed circuits out of a total of N outcomes. The production yield is simply defined as

$$Y = 1 - \frac{N_{fail}}{N} \tag{6.1}$$

In order to utilize the advanced mathematical optimization techniques, we need to convert the yield optimization to a well behaved mathematical programming problem.

The one-sided ℓ_1 approach proposed by Bandler and Chen (1989) [15] is employed for yield optimization using PBMs.

Let the parameters of a nominal circuit be ϕ^0 including the physical parameters of active and passive elements. The manufactured outcomes ϕ^i, $i = 1, 2, \ldots, N$, are spread around ϕ^0 according to the statistical distributions of the parameters and can be represented by

$$\phi^i = \phi^0 + \Delta\phi^i. \tag{6.2}$$

For the ith outcome and the jth design specification S_j, $j = 1, 2, \ldots, m$, the error is defined as

$$e_j(\phi^i) = R_j(\phi^i) - S_j \tag{6.3a}$$

if S_j is an upper specification, or as

$$e_j(\phi^i) = S_j - R_j(\phi^i) \tag{6.3b}$$

if S_j is a lower specification.

During yield optimization, which takes place at the design stage, the outcomes ϕ^i cannot be the manufactured ones. Instead, they are generated from the statistical models, and the yield optimization problem is defined for those simulated random outcomes. Let all the errors for the ith outcome be assembled into the vector

$$e(\phi^i) = \begin{bmatrix} e_1(\phi^i) \\ e_2(\phi^i) \\ . \\ . \\ . \\ e_m(\phi) \end{bmatrix} \tag{6.4}$$

If all the entries of $e(\phi^i)$ are nonpositive, the outcome ϕ^i is acceptable, i.e., it meets all the specifications. From (6.4) the generalized ℓ_p function $v(\phi^i)$ is created as

$$v(\phi^i) = \begin{cases} \left[\sum_{j \in J(\phi^i)} [e_j(\phi^i)]^p \right]^{\frac{1}{p}} & \text{if } J(\phi^i) \neq \emptyset \\ - \left[\sum_{j=1}^{m} [-e_j(\phi^i)]^{-p} \right]^{-\frac{1}{p}} & \text{if } J(\phi^i) = \emptyset \end{cases} \tag{6.5}$$

where

$$J(\phi^i) = \{ j \mid e_j(\phi^i) \geq 0 \} \tag{6.6}$$

The one-sided ℓ_1 objective function for yield optimization [15] can be formulated as

$$U(\phi^0) = \sum_{i \in I} \alpha_i \, v(\phi^i) \tag{6.7}$$

where

$$I = \{ i \mid v(\phi^i) > 0 \} \tag{6.8}$$

and α_i are positive multipliers. If α_i are chosen as [15]

$$\alpha_i = \frac{1}{| v(\phi^i) |} \tag{6.9}$$

the value of function $U(\phi^0)$ would be equal to N_{fail} and the yield would be

$$Y(\phi^0) = 1 - \frac{U(\phi^0)}{N} \tag{6.10}$$

Hence, the relation between yield and the error functions is established. The

maximization of yield is converted to minimization of $U(\phi^0)$, i.e.,

$$\underset{\phi^0}{\text{minimize}}\ U(\phi^0) \tag{6.11}$$

In our implementation the α_i are assigned according to (6.9) only at the starting point and then it is kept fixed during optimization. As a consequence, $U(\phi^0)$ is no longer equal to N_{fail} when optimization proceeds, but it provides a continuous approximation to N_{fail} [15].

6.3 FAST GRADIENT-BASED YIELD OPTIMIZATION [24]

Gradient-based yield optimization involves repeated simulation of a large number of statistical outcomes and requires sensitivity analysis to estimate the gradients of the error functions. Therefore, an effective and efficient approach to gradient calculation is very important. Two gradient estimation techniques IGAT and FAST, as discussed in Chapter 4, have been used in yield optimization of nonlinear circuits (Bandler, Zhang, Song and Biernacki (1990) [24]). Here, we use FAST for physics-based yield optimization.

In order to solve the yield optimization problem (6.11), we need to calculate the gradients of the objective function U w.r.t. the designable variables. Let ϕ_k^0 be a generic designable variable out of ϕ^0. Then, from (6.7) the gradient of U w.r.t. ϕ_k^0 is

$$\frac{\partial U(\phi^0)}{\partial \phi_k^0} = \sum_{i \in I} \alpha_i \frac{\partial v(\phi^i)}{\partial \phi_k^0} \tag{6.12}$$

Differentiating (6.5) w.r.t. ϕ_k^0 we obtain, if $J(\phi^i) \neq \varnothing$

$$\frac{\partial v(\phi^i)}{\partial \phi_k^0} = \left[\sum_{j \in J(\phi^i)} [e_j(\phi^i)]^p\right]^{\frac{1}{p}-1} \sum_{j \in J(\phi^i)} [e_j(\phi^i)]^{p-1} \left[\frac{\partial e_j(\phi^i)}{\partial \phi^i}\right]^T \frac{\partial \phi^i}{\partial \phi_k^0} \tag{6.13}$$

From (6.2) we have $\frac{\partial \phi^i}{\partial \phi_k^0} = u_k$, unless a relationship between ϕ^i and ϕ^0 exists, which differs from (6.2) (e.g., a relative perturbation). Following (6.3a) and (6.3b) the computation of $\frac{\partial e_j(\phi^i)}{\partial \phi^i}$ can be converted to the calculation of the gradients of circuit responses by expressing the gradient of $e_j(\phi^i)$ w.r.t. the lth element ϕ_l^i in ϕ^i as

$$\frac{\partial e_j(\phi^i)}{\partial \phi_l^i} = \pm \frac{\partial R_j(\phi^i)}{\partial \phi_l^i} \tag{6.14}$$

where the sign depends on the type of the specification S_j. If S_j is an upper (lower) specification, the positive (negative) sign is used. Finally, the FAST technique discussed in Chapter 4 is used to evaluate $\frac{\partial R_j(\phi^i)}{\partial \phi_l^i}$.

Usually, a nominal design is carried out before yield optimization. The solution of the nominal design is then used as the initial point for yield optimization.

The entire procedure of yield optimization can be illustrated by the flowchart shown in Fig. 6.1. In yield optimization we typically deal with four types of parameters, namely, designable variables with statistics, designable variables without statistics, non-designable variables with statistical variations, and fixed parameters. The FAST sensitivity calculation is required only for design variables. The statistical outcomes are generated from the parameters with statistical variations while keeping other parameters at their nominal values.

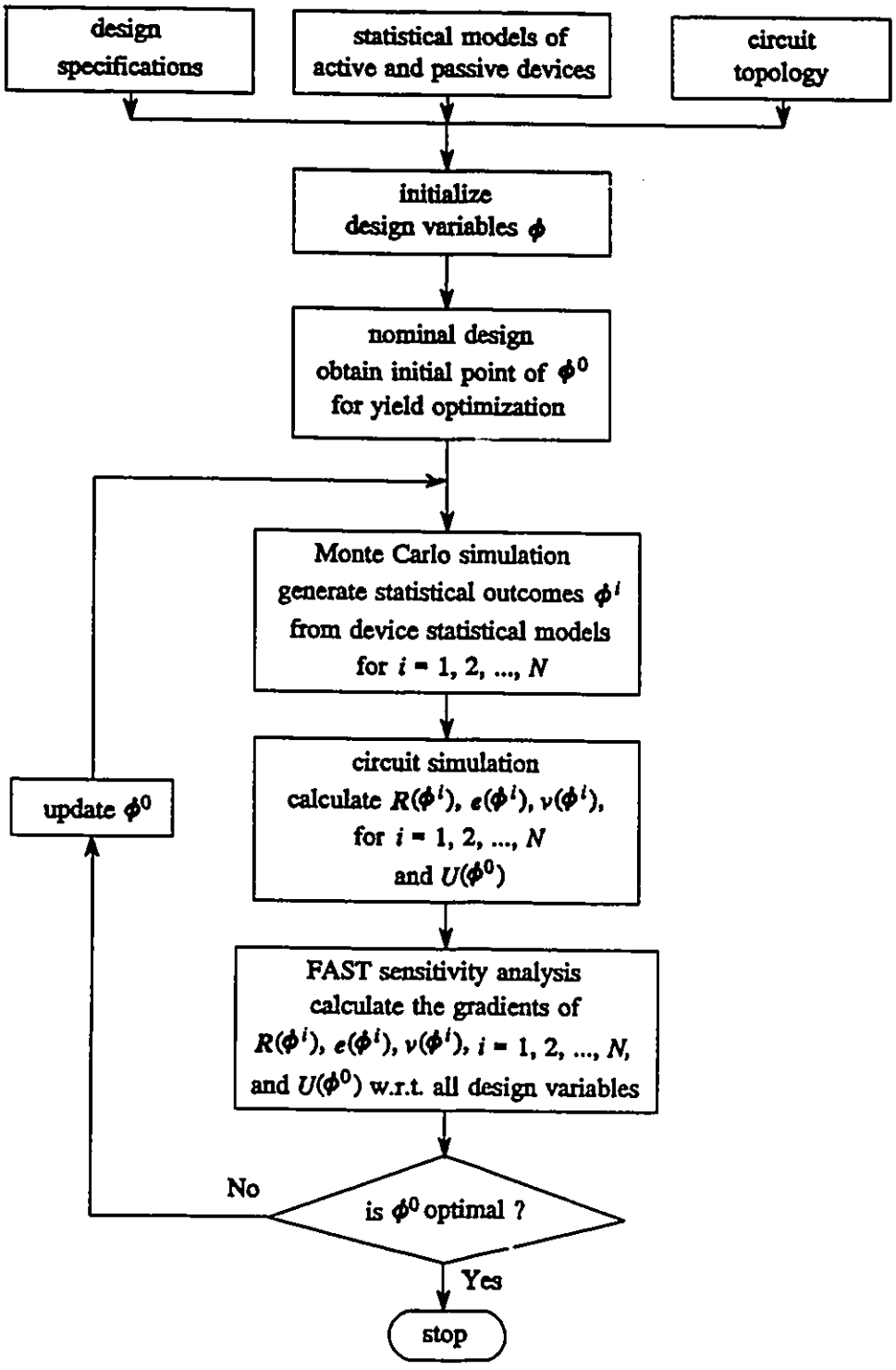

Fig. 6.1 Flowchart for yield optimization.

6.4 YIELD OPTIMIZATION OF MMICs

In this section, we present yield optimization of MMICs with PBMs. As design variables we directly consider physical parameters for both active devices and passive components. The parameters may include, for example, FET gate length, gate width, doping density, the number of turns of spiral inductors, geometrical dimensions of metal-insulator-metal (MIM) capacitors, etc.

6.4.1 PBMs for MMIC Passive Components

We use the PBM described in Chapter 2 to model GaAs MESFETs. Passive components are modeled through their equivalent circuits and the corresponding n-port Y matrices. The values of the equivalent circuit elements are derived from material and geometrical parameters. Since the MMICs are manufactured on a common semi-insulating substrate these equivalent models are grounded, e.g., a "two terminal component" is represented by a two-port. From these equivalent circuits we calculate the corresponding Y matrices. In general,

$$I = Y(\phi)V \tag{6.15}$$

where ϕ stands for physical parameters, and I and V are port current and voltage vectors.

For MIM capacitors ϕ includes the geometrical dimensions of the metal plate, the permittivity and the thickness of the dielectric film. For spiral inductors, ϕ includes the substrate height, the conductor width and spacing, and the number of turns. For planar resistors ϕ includes the geometrical dimensions and resistivities of the resistive films. These three typical MMIC passive components are discussed here.

The configuration of a spiral inductor and its corresponding equivalent circuit are shown in Fig. 6.2. R, C_1, C_2 and C_3 are the parasitic elements associated with the inductor L. Following Bahl (1988) [5], the values of L, R and C_3 can be calculated from the physical parameters by

$$L(\text{nH}) = 0.03937K_g \frac{n^2(d_o + d_i)^2}{32(d_o + d_i) + 88(d_o - d_i)} \tag{6.16}$$

$$R(\Omega) = \frac{K\pi nr_s(d_o + d_i)}{4w} \tag{6.17}$$

$$C_3(\text{pF}) = 3.5\times10^{-5}d_o + 0.06 \tag{6.18}$$

where d_o and d_i are the outer and inner diameters, n is the number of turns, w is the width, r_s is the sheet resistivity in ohms per square, K and K_g are the correction factors as defined in [5]. The parasitic capacitances C_1 and C_2 can not be easily calculated for a spiral inductor [5]. Their values can be obtained by fitting the model responses to the corresponding measurements. They are neglected in our experiment.

It has been pointed out that $d_o = 5d_i$ will optimize the Q factor [5]. If we use this condition and let [5]

$$d_o = 1.25[2n(w + s) + (w - s)] \tag{6.19}$$

then

$$d_i = \frac{d_o}{5} = 0.25[2n(w + s) + (w - s)] \tag{6.20}$$

and (6.16) is changed to

$$L(\text{nH}) = 0.03937K_g \frac{0.375^2n^2[2n(w + s) + (w - s)]}{8.5} \tag{6.21}$$

where s is the separation space between turns.

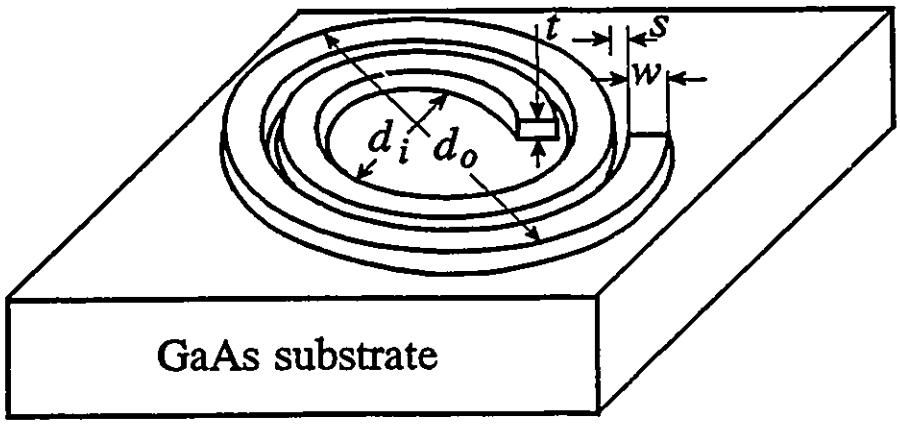

(a)

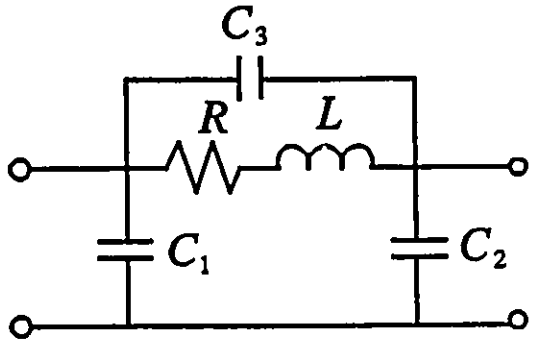

(b)

Fig. 6.2 Configuration of a spiral inductor (a) and its corresponding equivalent circuit (b) [5].

Fig. 6.3 shows a MIM capacitor and its corresponding equivalent circuit. R, L, G, C_1 and C_2 are the parasitic elements associated with capacitor C. The values of these elements (excluding L) can be calculated using the following formulas [5].

$$C(\text{pF}) = \frac{10^{-3}\varepsilon_{rd} w l}{36\pi d} \tag{6.22}$$

$$R(\Omega) = \frac{K l r_s}{w + t} \tag{6.23}$$

$$G(1/\Omega) = \omega C \tan\delta \tag{6.24}$$

$$C_1 = C_2(\text{pF}) = 10^{-2} l \left[\frac{\sqrt{\varepsilon_e}}{Z_0(w, h, \varepsilon_r)} - \frac{\varepsilon_r w}{36\pi h} \right] \tag{6.25}$$

where ε_e is the effective permittivity of microstrip line of width w, Z_0 is the characteristic impedance, h is the substrate thickness, ε_r is the relative permittivity of the substrate, ε_{rd} is the relative permittivity of the dielectric film, $\tan\delta$ is its loss tangent, l and t are the length and thickness of the metal plates, respectively, K is the correction factor, and ω is the angular frequency.

It is difficult to accurately calculate the parasitic inductor L. Its value could be roughly estimated with some simplifying assumptions (Ladbrooke (1989) [78]). It is also neglected in our experiment.

Fig. 6.4 shows a planar resistor and its associate equivalent circuit. L, C_1 and C_2 are parasitic elements. Following Goyal, Golio and Thomann (1989) [60], the resistance can be calculated by

$$R = \frac{l r_s}{w} \tag{6.26}$$

where l and w are the length and width of the resistive film, respectively.

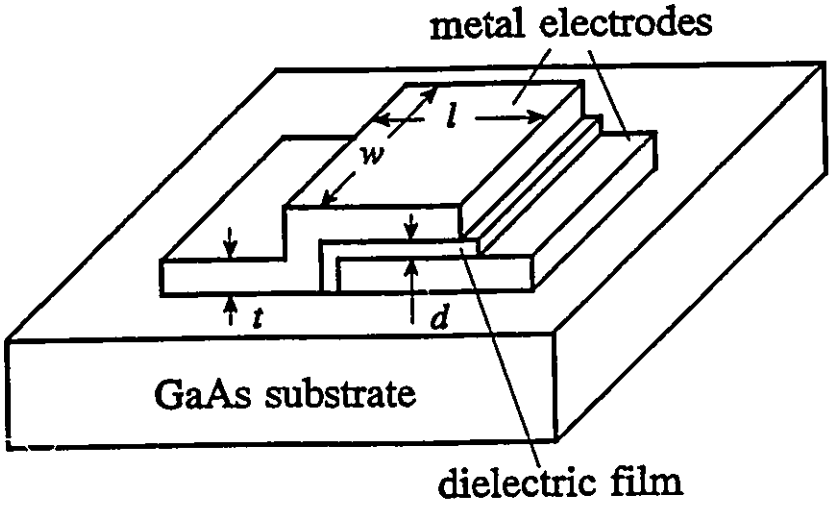

(a)

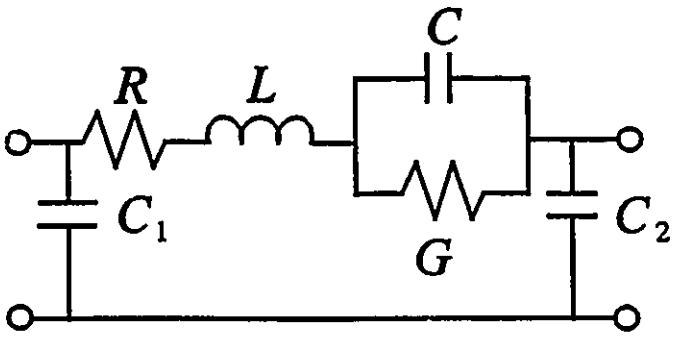

(b)

Fig. 6.3 Configuration of a MIM capacitor (a) and its corresponding equivalent circuit (b) [5].

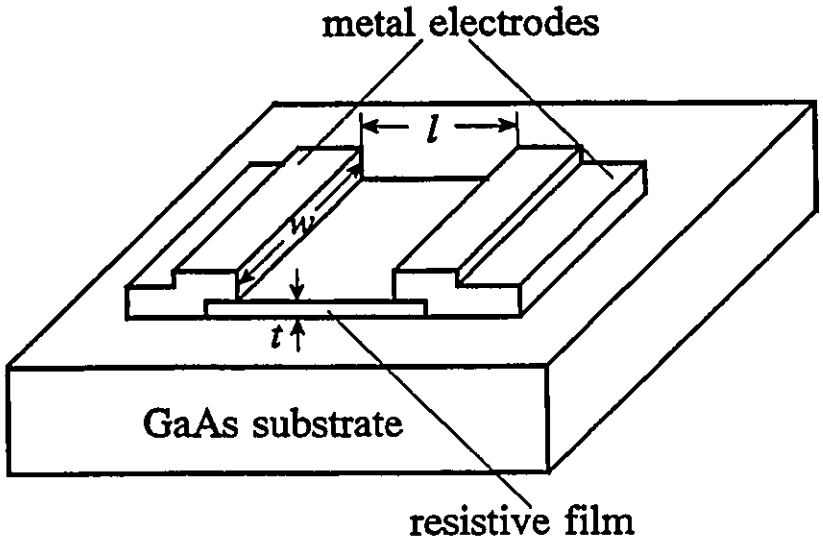

(a)

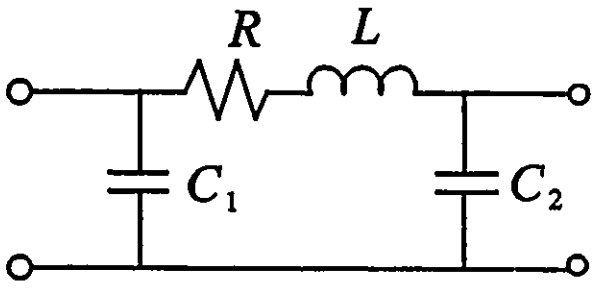

(b)

Fig. 6.4 Configuration of a planar resistor (a) and its corresponding equivalent circuit (b) [60].

For use at high frequencies, the parasitic capacitances C_1 and C_2 and the parasitic inductance L should be considered. The impedance of the resistor could be evaluated by [60]

$$Z(\omega) = R\left[AB\tanh(\frac{A}{B})\right] \tag{6.27}$$

where

$$A = \sqrt{1 + j\frac{Z_0}{R}\theta} \tag{6.28a}$$

$$B = \sqrt{\frac{Z_0}{R}\times\frac{1}{j\theta}} \tag{6.28b}$$

$$\theta = \frac{\omega l}{\upsilon} \tag{6.28c}$$

where Z_0 and υ are the characteristic impedance and phase velocity of the resistive segment, treated as a lossless transmission line. In our experiment L, C_1 and C_2 are ignored.

In the preceding equations, all geometrical dimensions are in μm.

6.4.2 Yield Optimization of A Three Stage X-band MMIC Amplifier

We consider a three stage small-signal X-band cascadable MMIC amplifier shown in Fig. 6.5. The design is based on the circuit topology and the fabrication layout described in [74], but with different parameter values. The amplifier contains three MESFETs using an interdigitated structure with two gate fingers of dimensions 150μm×1.0μm. The matching circuits are composed of inductors and capacitors arranged in bandpass topology. All passive components are realized using lumped MMIC elements: spiral inductors, MIM capacitors and bulk resistors. The second and

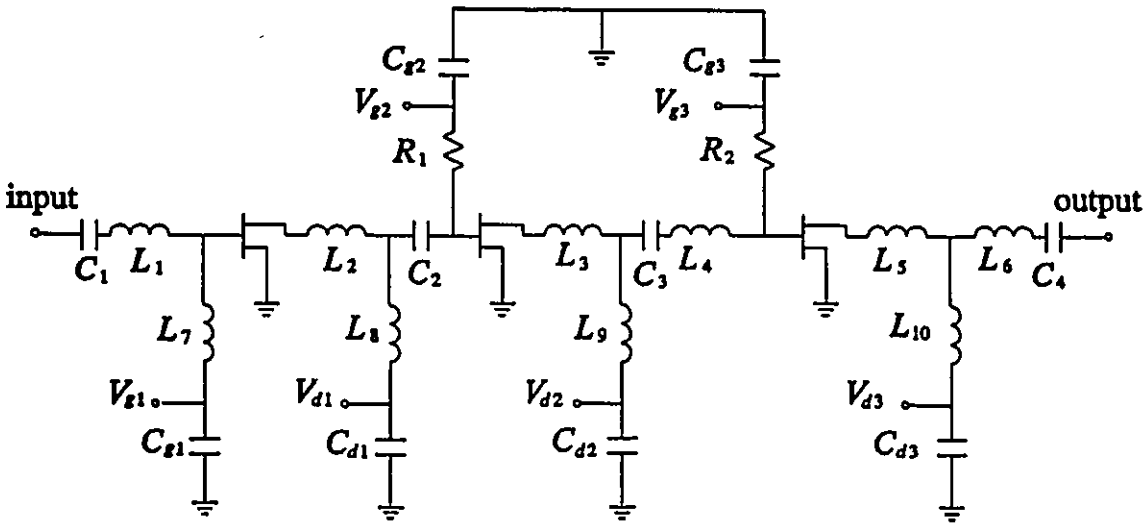

Fig. 6.5 Circuit diagram of an X-band amplifier [74].

third MESFETs are biased through 1500Ω GaAs bulk resistors. The drains and the first gate bias are bypassed by high value MIM capacitors. The input (output) matching circuit includes a series capacitor to make the amplifier cascadable without additional components.

The amplifier is to meet the following specifications: in the passband (8GHz - 12GHz) gain = 14±1.5dB, input and output VSWR < 2.5; in the stopband (below 6GHz or above 15GHz) gain < 2dB.

We use the PBMs for both the MESFETs and the passive elements. From the models for passive elements discussed in Section 6.4.1, we select only the major components in their corresponding equivalent circuits. In other words, we consider only the capacitance C for MIM capacitor, the inductance L for spiral inductor and resistance R for planar resistor and disregard other parasitic components.

Since all devices are made from the same material and on the same wafer, they share common parameters. All three MESFETs have the same values for the critical electric field, saturation velocity, relative permittivity, built-in potential, low-field mobility and high-field diffusion coefficient. All the MIM capacitors have the same dielectric film, and all bulk resistors have the same sheet resistance. The geometrical parameters can have different values for different devices, including the gate length, gate width, and channel thickness of the MESFETs, the metal plate area of the MIM capacitors, and the number of turns of the spiral inductors. The doping densities of the MESFETs are also considered as independent parameters.

First, a nominal design is performed using the minimax optimizer of OSA90/hope [139]. As in a traditional design, only the matching circuits are

optimized. The parameters of the active devices (MESFETs) have fixed values which are listed in Table 6.1. There are 14 design variables, namely, S_{C1}, S_{C2}, S_{C3}, S_{C4} (the area of the metal plate of MIM capacitors C_1, C_2, C_3 and C_4), n_{L1}, n_{L2}, ..., n_{L10} (the number of turns of the spiral inductors L_1, L_2, .., L_{10}). The values of the capacitors and inductors given in [74] were used to select the initial values for these variables. The nominal solution was achieved by minimax optimization after 15 iterations (about 5 minutes on a Sun SPARCstation 1). The gain and input VSWR before and after optimization are shown in Fig. 6.6. The parameter values for the passive elements before and after optimization are listed in Table 6.2.

The nominal design is then used as the starting point for yield optimization. A total of 37 parameters are considered as statistical variables. They include the gate length, gate width, channel thickness and doping density of the MESFETs, as well as the geometrical parameters of the passive elements. The extrinsic parasitic parameters of the MESFETs are assumed independent, non-designable and without statistical variations. The mean values and standard deviations of the statistical variables are listed in Table 6.3. The correlation matrix used is given in Table 6.4. The most significant correlations are between the corresponding parameters for different devices. For instance, the gate lengths of the three MESFETs are strongly correlated. In addition to the number of turns of the 10 spiral inductors and the metal plate areas of the 4 MIM capacitors, the gate length, gate width, channel thickness and doping density of the MESFETs are chosen as the variables for yield optimization.

TABLE 6.1

PARAMETER VALUES FOR THE THREE MESFETS

Parameter	Values	Parameter	Values
$L(\mu m)$	1.0	$R_g(\Omega)$	2.5
$W(\mu m)$	300	$R_s(\Omega)$	3.5
$N_d(1/m^3)$	1.0×10^{23}	$R_d(\Omega)$	3.5
$a(\mu m)$	0.3	L_g(nH)	0.05
V_{bi}(V)	0.7	L_s(nH)	0.08
$D_0(m^2/s)$	1.0×10^{-3}	L_d(nH)	0.08
E_c(V/m)	3.75×10^5	C_{ds}(pF)	0.001
v_s(m/s)	1.5×10^5	C_{gc}(pF)	0.1
ε_r	12.9	C_{dc}(pF)	0.1
		C_x(pF)	10
		$G_{ds}(1/\Omega)$	0.003

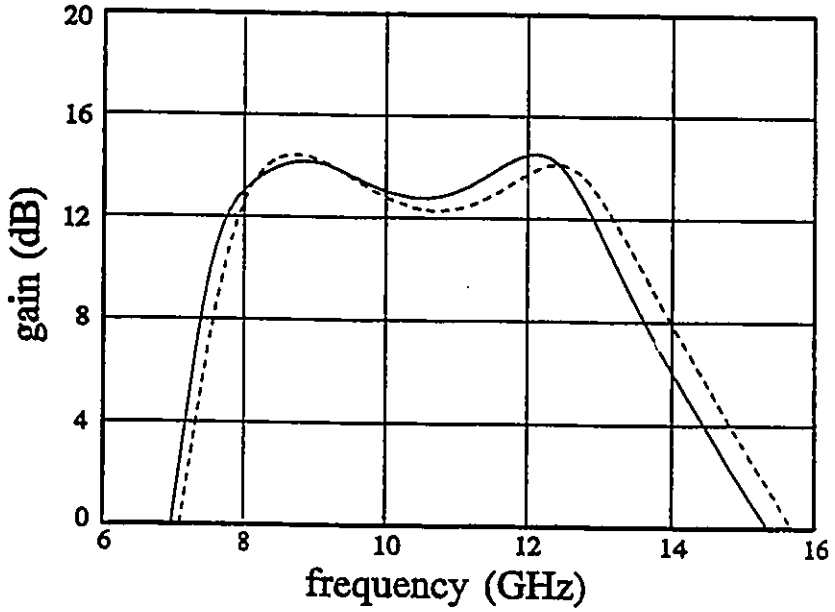

(a)

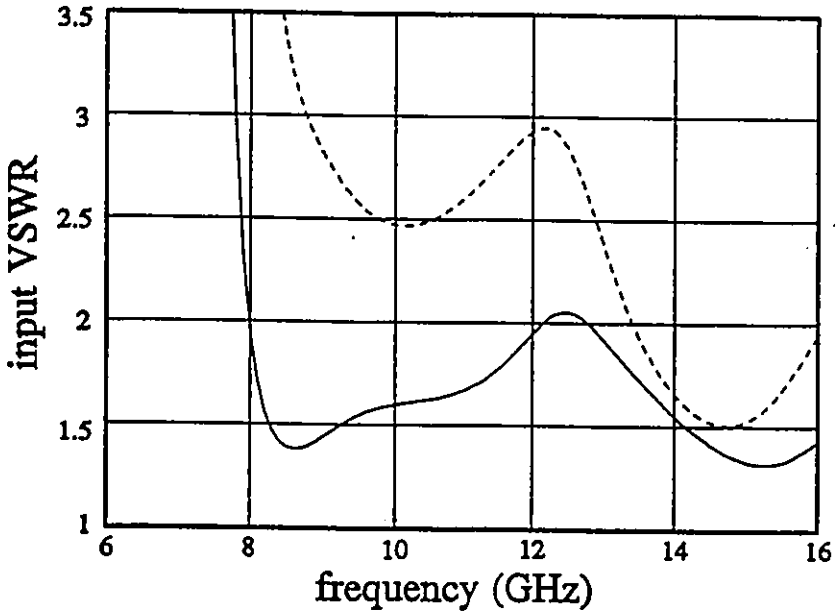

(b)

Fig. 6.6 (a) Gain and (b) input VSWR versus frequency before (---) and after (——) nominal design optimization.

TABLE 6.2

PARAMETER VALUES FOR THE PASSIVE ELEMENTS USED IN NOMINAL DESIGN

Parameter	Before Optimization	After Optimization
$S_{C1}(\mu m^2)$	353.1	326.8
$S_{C2}(\mu m^2)$	2014.4	2022.4
$S_{C3}(\mu m^2)$	212.3	218.2
$S_{C4}(\mu m^2)$	354.2	352.2
$S_{Cg}^*(\mu m^2)$	8078	8078
$S_{Cd}^*(\mu m^2)$	24235	24235
$d^*(\mu m)$	0.1	0.1
$w_L^*(\mu m)$	20	20
$s_L^*(\mu m)$	10	10
n_{L1}	3.06	2.78
n_{L2}	3.56	3.66
n_{L3}	2.84	2.96
n_{L4}	3.68	3.63
n_{L5}	2.13	2.17
n_{L6}	2.61	2.58
n_{L7}	2.42	2.62
n_{L8}	2.45	2.43
n_{L9}	2.88	2.78
n_{L10}	3.09	3.01
$r_s^*(\Omega/\square)$	400	400
$w_R^*(\mu m)$	20	20
$l_R^*(\mu m)$	75	75
$h^*(\mu m)$	200	200

S_{Ci} is the metal plate area of the MIM capacitors C_i, $i = 1, 2, 3, 4$. S_{Cg} (S_{Cd}) is the metal area for the capacitors C_{g1}, C_{g2} and C_{g3} (C_{d1}, C_{d2} and C_{d3}). d is the thickness of the dielectric film for all MIM capacitors. n_{Li} is the number of turns of the spiral inductor L_i, $i = 1, 2, ..., 10$. w_L and s_L are, respectively, the conductor width and spacing for all spiral inductors. r_s, w_R and l_R are, respectively, the sheet resistance, width and length of the resistive film for the two bias resistors R_1 and R_2. h is the substrate thickness. Those parameters marked with * are fixed during optimization.

TABLE 6.3

ASSUMED DISTRIBUTIONS FOR STATISTICAL VARIABLES

Statistical Variable	Mean Value	Standard Deviation (%)
$L(\mu m)$	1.0	3.5
$a(\mu m)$	0.3	3.5
$W(\mu m)$	300	2.0
$N_d(1/m^3)$	1.0×10^{23}	7.0
$w_L(\mu m)$	20	3.0
$s_L(\mu m)$	10	3.0
$d(\mu m)$	0.1	4.0
$S_{C1}(\mu m^2)$	326.8	3.5
$S_{C2}(\mu m^2)$	2022.4	3.5
$S_{C3}(\mu m^2)$	218.2	3.5
$S_{C4}(\mu m^2)$	352.2	3.5

The gate length L, channel thickness a, gate width W and doping density N_d of the three MESFETs have the same distribution. The conductor width w_L and spacing s_L of the 10 spiral inductors $L_1, L_2, ..., L_{10}$ have the same distribution. d is the thickness of the dielectric film for all MIM capacitors. S_{Ci} is the area of the metal plate of MIM capacitor C_i.

TABLE 6.4

ASSUMED PARAMETER CORRELATIONS FOR THE THREE MESFETS

	a_{F1}	L_{F1}	W_{F1}	N_{dF1}	a_{F2}	L_{F2}	W_{F2}	N_{dF2}	a_{F3}	L_{F3}	W_{F3}	N_{dF3}
a_{F1}	1.00	0.00	0.00	-0.25	0.80	0.00	0.00	-0.20	0.78	0.00	0.00	-0.10
L_{F1}	0.00	1.00	0.00	-0.10	0.00	0.80	0.00	-0.05	0.00	0.78	0.00	-0.05
W_{F1}	0.00	0.00	1.00	0.00	0.00	0.00	0.80	0.00	0.00	0.00	0.78	0.00
N_{dF1}	-0.25	-0.10	0.00	1.00	-0.20	-0.05	0.00	0.80	-0.15	-0.05	0.00	0.78
a_{F2}	0.80	0.00	0.00	-0.20	1.00	0.00	0.00	-0.25	0.80	0.00	0.00	-0.20
L_{F2}	0.00	0.80	0.00	-0.05	0.00	1.00	0.00	-0.10	0.00	0.80	0.00	-0.10
W_{F2}	0.00	0.00	0.80	0.00	0.00	0.00	1.00	0.00	0.00	0.00	0.80	0.00
N_{dF2}	-0.20	-0.05	0.00	0.80	-0.25	-0.10	0.00	1.00	-0.20	-0.05	0.00	0.80
a_{F3}	0.78	0.00	0.00	-0.15	0.80	0.00	0.00	-0.20	1.00	0.00	0.00	-0.25
L_{F3}	0.00	0.78	0.00	-0.05	0.00	0.80	0.00	-0.05	0.00	1.00	0.00	-0.10
W_{F3}	0.00	0.00	0.78	0.00	0.00	0.00	0.80	0.00	0.00	0.00	1.00	0.00
N_{dF3}	-0.10	-0.05	0.00	0.78	-0.20	-0.10	0.00	0.80	-0.25	-0.10	0.00	1.00

The subscripts $F1$, $F2$ and $F3$ are used to distinguish the parameters of three different FETs.

At the starting point (i.e., the minimax nominal design), the yield was 26% as estimated by Monte Carlo analysis with 200 statistical outcomes. The yield was improved to 69% at the solution of yield optimization (about 4 and a half hours CPU time on a Sun SPARCstation 1). The solution is given in Table 6.5. The Monte Carlo sweeps of gain and input VSWR before and after yield optimization are shown in Figs. 6.7 and 6.8.

6.5 PREDICTABLE YIELD-DRIVEN CIRCUIT DESIGN

In this section, we present a comprehensive approach to *predictable* yield optimization of microwave circuits exploiting an analytical statistical model. A novel small-signal statistical GaAs MESFET PBM (KTL) integrates the Khatibzadeh and Trew model for DC simulation with the Ladbrooke formulas for small-signal analysis. Accuracy of the statistical KTL model is demonstrated by good agreement between Monte Carlo simulations using the model and corresponding simulations using device measurement data. Predicted yield over a range of specifications is verified by device data. The benefits of simultaneous circuit-device yield optimization assisted by yield sensitivity analysis are also demonstrated.

6.5.1 A New Statistical GaAs MESFET Model

In Chapter 5 we reported that the Ladbrooke model [78] has attractive statistical properties for small-signal application but the operating point needs to be determined separately. On the other hand, the Khatibzadeh and Trew model [76], though suitable for DC and large-signal applications (e.g., Khatibzadeh and Trew

TABLE 6.5

DESIGN VARIABLES FOR YIELD OPTIMIZATION

Parameter	Before Optimization	After Optimization
$L(\mu m)$	1.0	0.99
$a(\mu m)$	0.3	0.31
$W(\mu m)$	300	308
$N_d(1/m^3)$	1.0×10^{23}	1.03×10^{23}
$S_{C1}(\mu m^2)$	326.8	322.7
$S_{C2}(\mu m^2)$	2022.4	2006.3
$S_{C3}(\mu m^2)$	218.2	222.9
$S_{C4}(\mu m^2)$	352.2	356.7
n_{L1}	2.78	2.74
n_{L2}	3.66	3.66
n_{L3}	2.96	3.03
n_{L4}	3.63	3.65
n_{L5}	2.17	2.23
n_{L6}	2.58	2.51
n_{L7}	2.62	2.62
n_{L8}	2.43	2.44
n_{L9}	2.78	2.78
n_{L10}	3.01	3.09

All other parameters are fixed at the same values as listed in Table 6.1 and Table 6.2.

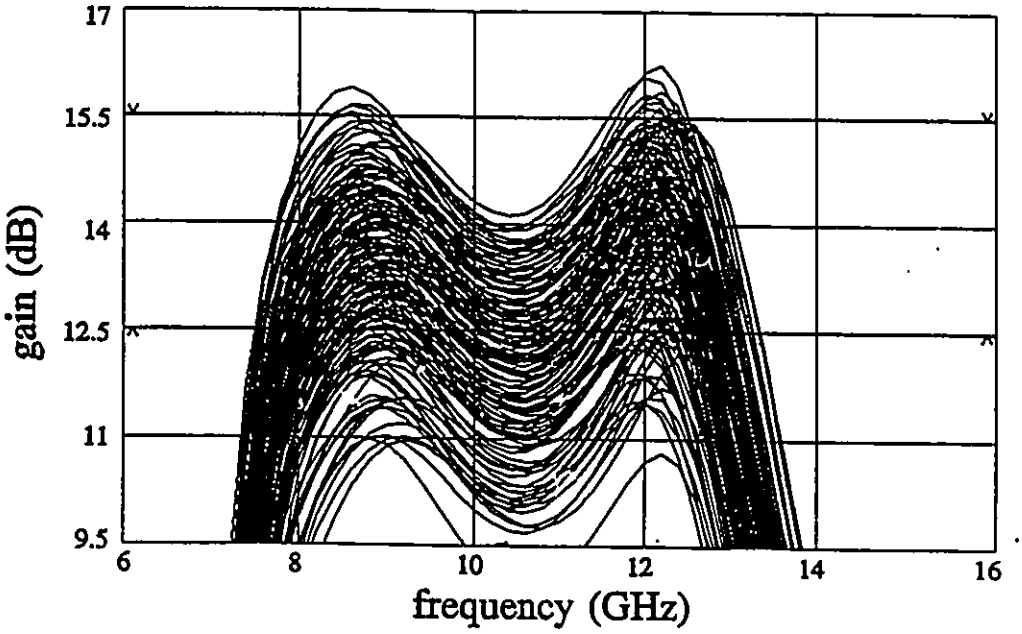

(a)

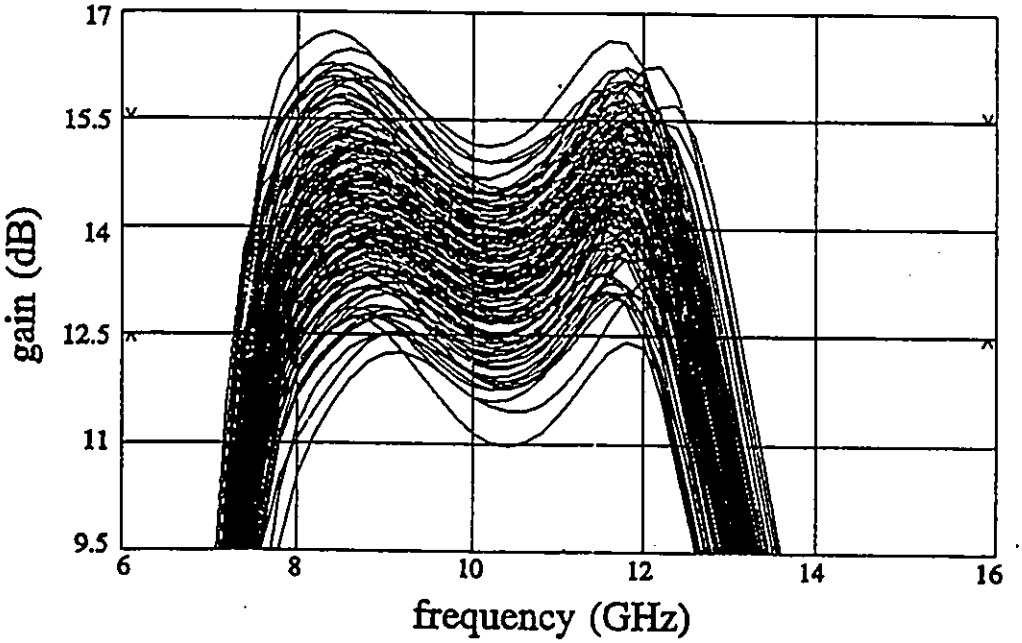

(b)

Fig. 6.7 Monte Carlo sweep of gain versus frequency (a) before and (b) after yield optimization.

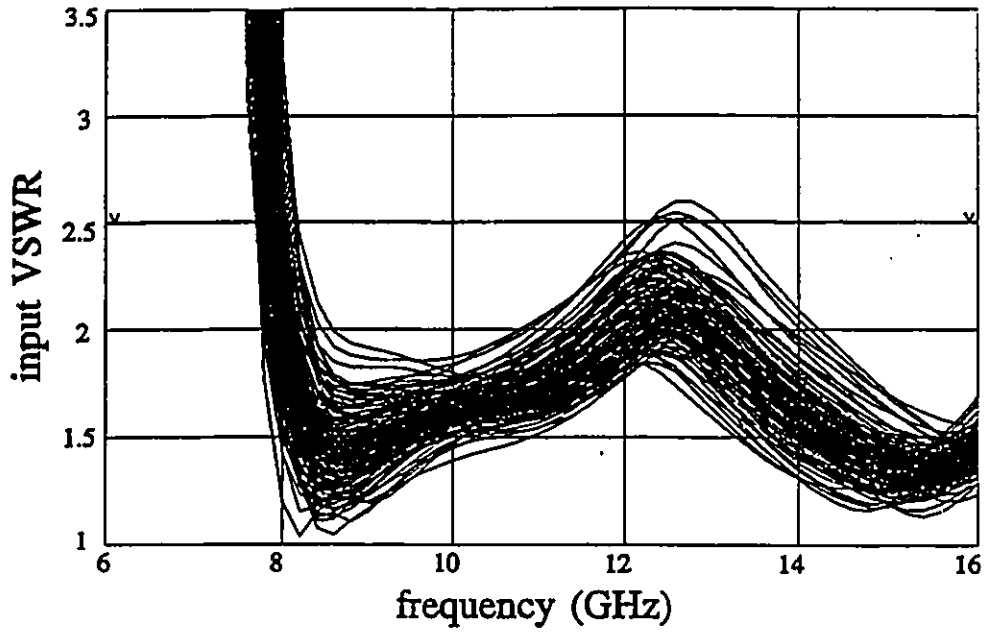

(a)

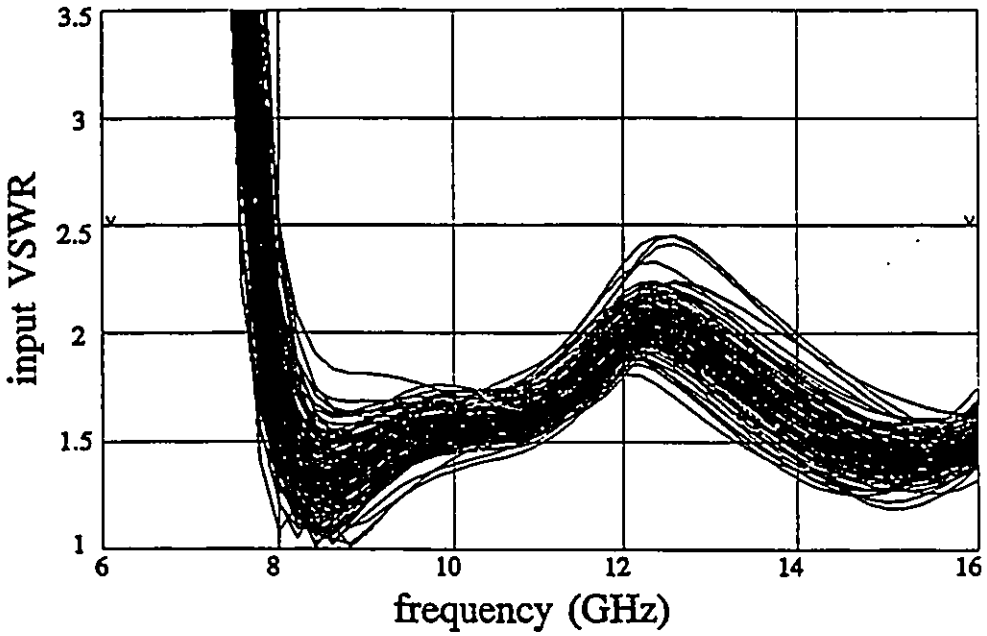

(b)

Fig. 6.8 Monte Carlo sweep of input VSWR versus frequency (a) before and (b) after yield optimization.

(1988) [76], Bandler, Zhang and Cai (1990) [23], and Stoneking, Bilbro, Gilmore, Trew and Kelly (1992) [125]), seems to be not as accurate as the Ladbrooke model for small-signal applications, in particular for statistical modeling.

To overcome the shortcomings of each model and provide for complete DC/small-signal device simulations we combine the Ladbrooke model with the Khatibzadeh and Trew model. The latter is employed to solve for the DC operating point needed in establishing the former. Both models share the same physical parameters, therefore the resulting combined, or integrated, model is consistently defined. The statistical KTL model is then obtained by extracting the statistics of the model parameters from multi-device measurement data.

The KTL small-signal equivalent circuit follows the Ladbrooke model and is shown in Fig. 6.9 which is the same as Fig. 5.9 except that two capacitors C_{ge} and C_{de} are added to the extrinsic circuits. The model includes the intrinsic FET parameters

$$\{L, W, a, N_d, V_{b0}, v_s, E_c, \mu_0, \varepsilon, L_{g0}, a_0, r_{01}, r_{02}, r_{03}\}$$

and the linear extrinsic elements

$$\{L_g, R_g, L_d, R_d, L_s, R_s, G_{ds}, C_x, C_{ds}, C_{ge}, C_{de}\}$$

where L is the gate length, W the gate width, a the channel thickness, N_d the doping density, V_{b0} the zero-bias barrier potential, v_s the saturation value of electron drift velocity, E_c the critical electric field, μ_0 the low-field mobility of GaAs, ε the permittivity of GaAs, L_{g0} the inductance from gate bond wires and pads, a_0 the proportionality coefficient, and r_{01}, r_{02} and r_{03} are fitting coefficients as indicated in Section 5.5.2.

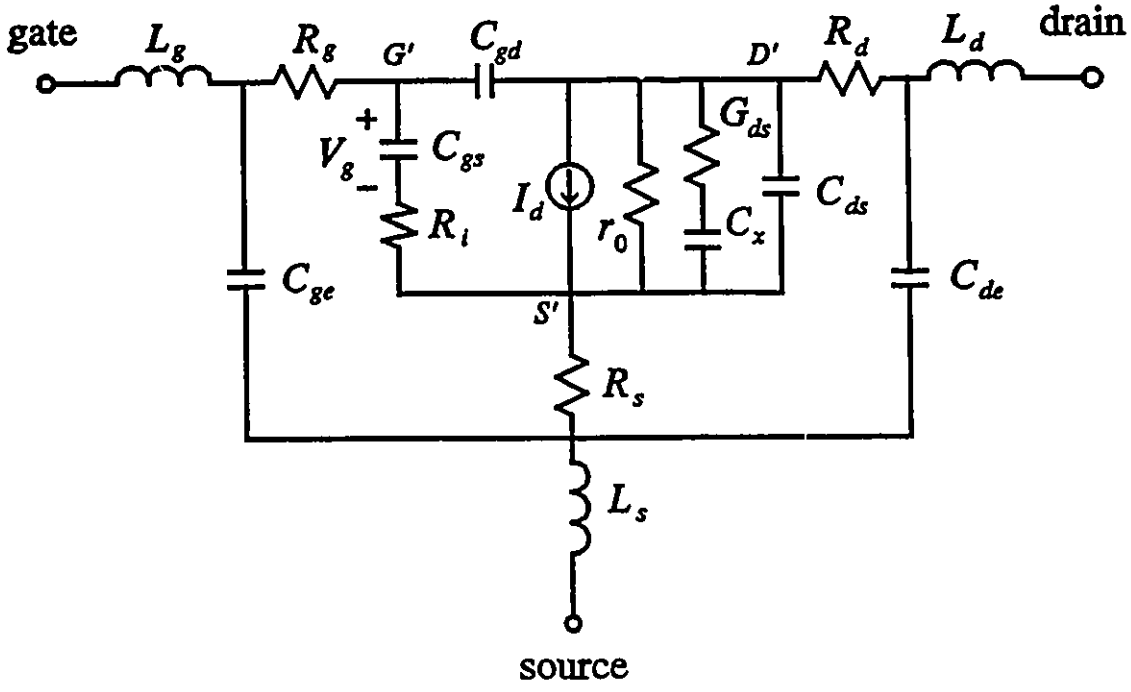

Fig. 6.9 Small-signal equivalent circuit where $I_d=g_m V_g e^{-j\omega\tau}$.

The bias-dependent small-signal parameters, namely, g_m, C_{gs}, C_{gd}, R_i, L_g, r_0 and τ, as shown in Fig. 6.9, are derived using the same formulas as those described in Section 5.5.2.

Following our approach to statistical modeling presented in Chapter 5, device statistics are represented by a multidimensional normal distribution characterized by the means, standard deviations and the correlation matrix, with additional one-dimensional mapping employing discrete distribution functions (DDFs) for the marginal distributions.

6.5.2 Measurement Data Interpolation

In Chapter 5 we reported statistical modeling from a sample of GaAs MESFET measurements from Plessey Research Caswell [140]. 69 individual devices (data sets) from two wafers were used. Each device represents a four finger 0.5μm gate length GaAs MESFET with equal finger width of 75μm. Each data set contains small-signal S parameters measured at frequencies from 1GHz to 21GHz with 0.4GHz step and under three different bias conditions (V_{DS} at 5V and V_{GS} approximately at 0V, -0.7V and -1.4V, respectively). DC drain bias currents are also included in the measurements.

The measurement bias conditions vary slightly from device to device, thus we align the different data sets to provide consistent bias points for statistical modeling. It is also desirable to interpolate measured data at some other bias points. The Materka and Kacprzak model is a suitable interpolator for this purpose, because of its excellent single device fitting accuracy for these devices. For each individual device

we fit the Materka and Kacprzak model to its corresponding data set. The resulting models are used to interpolate data for each device at two bias points (gate bias -0.5V and -0.7V, drain bias 5V). In this way we generated data sets for 69 devices including DC responses and *S* parameters from 1GHz to 21GHz with 2GHz step under the two bias conditions.

6.5.3 Statistical Modeling and Verification

After alignment of the measurement data described in the preceding section, we use the statistical modeling approach discussed in Chapter 5 to create the statistical KTL model. The parameters were extracted for each device by fitting the model responses to the corresponding *S*-parameter data and DC drain bias currents at gate bias -0.5V and -0.7V and drain bias 5V. The 69 (deterministic) models corresponding to the 69 measured devices were then postprocessed to obtain the parameter statistics including mean values, standard deviations and parameter correlations. The resulting mean values and the standard deviations are listed in Table 6.6. The parameter correlations are listed in Table 6.7. Histograms of channel thickness and doping density are shown in Fig. 6.10.

It should be pointed out that parameter statistics of the KTL model are different from those of the Ladbrooke model reported in Chapter 5. This can be easily seen by comparing Table 5.5 with Table 6.6 and Fig. 5.10-11 with Fig. 6.10. The causes of such discrepancies are not clear and require further investigation.

For verification, 400 Monte Carlo outcomes were generated using the statistical KTL model. The statistics of the simulated *S* parameters for those 400

TABLE 6.6

MESFET MODEL PARAMETERS

Parameter	Mean	Std. Dev. (%)
$L(\mu m)$	0.4997	4.76
$a(\mu m)$	0.1630	5.78
$N_d(m^{-3})$	2.475×10^{23}	4.21
$V_{bi}(V)$	0.2661	34.6
$L_{G0}(nH)$	0.0299	9.02
$r_{01}(\Omega/V^2)$	0.0779	0.17
$r_{02}(V)$	7.7855	0.17
$r_{03}(\Omega)$	534.44	4.86
$R_d(\Omega)$	0.4905	1.42
$R_s(\Omega)$	3.9345	1.29
$R_g(\Omega)$	7.7811	0.34
$L_d(nH)$	6.21×10^{-2}	5.88
$L_s(nH)$	2.15×10^{-2}	7.31
$G_{ds}(1/\Omega)$	2.34×10^{-3}	4.19
$C_{ds}(pF)$	5.89×10^{-2}	2.33
$C_{ge}(pF)$	4.61×10^{-2}	6.12
$C_{de}(pF)$	2.00×10^{-4}	0.05
$W(\mu m)$	300	*
$v_s(m/s)$	9.5×10^{4}	*
$E_c(V/m)$	1.9×10^{5}	*
$\mu_0(m^2/Vs)$	0.5	*
ϵ	12.5	*
a_0	1.0	*

* Assumed fixed (non-statistical) parameters.

TABLE 6.7

STATISTICAL PARAMETER CORRELATIONS FOR THE KTL MODEL

	L	a	N_d	V_{bi0}	L_{G0}	r_{01}	r_{02}	r_{03}	R_g	R_d	L_d	R_s	L_s	G_{ds}	C_{ds}	C_{gs}	C_{dc}
L	1	0.6966	-0.1201	0.8042	-0.0059	-0.2517	0.6122	-0.2624	-0.1574	-0.2693	-0.3454	0.3461	0.1445	-0.6601	-0.4498	-0.1819	-0.1685
a	0.6966	1	-0.1725	0.3959	-0.3875	-0.7307	0.1765	-0.7345	-0.3326	-0.4907	-0.4157	0.8426	0.0643	-0.2165	-0.1811	-0.3183	-0.7354
N_d	-0.1201	-0.1725	1	-0.1764	0.5367	0.4261	0.0018	0.4319	-0.4629	-0.2328	0.7533	-0.4202	0.6395	0.2471	-0.6034	-0.2645	0.0611
V_{bi0}	0.8042	0.3959	-0.1764	1	-0.0123	-0.1157	0.5011	-0.1254	-0.1243	-0.1831	-0.2690	0.0895	0.2515	-0.4987	-0.3632	-0.1009	0.0644
L_{G0}	-0.0059	-0.3875	0.5367	-0.0123	1	0.5943	-0.0304	0.5932	0.2392	0.3048	0.7160	-0.5648	0.4985	-0.0055	-0.5225	-0.4108	0.5212
r_{01}	-0.2517	-0.7307	0.4261	-0.1157	0.5943	1	0.0515	0.9998	0.3857	0.5587	0.4765	-0.7618	0.1455	-0.0374	-0.1893	-0.0102	0.7088
r_{02}	0.6122	0.1765	0.0018	0.5011	-0.0304	0.0515	1	0.0389	-0.3423	-0.3456	-0.3523	-0.2191	0.0462	-0.9102	-0.3862	0.4628	0.2075
r_{03}	-0.2624	-0.7345	0.4319	-0.1254	0.5932	0.9998	0.0389	1	0.3825	0.5574	0.4835	-0.7617	0.1463	-0.0226	-0.1854	-0.0119	0.7055
R_g	-0.1574	-0.3326	-0.4629	-0.1243	0.2392	0.3857	-0.3423	0.3825	1	0.8610	-0.0682	-0.0323	-0.4047	0.0007	0.4020	-0.2838	0.4192
R_d	-0.2693	-0.4907	-0.2328	-0.1831	0.3048	0.5587	-0.3456	0.5574	0.8610	1	0.2653	-0.2514	-0.1452	0.1184	0.1761	-0.1742	0.4925
L_d	-0.3454	-0.4157	0.7533	-0.2690	0.7160	0.4765	-0.3523	0.4835	-0.0682	0.2653	1	-0.4980	0.6915	0.4841	-0.5033	-0.3559	0.2359
R_s	0.3461	0.8426	-0.4202	0.0895	-0.5648	-0.7618	-0.2191	-0.7617	-0.0323	-0.2514	-0.4980	1	-0.1882	0.0723	0.2473	-0.3779	-0.7979
L_s	0.1445	0.0643	0.6395	0.2515	0.4985	0.1455	0.0462	0.1463	-0.4047	-0.1452	0.6915	-0.1882	1	0.1363	-0.7723	-0.4043	-0.0783
G_{ds}	-0.6601	-0.2165	0.2471	-0.4987	-0.0055	-0.0374	-0.9102	-0.0226	0.0007	0.1184	0.4841	0.0722	0.1363	1	0.2189	0.3123	-0.2506
C_{ds}	-0.4498	-0.1811	-0.6034	-0.3632	-0.5225	-0.1893	-0.3862	-0.1854	0.4020	0.1761	-0.5033	0.2473	-0.7723	0.2189	1	0.2238	-0.0054
C_{gs}	-0.1819	-0.3183	-0.2645	-0.1009	-0.4108	-0.0102	0.4628	-0.0119	-0.2838	-0.1742	-0.3559	-0.3779	-0.4043	-0.3123	0.2238	1	0.2293
C_{dc}	-0.1685	-0.7354	0.0611	0.0644	0.5212	0.7088	0.2075	0.7055	0.4192	0.4925	0.2359	-0.7979	-0.0783	-0.2506	-0.0054	0.2293	1

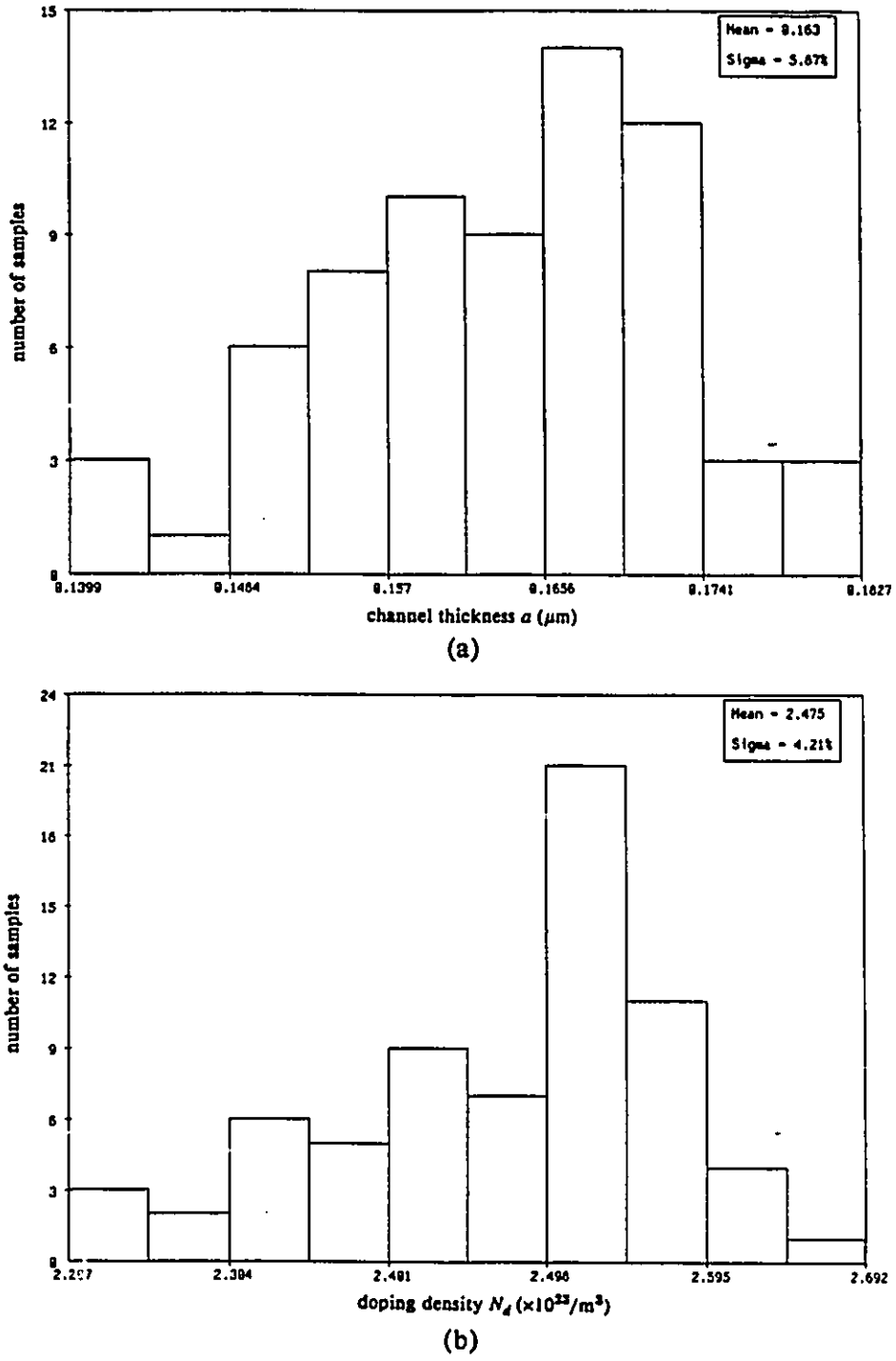

Fig. 6.10 Histograms of (a) channel thickness a and (b) doping density N_d obtained from statistical postprocessing of extracted parameters.

outcomes were compared with the statistics of the data. The mean values and standard deviations from the data and the simulated S parameters at both bias points and at frequency 11GHz are listed in Table 6.8. Note that the statistics of the data and simulated S parameters are consistent. This validates the statistical properties of KTL.

Statistical verification of the models is of utmost importance. Virtually every paper on statistical modeling tries to address it. While first and second order statistical moments are frequently considered inadequate (e.g., Purviance, Meehan and Collins (1990) [98]), full verification of joint probability density functions may not be feasible. A further verification may required. This is discussed in the next section.

6.5.4 Yield Optimization and Verification

We consider the small-signal broadband amplifier shown in Fig. 6.11. The specifications for yield optimization are: $|S_{21}| = 8\text{dB} \pm 0.5\text{dB}$, $|S_{11}| < 0.5$ and $|S_{22}| < 0.5$ for the frequency range 8GHz-12GHz. The matching network elements, namely, L_1, L_2, L_3, L_4, L_5, L_6, C_1, C_2, C_3, C_4 and R, are chosen as design variables. They are also assigned random variations of uniform distribution with a 5% tolerance. Adding these to the FET parameters, we have a total of 28 statistical variables. The optimization was carried out using OSA90/hope [139] on a Sun SPARCstation 1.

First, a nominal minimax design was obtained (after 133 iterations and about 12 minutes CPU time). The yield of the nominal design is estimated as 17.5% by Monte Carlo simulation with 200 outcomes. Using the nominal design as the starting point, yield optimization was performed with 100 outcomes. After 30 iterations (145 minutes CPU time), the yield was increased to 67% as estimated by Monte Carlo

TABLE 6.8

MEAN VALUES AND STANDARD DEVIATIONS OF DATA AND SIMULATED S PARAMETERS AT 11GHZ

	Bias 1				Bias 2			
	Data		KTL		Data		KTL	
	Mean	Dev.(%)	Mean	Dev.(%)	Mean	Dev.(%)	Mean	Dev.(%)
$\lvert S_{11} \rvert$	0.771	0.67	0.765	0.74	0.775	0.65	0.776	0.72
$\angle S_{11}$	-103.5	1.53	-104.2	1.62	-100.1	1.60	-100.5	1.54
$\lvert S_{21} \rvert$	1.760	2.26	1.707	2.84	1.657	3.23	1.668	2.78
$\angle S_{21}$	97.21	0.72	98.26	0.84	98.10	0.70	100.3	0.73
$\lvert S_{12} \rvert$	0.091	4.10	0.092	4.32	0.097	4.27	0.097	3.85
$\angle S_{12}$	35.59	1.74	35.04	2.13	36.20	1.63	35.45	2.12
$\lvert S_{22} \rvert$	0.576	1.57	0.577	1.66	0.577	1.78	0.579	1.66
$\angle S_{22}$	-39.48	1.42	-39.61	1.37	-39.96	1.26	-40.18	1.24

Bias 1: V_{GS} = -0.5V, V_{DS} = 5V.
Bias 2: V_{GS} = -0.7V, V_{DS} = 5V.

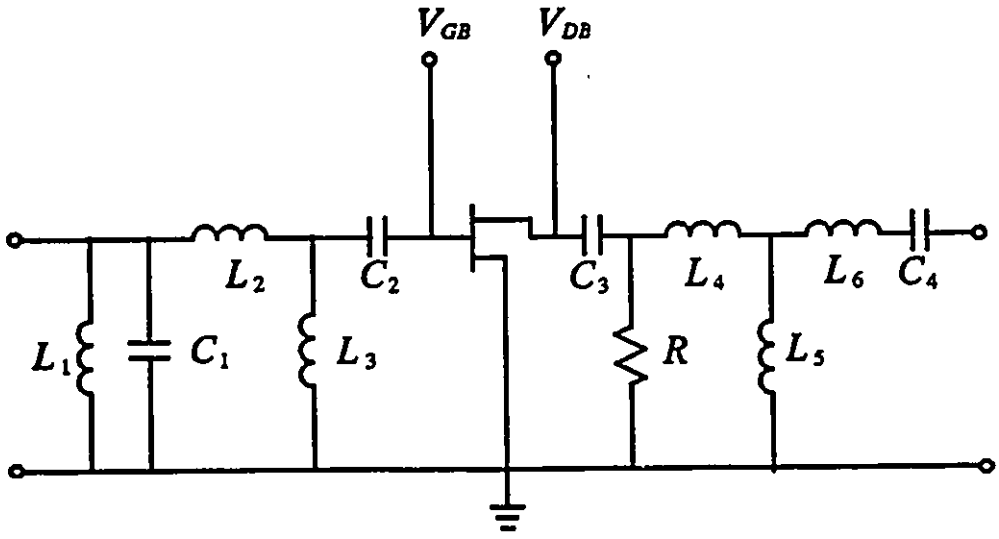

Fig. 6.11 Small-signal broadband amplifier [27].

simulation with 200 outcomes.

Table 6.9 lists the values of the design variables before and after yield optimization. The Monte Carlo sweeps of $|S_{21}|$ before and after yield optimization are shown in Fig. 6.12.

The significance of yield optimization will be much more convincing if the yield predicted by statistical models can be shown to be consistent with actual device data. To demonstrate that this indeed can be the case, we substitute the KTL model with device data and compare the Monte Carlo yields for both cases. Because the wafer measurements contain small variations in bias conditions between different devices, we use the Materka and Kacprzak model to interpolate individual device data at the same bias point (V_{GB} = -0.7V and V_{DB} = 5V), as discussed in Section 6.5.2.

The yield predicted by Monte Carlo simulation using the device data and 140 outcomes was 15.7% (nominal design) and 57.9% (after yield optimization). This verifies very well the yields predicted by KTL model (which are 17.5% and 67%, respectively). The Monte Carlo sweeps of $|S_{21}|$ using the device data are shown in Fig. 6.13, which are in excellent agreement with those produced by the statistical model (Fig. 6.12).

To show that the good result is not a singular exception, we varied the design specifications over a range and applied the same procedure. As shown in Table 6.10, the yields predicted by the model and the device data are in very good agreement in all cases.

We feel that the procedure outlined in this section is suitable for statistical validation of the KTL model. Yield, similarly to mean value or standard deviation,

TABLE 6.9

MATCHING CIRCUIT OPTIMIZATION

Design Variable	Before Yield Optimization	After Yield Optimization
C_1(pF)	0.6161	0.4372
C_2(pF)	5.2556	6.1365
C_3(pF)	0.2606	0.2757
C_4(pF)	0.1385	0.1570
$R(\Omega)$	589.00	708.08
L_1(nH)	0.5947	0.9110
L_2(nH)	0.9916	0.9430
L_3(nH)	1.9203	1.6395
L_4(nH)	1.5754	1.7516
L_5(nH)	2.0039	2.3933
L_6(nH)	1.0085	0.7537

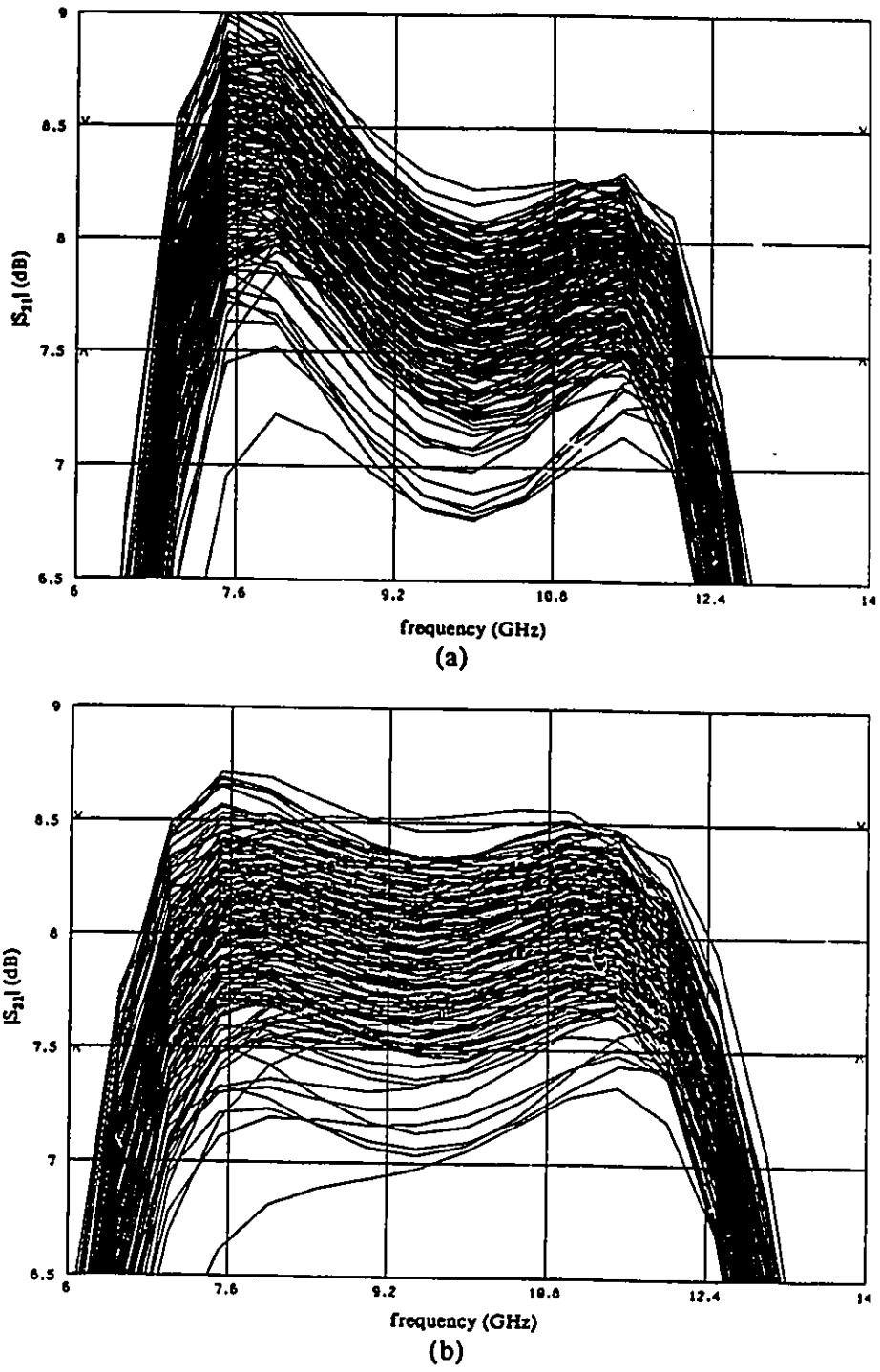

Fig. 6.12 Monte Carlo sweeps of $|S_{21}|$ using the statistical KTL model, (a) before yield optimization and (b) after yield optimization.

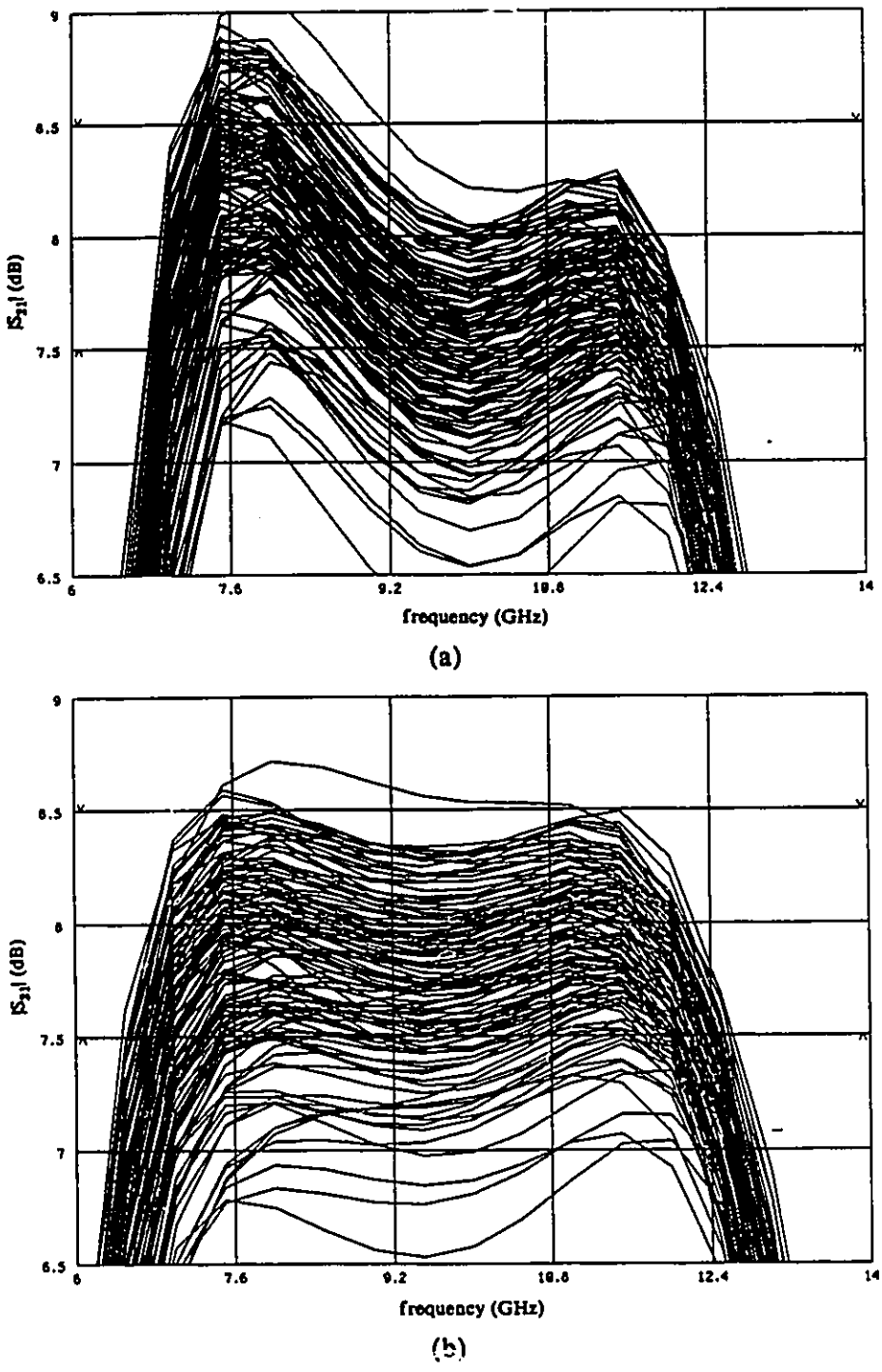

Fig. 6.13 Monte Carlo sweeps of $|S_{21}|$ using device data (140 outcomes), (a) before yield optimization and (b) after yield optimization.

TABLE 6.10

YIELD PREDICTED BY MODEL AND VERIFIED BY DATA

Specification	Before Yield Optimization		After Yield Optimization	
	KTL Predicted Yield (%)	Data Verified Yield (%)	KTL Predicted Yield (%)	Data Verified Yield (%)
Spec. 1	17.5	15.7	67	57.9
Spec. 2	21	20	83	75.7
Spec. 3	44	37.1	98	93.6

Spec. 1: $7.5\text{dB} < |S_{21}| < 8.5\text{dB}$, $|S_{11}| < 0.5$, $|S_{22}| < 0.5$.
Spec. 2: $6.5\text{dB} < |S_{21}| < 7.5\text{dB}$, $|S_{11}| < 0.5$, $|S_{22}| < 0.5$.
Spec. 3: $6.0\text{dB} < |S_{21}| < 8.0\text{dB}$, $|S_{11}| < 0.5$, $|S_{22}| < 0.5$.

200 outcomes are used for yield prediction by the statistical KTL model, 140 for yield verification using the device data.

can be considered as a statistical parameter, whose estimate is determined from a sample. It is better qualified to validate the model for the simple reason that yield estimation is what the model is intended for.

6.5.5 Yield Sensitivity Analysis

Yield is a function of device parameters, circuit elements, parameter statistics and design specification. To select a proper set of variables for yield optimization can be a delicate task. We use OSA90/hope to calculate the sensitivities of yield w.r.t. circuit and design parameters. This analysis reveals the influence of different parameters on yield, and this information can assist us in selecting variables for yield optimization.

We performed yield sensitivity analysis w.r.t. two parameters which were not included in the optimization of the matching network, namely, one design specification and one device parameter (the FET gate length).

Fig. 6.14 depicts the yield sensitivity w.r.t. the lower specification on the gain (the upper specification was fixed). It shows, for instance, that if the lower specification is relaxed from 7.5dB to 7.3dB, the yield would increase from 67% to 74.5%. Fig. 6.15 depicts the yield sensitivity w.r.t. the FET gate length. It clearly shows that the gate length has a strong influence on yield and therefore merits inclusion as a variable for yield optimization.

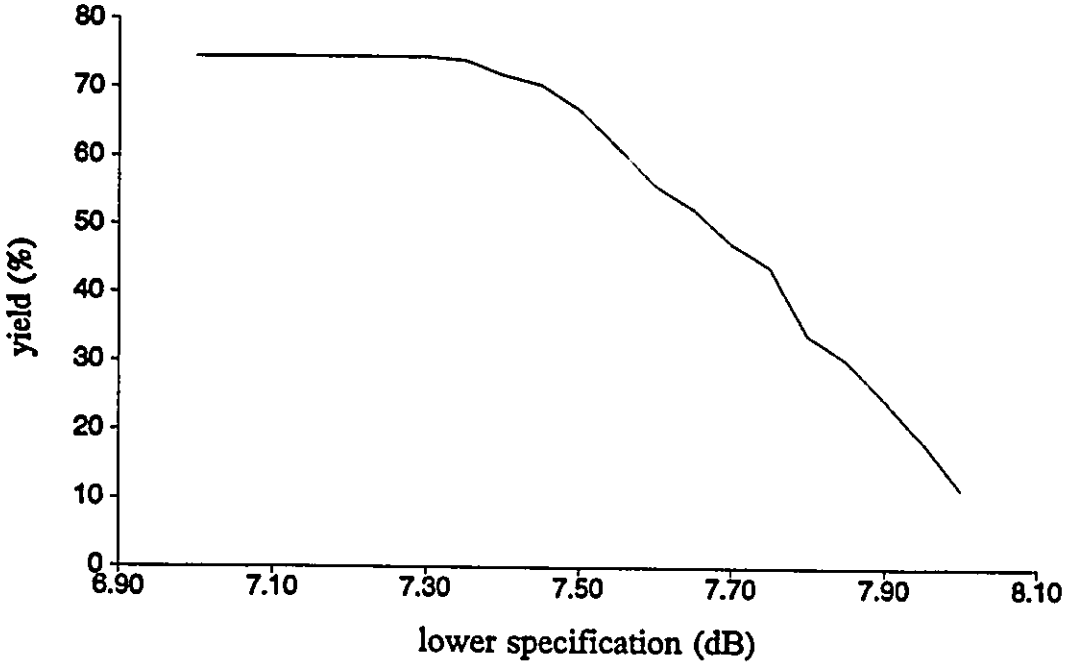

Fig. 6.14 Yield versus the lower specification on the gain.

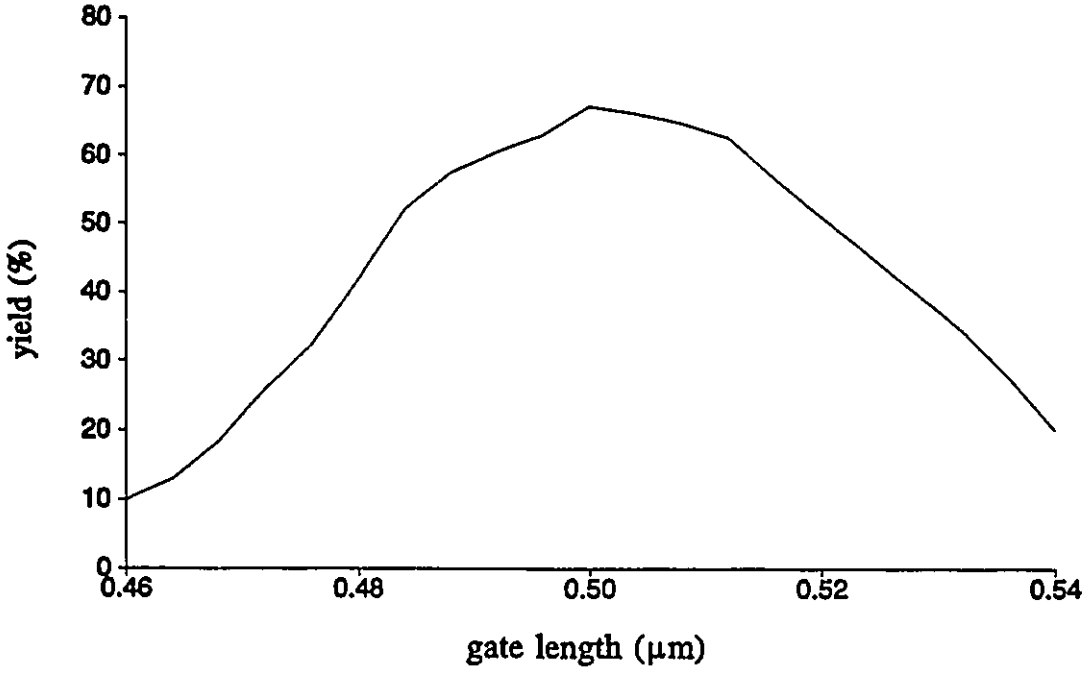

Fig. 6.15 Yield versus the FET gate length.

6.5.6 Simultaneous Device-Circuit Design

Representing devices by statistical PBMs has a clear advantage over direct use of the measured S parameters: the model can interpolate device behaviour at frequency and bias points not contained in the data, and an unlimited number of outcomes can be generated for Monte Carlo analysis. Also, the use of PBMs presents us with the opportunity of optimizing the parameters of active devices, which is not possible if the devices are represented by S parameters. Although device optimization can be expensive to implement, it may be justified when stringent specifications result in very low yield which cannot be sufficiently improved by optimizing the matching circuit alone.

Consider again the small-signal broadband amplifier. We tighten the upper specification on $|S_{11}|$ from 0.5 to 0.4 in the passband, while the other specifications remain the same. Two separate cases of optimization were constructed as follows. In Case I, only the matching circuits are optimized. In Case II, we include the GaAs MESFET gate length and channel thickness as design variables in addition to the matching circuits.

In both cases, we first performed a minimax nominal optimization and then a yield optimization. In Case I, at the nominal solution the yield predicted by Monte Carlo simulation using 200 outcomes is only 7.5%. After yield optimization the yield is improved to 27.5%.

In Case II, the yield at the nominal solution is 12.5%, and is increased to 64.5% after yield optimization. Compared with Case I, this drastic improvement in the optimized yield requires relatively small changes in the device parameters: the gate

length changed from 0.5μm to 0.4μm and the channel thickness from 0.163μm to 0.14μm.

6.6 CONCLUSIONS

Yield-driven circuit design has been addressed in this chapter. We have presented various stages of yield-driven CAD: statistical modeling, nominal design optimization, yield optimization, yield verification and device optimization.

FAST gradient-based yield optimization using the one-sided ℓ_1 algorithm with a generalized ℓ_p function has been discussed.

We have demonstrated yield optimization of MMICs using PBMs for both active and passive devices. Significant increase of yield is obtained after yield optimization for a three stage X-band MMIC amplifier.

Predictable yield-driven circuit optimization employing statistical KTL model has been addressed. We have presented the statistical KTL model: a novel, accurate physics-oriented model for GaAs MESFETs, particularly suitable for statistical device characterization. Using the statistical KTL model to design a broadband small-signal amplifier, we have demonstrated for the first time that yield predicted by Monte Carlo simulation using an analytical PBM can be consistent with yield predicted directly from device measurement data. Excellent results have been obtained for a variety of design specifications.

Simultaneous device and circuit optimization assisted by yield sensitivity analyses further champions the relevance and benefits of our physics-based technique for MMICs. It will become more attractive with continuing advances in technology.

Chapter 7

CONCLUSIONS

This thesis has presented approaches towards physics-oriented microwave circuit optimization. We have addressed physics-based device modeling, parameter extraction, nonlinear simulation, nominal design, statistical modeling and yield optimization.

Analytical large-signal PBMs of MESFETs have been discussed and new developments presented in Chapter 2. Emphasis has been put on the Khatibzadeh and Trew model. A significant advantage of PBMs over ECMs is that the device responses can be predicted by PBM simulation directly from the physical parameters. This predictive potential of PBMs can be used to improve design capabilities. PBMs are particularly suitable for MMIC analysis and design since PBMs provide flexibility for engineers to perform designs based on physical parameters and to foresee the characteristics of the circuits before fabrication.

Nonlinear circuit analysis with PBMs integrated into the HB equation has been described in Chapter 3. The formulation of the HB equation and the calculation of its Jacobian matrix has been illustrated. An efficient Newton method for solving the HB equation has been addressed. The accuracy of the HB simulation depends on the circuit nonlinearities and the number of harmonics used in the HB equation as well as the convergence properties of the algorithm used to solve the HB equation. Most

Chapter 7

CONCLUSIONS

This thesis has presented approaches towards physics-oriented microwave circuit optimization. We have addressed physics-based device modeling, parameter extraction, nonlinear simulation, nominal design, statistical modeling and yield optimization.

Analytical large-signal PBMs of MESFETs have been discussed and new developments presented in Chapter 2. Emphasis has been put on the Khatibzadeh and Trew model. A significant advantage of PBMs over ECMs is that the device responses can be predicted by PBM simulation directly from the physical parameters. This predictive potential of PBMs can be used to improve design capabilities. PBMs are particularly suitable for MMIC analysis and design since PBMs provide flexibility for engineers to perform designs based on physical parameters and to foresee the characteristics of the circuits before fabrication.

Nonlinear circuit analysis with PBMs integrated into the HB equation has been described in Chapter 3. The formulation of the HB equation and the calculation of its Jacobian matrix has been illustrated. An efficient Newton method for solving the HB equation has been addressed. The accuracy of the HB simulation depends on the circuit nonlinearities and the number of harmonics used in the HB equation as well as the convergence properties of the algorithm used to solve the HB equation. Most

nonlinear microwave circuits demonstrate weak nonlinearity and operate in the steady-state. Therefore, the HB technique has been considered as a very efficient method for nonlinear microwave circuit simulation.

Nonlinear circuit nominal design employing gradient-based optimization techniques with PBMs has been discussed in Chapter 4. FAST has been shown to be suitable for high speed gradient calculations for circuit optimization employing geometrical, material and process-related parameters of devices as design variables. Physics-based circuit optimization capable of directly optimizing the device physical parameters facilitates simultaneous device-circuit design. It gives engineers more freedom and possibilities. Design optimization using PBMs is becoming increasingly important in microwave CAD.

Statistical modeling of active devices has been presented in Chapter 5. ECM statistical modeling was reported with the Materka and Kacprzak model while PBM statistical modeling was illustrated through new implementations of the Khatibzadeh and Trew model and the Ladbrooke model. The statistical models obtained by parameter extraction and postprocessing are examined by comparing the results of Monte Carlo simulation to the measured data. The results show that statistical PBMs are more accurate than statistical ECMs. This indicates that PBMs are more suitable for statistical modeling though ECMs may provide better fit to the measurements for individual devices

We have seriously addressed yield-driven circuit design in Chapter 6. Formulation of yield optimization using the one-sided ℓ_1 technique with the generalized ℓ_p function has been discussed. FAST has been employed for gradient

calculation to allow efficient yield optimization. Physics-based statistical models have been applied in physics-based yield optimization suitable for MMICs. Both passive and active elements have been related through material and geometrical statistical parameters. Significant increase in yield has been achieved after yield optimization. We have presented predictable yield-driven circuit design using the statistical KTL model. From our experience, the statistical KTL model is the first analytical PBM to provide reliable and predictable results in yield optimization. For the first time, we have demonstrated that yield predicted by Monte Carlo simulation can be consistent with yield predicted directly from device measurement data. The advantages of our physics-based technique have been shown by simultaneous device-circuit yield optimization assisted by yield sensitivity analysis. Physics-based yield-driven design has been considered indispensable to MMIC design. We believe that it will become more and more attractive in the future.

From his experiences, the author feels that the following problems related to the topics in this thesis are worth further research and development.

1. For physics-based device modeling of MESFET as discussed in Chapter 2, almost all researchers working on this subject concentrate their attention on the intrinsic part of the device. The intrinsic model is derived in terms of physical parameters. However, the extrinsic part is modelled using ECM elements which are determined according to practical knowledge or by parameter extraction from measurements. In fact, the extrinsic model parameters are also functions of physical quantities and have considerable effect on the calculation of device

responses. Therefore, the extrinsic model should be also derived from physical parameters. By doing this, the device model will consist of only physical parameters and will be completely physics-based. Furthermore, a number of phenomena of the MESFET such as the dependence of low frequency anomalies on the surface and bulk traps and the dependence of the breakdown voltage on the surface coatings have not been accommodated by the present MESFET PBMs. Further investigation and improvement are required.

2. Physics-based nonlinear circuit analysis using the HB technique and PBMs has received great interest in microwave CAD. However, there are still a number of unsolved problems. For example, large-signal HB simulation sometimes faces the convergence problem. It is not quite clear whether the problem is due to model inaccuracy or the convergence problem of the algorithm used to solve the HB equation. Further investigation is needed.

3. Statistical PBMs have been addressed with the Khatibzadeh and Trew model and the Ladbrooke model (see Chapter 5) as well as the KTL model (see Chapter 6). Their attractive statistical properties have been reported. However, there are some observations which are not clear. For example, we observed that the statistical Ladbrooke model and the statistical KTL model showed different statistical results for the same physical parameters. Theoretically they should be the same because the same Ladbrooke model was applied for small-signal simulation in both models. It is not clear whether the discrepancies are due to

different approaches to obtain the DC operating points or arise from the non-unique solution problem of statistical modeling. It would be interesting to further investigate these statistical models.

4. Yield-driven design of nonlinear large-scale circuits is a challenge in microwave CAD. Physics-based yield optimization has been considered as an important part of MMIC design since it links the design procedure directly to the physical and process parameters. Yield optimization usually requires a large number of circuit simulations which dominate the computation time. This becomes more critical in physics-based yield optimization. Significant improvement will be achieved if the number of circuit outcomes considered for yield optimization can be reduced. It would be very useful to develop an efficient yield optimization technique which has the capability of using a small number of outcomes while keeping an acceptable accuracy of predicted yield.

BIBLIOGRAPHY

[1] H.L. Abdel-Malek and J.W. Bandler, "Yield optimization for arbitrary statistical distributions: Part I-theory," *IEEE Trans. Circuits Syst.*, vol. CAS-27, 1980, pp. 245-253.

[2] H.L. Abdel-Malek and J.W. Bandler, "Yield optimization for arbitrary statistical distributions: Part II-implementation," *IEEE Trans. Circuits and Syst.*, vol. CAS-27, 1980, pp. 253-262.

[3] T.J. Aprille, Jr., and T.N. Trick, "Steady-state analysis of nonlinear circuits with periodic inputs," *Proc. IEEE*, vol. 60, 1972, pp. 108-114.

[4] T.J. Aprille, Jr., and T.N. Trick, "A computer algorithm to determine the steady-state response of nonlinear oscillators," *IEEE Trans. Circuit Theory*, vol. CT-19, 1972, pp. 354-360.

[5] I.J. Bahl, "Transmission Lines and Lumped Elements", in *Microwave Solid State Circuit Design*, I.J. Bahl and P. Bhartia, Eds. New York: Wiley, 1988, Chapter 2.

[6] J.W. Bandler, "Optimization of design tolerances using nonlinear programming," *Proc. 6th Princeton Conf. on Information Sciences and Systems* (Princeton, NJ), 1972, pp. 655-659. Also in *Computer-Aided Filter Design*, G. Szentirmai, Ed. New York: IEEE Press, 1973.

[7] J.W. Bandler, "The tolerance problem in optimal design," *Proc. European Microwave Conf.* (Brussels, Belgium), 1973, Paper A.13.1.(I).

[8] J.W. Bandler, "Optimization of design tolerances using nonlinear programming," *J. Optimization Theory and Applications*, vol. 14, 1974, pp. 99-114.

[9] J.W. Bandler, P.C. Liu and H. Tromp, "A nonlinear programming approach to optimal design centering, tolerancing and tuning," *IEEE Trans. Circuits Syst.*, vol. CAS-23, 1976, pp. 155-165.

[10] J.W. Bandler, P.C. Liu and H. Tromp, "Integrated approach to microwave design," *IEEE Trans. Microwave Theory Tech.*, vol. MTT-24, 1976, pp. 584-591.

[11] J.W. Bandler and H.L. Abdel-Malek, "Optimal centering, tolerancing, and yield determination via updated approximations and cuts," *IEEE Trans. Circuits Syst.*, vol. CAS-25, 1978, pp. 853-871.

[12] J.W. Bandler, W. Kellermann and K. Madsen, "A superlinearly convergent minimax algorithm for microwave circuit design", *IEEE Trans. Microwave Theory Tech.*, vol. MTT-33, 1985, pp. 1519-1530.

[13] J.W. Bandler, S.H. Chen and S. Daijavad, "Microwave device modeling using efficient ℓ_1 optimization: A novel approach," *IEEE Trans. Microwave Theory Tech.*, vol. MTT-34, 1986, pp. 1282-1293.

[14] J.W. Bandler, S.H. Chen and M.L. Renault, "KMOS-a fortran library for nonlinear optimization," Department of Electrical and Computer Engineering, McMaster University, Hamilton, Canada, Report SOS-87-1-R, 1987.

[15] J.W. Bandler and S.H. Chen, "Circuit optimization: the state of the art", *IEEE Trans. Microwave Theory Tech.*, vol. 36, 1988, pp. 424-443.

[16] J.W. Bandler, S.H. Chen, S. Daijavad and K. Madsen, "Efficient optimization with integrated gradient approximations," *IEEE Trans. Microwave Theory Tech.*, vol. 36, 1988, pp. 444-455.

[17] J.W. Bandler, S.H. Chen, S. Ye and Q.J. Zhang, "Integrated model parameter extraction using large-scale optimization concepts," *IEEE Trans. Microwave Theory Tech.*, vol. 36, 1988, pp. 1629-1638.

[18] J.W. Bandler, Q.J. Zhang and R.M. Biernacki, "A unified theory for frequency domain simulation and sensitivity analysis of linear and nonlinear circuits," *IEEE Trans. Microwave Theory Tech.*, vol. 36, 1988, pp. 1661-1669.

[19] J.W. Bandler, Q.J. Zhang, S. Ye and S.H. Chen, "Efficient large-signal FET parameter extraction using harmonics," *IEEE Trans. Microwave Theory Tech.*, vol. 37, 1989, pp. 2099-2108.

[20] J.W. Bandler, R.M. Biernacki, S.H. Chen, J. Loman, M. Renault and Q.J. Zhang, "Combined discrete/normal statistical modeling of microwave devices," *Proc. European Microwave Conf.* (Wembley, England), 1989, pp. 205-210.

[21] J.W. Bandler, Q.J. Zhang and R.M. Biernacki, "Practical, high-speed gradient computation for harmonic balance simulators," *IEEE Int. Microwave Symp. Dig.* (Long Beach, CA), 1989, pp. 363-366.

[22] J.W. Bandler, Q.J. Zhang, J. Song and R.M. Biernacki, "Yield optimization of nonlinear circuits with statistically characterized devices," *IEEE Int. Microwave Symp. Dig.* (Long Beach, CA), 1989, pp. 649-652.

[23] J.W. Bandler, Q.J. Zhang and Q. Cai, "Nonlinear circuit optimization with dynamically integrated physical device models," *IEEE Int. Microwave Symp. Dig.* (Dallas, TX), 1990, pp. 303-306.

[24] J.W. Bandler, Q.J. Zhang, J. Song and R.M. Biernacki, "FAST gradient based yield optimization of nonlinear circuits", *IEEE Trans. Microwave Theory Tech.*, vol. 38, 1990, pp. 1701-1710.

[25] J.W. Bandler, R.M. Biernacki, S.H. Chen, J. Song, S. Ye and Q.J. Zhang, "Statistical modeling of GaAs MESFETs," *IEEE Int. Microwave Symp. Dig.* (Boston, MA), 1991, pp. 87-90.

[26] J.W. Bandler, R.M. Biernacki, S.H. Chen, J. Song, S. Ye and Q.J. Zhang, "Gradient quadratic approximation scheme for yield-driven design," *IEEE Int. Microwave Symp. Dig.* (Boston, MA), 1991, pp. 1197-1200.

[27] J.W. Bandler, R.M. Biernacki, S.H. Chen, J. Song, S. Ye and Q.J. Zhang, "Analytically unified DC/small-signal/large-signal circuit design," *IEEE Trans. Microwave Theory Tech.*, vol. 39, 1991, pp. 1076-1082.

[28] J.W. Bandler, Q. Cai, R.M. Biernacki, S.H. Chen and Q.J. Zhang, "Physics-based design and yield optimization of MMICs," *Proc. European Microwave Conf.* (Stuttgart, Germany), 1991, pp. 1515-1520.

[29] J.W. Bandler, R.M. Biernacki, Q. Cai, S.H. Chen, S. Ye and Q.J. Zhang, "Integrated physics-oriented statistical modeling, simulation and optimization," *IEEE Trans. Microwave Theory Tech.*, vol. 40, 1992, pp. 1374-1400.

[30] J.W. Bandler, S. Ye, Q. Cai, R.M. Biernacki and S.H. Chen, "Predictable yield-driven circuit optimization," *IEEE Int. Microwave Symp. Dig.* (Albuquerque, NM), 1992, pp. 837-840.

[31] E. Bedrosian and S.O. Rice, "The output properties of Volterra systems (nonlinear systems with memory) driven by harmonic and Gaussian inputs," *Proc. IEEE*, vol. 59, 1971, pp. 1688-1707.

[32] R.M. Biernacki and M.A. Styblinski, "Statistical circuit design with a dynamic constraint approximation scheme," *Proc. IEEE Int. Symp. Circuits Syst.* (San Jose, CA), 1986, pp. 976-979.

[33] R.M. Biernacki, J.W. Bandler, J. Song and Q.J. Zhang, "Efficient quadratic approximation for statistical design," *IEEE Trans. Circuits Syst.*, vol. 36, 1989, pp. 1449-1454.

[34] C.G. Broyden, "A class of methods for solving nonlinear simultaneous equations," *Mathematics of Computation*, vol. 19, 1965, pp. 577-593.

[35] J.J. Bussgang, L. Ehrman and J.W. Graham, "Analysis of nonlinear systems with multiple inputs," *Proc. IEEE*, vol. 62, 1974, pp. 1088-1119.

[36] C.R. Chang, M.B. Steer and G.W. Rhyne, "Frequency-domain spectral balance using the arithmetic operator method," *IEEE Trans. Microwave Theory Tech.*, vol. MTT-37, 1989, pp. 1681-1688.

[37] C.R. Chang and M.B. Steer, "Frequency-domain nonlinear microwave circuit simulation using the arithmetic operator method," *IEEE Trans. Microwave Theory Tech.*, vol. 38, 1990, pp. 1139-1143.

[38] C.S. Chang and D.Y.S. Day, "Analytic theory for current-voltage characteristics and field distribution of GaAs MESFET's", *IEEE Trans. Electron Devices*, vol. 36, 1989, pp. 269-280.

[39] L.O. Chua and P. Lin, *Computer-Aided Analysis of Electronic Circuits: Algorithms and Computational Techniques*. Engelwood Cliffs, NJ: Prentice-Hall, 1975.

[40] F.R. Colon and T.N. Trick, "Fast periodic steady-state analysis for large-signal electronic circuits," *IEEE J. Solid-State Circuits*, vol. SC-8, 1973, pp. 260-269.

[41] P.F. Cox, P. Yang, S.S. Mahant-Shetti and P. Chatterjee, "Statistical modeling for efficient parametric yield estimation of MOS VLSI circuits," *IEEE Trans. Electron Devices*, vol. ED-32, 1985, pp. 471-478.

[42] W.J. Cunningham, *Introduction to Nonlinear Analysis*. New York: McGraw-Hill, 1958.

[43] W.R. Curtice, "A MESFET model for use in the design of GaAs integrated circuits," *IEEE Trans. Microwave Theory Tech.*, vol. MTT-28, 1980, pp. 448-456.

[44] W.R. Curtice and Y.H. Yun, "A temperature model for the GaAs MESFET," *IEEE Trans. Electron Devices*, vol. ED-28, 1981, pp. 954-962.

[45] W.R. Curtice and M. Ettenberg, "A nonlinear GaAs FET model for use in the design of output circuits for power amplifiers," *IEEE Trans. Microwave Theory Tech.*, vol. MTT-33, 1985, pp. 1383-1394.

[46] W.R. Curtice, "Nonlinear analysis of GaAs MESFET amplifiers, mixers, and distributed amplifiers using harmonic balance technique," *IEEE Trans. Microwave Theory Tech.*, vol. 35, 1987, pp. 441-447.

[47] W.R. Curtice, "GaAs MESFET modeling and nonlinear CAD," *IEEE Trans. Microwave Theory Tech.*, vol. 36, 1988, pp. 220-230.

[48] S.W. Director, "A method for quick determination of the periodic steady-state in nonlinear networks," *Proc. 9th Allerton Conf. Circuits Syst. Theory*, (Urbana, IL), 1971, pp. 131-139.

[49] S.W. Director and K.W. Current, "Optimization of forced nonlinear periodic circuits," *IEEE Trans. Circuits Syst.*, vol. CAS-23, 1976, pp. 329-335.

[50] S.W. Director and G.D. Hachtel, "The simplicial approximation approach to design centering," *IEEE Trans. Circuits Syst.*, vol. CAS-24, 1977, pp. 363-372.

[51] D.A. Divekar, R.W. Dutton and W.J. McCalla, "Experimental study of Gummel-Poon model parameter correlations for bipolar junction transistors," *IEEE J. Solid-State Circuits*, vol. SC-12, 1977, pp. 552-559.

[52] R.W. Dutton, D.A. Divekar, A.G. Gonzalez, S.E. Hansen and D.A. Antoniadis, "Correlation of fabrication process and electrical device parameter variations," *IEEE J. Solid-State Circuits*, vol. SC-12, 1977, pp. 349-355.

[53] S. El-Rabaie, J.A.C. Stewart, V.F. Fusco and J.J. McKeown, "A novel approach for the large signal analysis and optimisation of microwave frequency doublers", *IEEE Int. Microwave Symp. Dig.* (New York, NY), 1988, pp. 1119-1122.

[54] F. Filicori, V.A. Monaco and C.U. Naldi, "Simulation and design of microwave class-C amplifiers through harmonic analysis," *IEEE Trans. Microwave Theory Tech.*, vol. MTT-27, 1979, pp. 1043-1051.

[55] F. Filicori, G. Ghione and C.U. Naldi, "Physics-based electron device modelling and computer-aided MMIC design," *IEEE Trans. Microwave Theory Tech.*, vol. 40, 1992, pp. 1333-1352.

[56] H. Fukui, "Determination of the basic device parameters of a GaAs MESFET," *Bell Syst. Tech. J.*, vol. 58, 1979, pp. 771-797.

[57] R. Gilmore, "Nonlinear circuit design using the modified harmonic balance algorithm", *IEEE Trans. Microwave Theory Tech.*, vol. MTT-34, 1986, pp. 1294-1307.

[58] R.J. Gilmore and M.B. Steer, "Nonlinear circuit analysis using the method of harmonic balance-a review of the art. Part I. introductory concepts," *Int. J. Microwave and Millimetre-Wave Computer-Aided Engineering*, vol. 1, 1991, pp. 22-37.

[59] R.J. Gilmore and M.B. Steer, "Nonlinear circuit analysis using the method of harmonic balance-a review of the art. Part II. advanced concepts," *Int. J. Microwave and Millimetre-Wave Computer-Aided Engineering*, vol. 1, 1991, pp. 159-180.

[60] R. Goyal, M. Golio and W. Thomann, "Device modeling", in *Monolithic Microwave Integrated Circuits: Technology & Design*, R. Goyal Ed. Boston: Artech House, 1989, Chapter 4.

[61] A.B. Grebene and S.K. Ghandhi, "General theory for pinched operation of the junction-gate FET," *Solid-State Electronics*, vol. 12, 1969, pp. 573-589.

[62] J.H. Haywood and Y.L. Chow, "Intermodulation distortion analysis using a frequency-domain harmonic balance technique," *IEEE Trans. Microwave Theory Tech.*, vol. MTT-36, 1988, pp. 1251-1257.

[63] G.L. Heiter, "Characterization of nonlinearities in microwave devices and systems," *IEEE Trans. Microwave Theory Tech.*, vol. MTT-21, 1973, pp. 797-805.

[64] N. Herr and J.J. Barnes, "Statistical circuit simulation modeling of CMOS VLSI," *IEEE Trans. Computer-Aided Design*, vol. CAD-5, 1986, pp. 15-22.

[65] R.G. Hicks and P.J. Khan, "Numerical analysis of subharmonic mixers using accurate and approximate models," *IEEE Trans. Microwave Theory Tech.*, vol. MTT-30, 1982, pp. 2113-2120.

[66] P.A. Houston and A.G.R. Evans, "Electron drift velocity in n-GaAs at high electric fields", *Solid-State Electronics*, vol. 20, 1977, pp. 197-204.

[67] Y. Hu, J. Obregon and J.C. Mollier, "Nonlinear analysis of microwave FET oscillators using Volterra series," *IEEE Trans. Microwave Theory Tech.*, vol. 37, 1989, pp. 1689-1693.

[68] V.D. Hwang and T. Itoh, "An efficient approach for large-signal modeling and analysis of GaAs MESFET," *IEEE Trans. Microwave Theory Tech.*, vol. MTT-35, 1987, pp. 396-402.

[69] V.D. Hwang, Y-C. Shih, H.M. Le and T. Itoh, "Nonlinear modeling and verification of MMIC amplifiers using the waveform-balance method", *IEEE Trans. Microwave Theory Tech.*, vol. 37, 1989, pp. 2125-2133.

[70] A.K. Jastrzebski and M.I. Sobhy, "Analysis of microwave circuits using state-space approach," *Proc. IEEE Int. Symp. Circuits Syst.* (Montreal, Canada), 1984, pp. 1119-1122.

[71] A.R. Jha, R. Goyal and B. Manz, "Introduction," in *Monolithic Microwave Integrated Circuits: Technology & Design*, R. Goyal Ed. Boston: Artech House, 1989, Chapter 1.

[72] B.J. Karafin, "The optimum assignment of component tolerances for electrical networks," *Bell Syst. Tech. J.*, vol. 50, 1971, pp. 1225-1242.

[73] D.P. Kennedy and R.R. O'Brien, "Computer aided two dimensional analysis of the junction field-effect transistor," *IBM J. Res. Devel.*, vol. 14, 1970, pp. 95-116.

[74] C. Kermarrec and C. Rumelhard, "Microwave monolithic integrated circuits", in *GaAs MESFET Circuit Design*, R. Soares Ed. Boston: Artech House, 1988, Chapter 9.

[75] M.A. Khatibzadeh, "Large-signal modeling of gallium-arsenide field-effect transistors", Ph.D. dissertation, North Carolina State University, Raleigh, NC, 1987.

[76] M.A. Khatibzadeh and R.J. Trew, "A large-signal, analytic model for the GaAs MESFET", *IEEE Trans. Microwave Theory Tech.*, vol. 36, 1988, pp. 231-238.

[77] K.S. Kundert and A. Sangiovanni-Vincentelli, "Simulation of nonlinear circuits in the frequency domain," *IEEE Trans. Computer-Aided Design*, vol. CAD-5, 1986, pp. 521-535.

[78] P.H. Ladbrooke, *MMIC Design: GaAs FETs and HEMTs*. Norwood, MA: Artech House, 1989.

[79] C.L. Law and C.S. Aitchison, "Prediction of wide-band power performance of MESFET distributed amplifiers using the Volterra series representation," *IEEE Trans. Microwave Theory Tech.*, vol. MTT-34, 1986, pp. 1308-1317.

[80] K. Lehovec and R. Zuleeg, "Voltage-current characteristics of GaAs J-FETs in the hot electron range", *Solid-State Electronics*, vol. 13, 1970, pp. 1415-1426.

[81] S.Y. Liao, *Microwave Devices and Circuits*, Third Edition, Englewood Cliffs, NJ: Prentice-Hall, 1990.

[82] J.C. Lindenlaub, "An approach for finding the sinusoidal steady-state response of nonlinear systems," *Proc. 7th Allerton Conf. Circuit Syst. Theory* (Chicago, IL), 1969, pp. 323-327.

[83] S. Liu and K. Singhal, "A statistical model for MOSFETs," *Proc. IEEE Int. Conf. Computer-Aided Design* (Santa Clara, CA), 1985, pp. 78-80.

[84] S.A. Maas, "A general-purpose computer program for the Volterra-series analysis of nonlinear microwave circuits," *IEEE Int. Microwave Symp. Dig.* (New York, NY), 1988, pp. 311-314.

[85] A. Madjar and F.J. Rosenbaum, "A large-signal model for the GaAs MESFET", *IEEE Trans. Microwave Theory Tech.*, vol. MTT-29, 1981, pp. 781-788.

[86] A. Materka and T. Kacprzak, "Computer calculation of large-signal GaAs FET amplifier characteristics," *IEEE Trans. Microwave Theory Tech.*, vol. MTT-33, 1985, pp. 129-135.

[87] M.D. Meehan, T. Wandinger and D.A. Fisher, "Accurate design centering and yield prediction using the 'truth model'," *IEEE Int. Microwave Symp. Dig.* (Boston, MA), 1991, pp. 1201-1204.

[88] A.I. Mees, *Dynamics of Feedback Systems*. New York: Wiley, 1981.

[89] R.A. Minasian, "Intermodulation distortion analysis of MESFET amplifiers using Volterra series representation," *IEEE Trans. Microwave Theory Tech.*, vol. MTT-28, 1980, pp. 1-8.

[90] L.W. Nagel and D.O. Pederson, *SPICE (Simulation Program with Integrated Circuit Emphasis)*, Electronics Research Laboratory, University of California, Memo ERL-M382, April, 1973.

[91] M.S. Nakhla and J. Vlach, "A piecewise harmonic-balance technique for determination of periodic response of nonlinear systems," *IEEE Trans. Circuits Syst.*, vol. CAS-23, 1976, pp. 85-91.

[92] M.S. Nakhla and F.H. Branin, Jr., "Determining the periodic response of nonlinear systems by a gradient method," *Int. J. Circuit Theory Appl.*, vol. 5, 1977, pp. 255-273.

[93] J.F. Pinel and K.A. Roberts, "Tolerance assignment in linear networks using nonlinear programming," *IEEE Trans. Circuit Theory*, vol. CT-19, 1972, pp. 475-479.

[94] M.J.D. Powell, "A Fortran subroutine for unconstrained minimization, requiring first derivatives of the objective functions," Atomic Energy Research Establishment, Harwell, Berkshire, England, Rep. AERE-R. 6469, 1970, pp. 20-27.

[95] R.A. Pucel, A. Haus and H. Statz, "Signal and noise properties of gallium arsenide microwave field-effect transistors", in *Advances in Electronics and Electron Physics*, vol. 38. New York: Academic Press, 1975, pp. 195-265.

[96] J. Purviance, D. Criss and D. Monteith, "FET model statistics and their effects on design centering and yield prediction for microwave amplifiers," *IEEE Int. Microwave Symp. Dig.* (New York, NY), 1988, pp. 315-318.

[97] J.E. Purviance, M.C. Petzold and C. Potratz, "A linear statistical FET model using principal component analysis," *IEEE Trans. Microwave Theory Tech.*, vol. 37, 1989, pp. 1389-1394.

[98] J. Purviance, M. Meehan and D. Collins, "Properties of FET parameter statistical data bases," *IEEE Int. Microwave Symp. Dig.* (Dallas, TX), 1990, pp. 567-570.

[99] P.J. Rankin, "Statistical modeling for integrated circuits," *IEE Proc.*, vol. 129, Pt. G, No. 4, 1982, pp. 186-191.

[100] M. Reiser, "A two-dimensional numerical FET model for DC, AC and large-signal analysis," *IEEE Trans. Electron Devices*, vol. ED-20, 1973, pp. 35-45.

[101] G.W. Rhyne and M.B. Steer, "Generalized power series analysis of intermodulation distortion in a MESFET amplifier: simulation and experiment," *IEEE Trans. Microwave Theory Tech.*, vol. MTT-35, 1987, pp. 1248-1255.

[102] G.W. Rhyne, M.B. Steer and B.D. Bates, "Frequency-domain nonlinear circuit analysis using generalized power series," *IEEE Trans. Microwave Theory Tech.*, vol. MTT-36, 1988, pp. 379-387.

[103] P.N. Rigby, J.R. Suffolk and R.S. Pengell, "Broadband monolithic low-noise feedback amplifiers," *IEEE Int. Microwave Symp. Dig.* (Boston, MA), 1983, pp. 41-45.

[104] V. Rizzoli, A. Lipparini, and E. Marazzi, "A general-purpose program for nonlinear microwave circuit design," *IEEE Trans. Microwave Theory Tech.*, vol. 31, 1983, pp. 762-770.

[105] V. Rizzoli, C. Cecchetti, A. Lipparini, and F. Mastri, "General-purpose harmonic balance analysis of nonlinear microwave circuits under multitone excitation," *IEEE Trans. Microwave Theory Tech.*, vol. 36, 1988, pp. 1650-1660.

[106] J.G. Ruch and G.S. Kino, "Measurement of the velocity-field characteristic of gallium arsenide", *Appl. Phys. Lett.*, vol. 10, 1967, pp. 40-42.

[107] I.W. Sandberg, "Expansions for nonlinear systems," *Bell Syst. Tech. J.*, vol. 61, 1982, pp. 159-199.

[108] P.A. Sandborn, J.R. East and G.I. Haddad, "Quasi-two-dimensional modeling of GaAs MESFET's", *IEEE Trans. Electron Devices*, vol. ED-34, 1987, pp. 985-991.

[109] R.G. Sea, "An algebraic formula for amplitudes of intermodulation products involving an arbitrary number of frequencies," *Proc. IEEE*, vol. 56, 1968, pp. 1388-1389.

[110] R.G. Sea and A.G. Vacroux, "On the computation of intermodulation products for a power series nonlinearity," *Proc. IEEE*, 1969, pp. 337-338.

[111] W. Shockley, "A unipolar 'field-effect' transistor", *Proc. IRE*, vol. 40, 1952, pp. 1365-1376.

[112] S. Skelboe, "Computation of the periodic steady-state response of nonlinear networks by extrapolation methods," *IEEE Trans. Circuits Syst.*, vol. CAS-27, 1980, pp. 161-175.

[113] S. Skelboe, "Time-domain steady-state analysis of nonlinear electrical systems," *Proc. IEEE*, vol. 70, 1982, pp. 1210-1228.

[114] K. Singhal and J.F. Pinel, "Statistical design centering and tolerancing using parametric sampling," *IEEE Trans. Circuits Syst.*, vol. CAS-28, 1981, pp. 692-702.

[115] C.M. Snowden, M.J. Hawes and D.V. Morgan, "Large-signal modeling of GaAs MESFET operation," *IEEE Trans. Electron Devices*, vol. ED-30, 1983, pp. 1817-1824.

[116] C.M. Snowden and D. Loret, "Two-dimensional hot-electron models for short-gate-length GaAs MESFETs," *IEEE Trans. Electron Devices*, vol. ED-34, 1987, pp. 212-223.

[117] C.M. Snowden and R.R. Pantoja, "Quasi-two-dimensional MESFET simulation for CAD," *IEEE Trans. Electron Devices*, vol. ED-36, 1989, pp. 1564-1574.

[118] C.M. Snowden and R.R. Pantoja, "GaAs MESFET physical models for process-oriented design," *IEEE Trans Microwave Theory Tech.*, vol. 40, 1992, pp. 1401-1409.

[119] M.I. Sobhy and A.K. Jastrzebski, "Direct integration methods of nonlinear microwave circuits," *Proc. 15th European Microwave Conf.* (Paris, France), 1985, pp. 1110-1118.

[120] R.S. Soin and R. Spence, "Statistical exploration approach to design centering," *Proc. IEE*, vol. 127, pt. G., 1980, pp. 260-269.

[121] C.J.B. Spanos and S.W. Director, "Parameter extraction for statistical IC process characterization," *IEEE Trans. Computer-Aided Design*, vol. CAD-5, 1986, pp. 66-78.

[122] H. Statz, P. Newman, I.W. Smith, R.A. Pucel and H.A. Haus, "GaAs FET device and circuit simulation in SPICE," *IEEE Trans. Electron Devices*, vol. ED-34, 1987, pp. 160-169.

[123] M.B. Steer and P.J. Khan, "An algebraic formula for the output of a system with large-signal multifrequency excitation," *Proc. IEEE*, 1983, pp. 177-179.

[124] M.B. Steer, C.R. Chang and G.W. Rhyne, "Computer-aided analysis of nonlinear microwave circuits using frequency-domain nonlinear analysis techniques: the state of the art," *Int. J. Microwave and Millimetre-Wave Computer-Aided Engineering*, vol. 1, 1991, pp. 181-200.

[125] D.E. Stoneking, G.L. Bilbro, P.A. Gilmore, R.J. Trew and C.T. Kelly, "Yield optimization using a GaAs process simulator coupled to a physical device model," *IEEE Trans Microwave Theory Tech.*, vol. 40, 1992, pp. 1353-1373.

[126] M.A. Styblinski, "Factor analysis model of resistor correlations for monolithic integrated circuits," *Proc. IEEE Int. Symp. Circuits Syst.* (Tokyo, Japan), 1977, pp. 776-777.

[127] M.A. Styblinski and A. Ruszczynski, "Stochastic approximation approach to statistical circuit design," *Electronics Lett.*, vol. 19, 1980, pp. 300-302.

[128] R.B. Swerdlow, "Analysis of intermodulation noise in frequency converters by Volterra series," *IEEE Trans. Microwave Theory Tech.*, vol. MTT-26, 1978, pp. 305-313.

[129] S.M. Sze, *Physics of Semiconductor Devices*, Second Edition, New York: John Wiley and Suns, 1981.

[130] R.S. Tucker, "Third-order intermodulation distortion and gain compression in GaAs FET's," *IEEE Trans. Microwave Theory Tech.*, vol. MTT-27, 1979, pp. 400-408.

[131] J.A. Turner and B.L.H. Wilson, "Implications of carrier velocity saturation in a gallium arsenide field-effect transistor," *Proc. Symp. Gallium Arsenide*, 1968, pp. 195-204.

[132] A. Ushida and L.O. Chua, "Frequency-domain analysis of nonlinear circuits driven by multi-tone signals," *IEEE Trans. Circuits Syst.*, vol. CAS-31, 1984, pp. 766-779.

[133] P.W. Van Der Walt, "Efficient technique for solving nonlinear mixer pumping problem," *Electronics Lett.*, vol 21, 1985, pp. 899-900.

[134] J. Vlach and K. Singhal, *Computer Methods for Circuit Analysis and Design.* New York: Van Nostrand Reinhold, 1983.

[135] V. Volterra, *Theory of Functionals and of Integral and Integro-Differential Equations.* London: Blackie & Son, 1930.

[136] D.D. Weiner and J.F. Spina, *Sinusoidal Analysis and Modeling of Weakly Nonlinear Circuits.* New YorK: Van Nostrand Reinhold, 1980.

[137] K. Yamaguchi and H. Kodera, "Drain conductance of junction gate FET's in the hot electron range", *IEEE Trans. Electron Devices*, vol. ED-23, 1976, pp. 545-553.

[138] *HarPE*™, Optimization Systems Associates Inc., P.O. Box 8083, Dundas, Ontario, Canada L9H 5E7, 1991.

[139] *OSA90/hope*™, Optimization Systems Associates Inc., P.O. Box 8083, Dundas, Ontario, Canada L9H 5E7, 1991.

[140] Measurement data provided by Plessey Research Caswell Ltd., Caswell, Towcester, Northamptonshire, England NN12 8EQ, 1990.

[141] *Libra*™, EEsof Inc., Westlake Village, CA 91362.

[142] *Microwave Harmonica User's Manual*, Compact Software Inc., Patterson, NJ, 07504, 1987.

AUTHOR INDEX

SUBJECT INDEX